Perfusion SPECT Guided Dose Escalation in Radiation Therapy for Lung Cancer Patients

by

Lingshu Yin

B.Sc. Nanjing University 2006

M.Sc. The University of British Columbia 2008

A THESIS SUBMITTED IN PARTIAL FULFILLMENT
OF THE REQUIREMENTS FOR THE DEGREE OF

Doctor of Philosophy

in

THE FACULTY OF GRADUATE STUDIES

(Physics)

The University Of British Columbia

(Vancouver)

March 2012

Abstract

Radiation therapy (RT) is a standard of care for patients with locally advanced inoperable non-small cell lung cancer (NSCLC). Prognosis for these patients is poor with 2-years survival below 20%. A substantial proportion of the lung cancer patients receiving RT develop symptomatic radiation pneumonitis (RP) as radiation-induced side effects. Thus, sparing of normal lung is one of the important goals for lung cancer patients receiving RT.

Currently in clinical practice, the sparing of lung is assessed based on the dose-volume histogram (DVH) assuming homogeneous lung function which is clearly not valid. Lung perfusion scan using Single Photon Emission Computed Tomography (SPECT) with ^{99m}Tc macroaggregated albumin (^{99m}Tc-MAA) provides unique functional information (lung perfusion i.e. blood flow) about the lung and holds the potential to improve normal tissue sparing in RT. Incorporating functional information from perfusion SPECT scan into RT treatment planning allows for identifying and sparing the well perfused parts of lung, thus reducing the risk of clinically significant radiation-induced lung complications.

From February 2008 to May 2011, 22 lung cancer patients in BC Cancer Agency were recruited into this ethics board approved SPECT study. The goal of this study is to establish a framework for SPECT-guided RT treatment planning and dose escalation trials. In this study, the incorporation of SPECT into RT treatment planning is carried out in a sequential manner including:

1. Reconstruction of SPECT images and investigating the metric of functional sparing for treatment planning

2. Evaluation of SPECT image registration algorithms

3. Developing the methodology of SPECT-guided intensity modulated radiation therapy (IMRT) treatment planning with a Monte Carlo based beamlets dose calculation

4. Evaluation of the effectiveness of SPECT-guided RT through a planning study comparing DVH and SPECT-driven IMRT plans.

In conclusion, comparing to conventional DVH driven IMRT plans, we found that SPECT-driven IMRT plans provide better sparing of both lung function and volume. Mean lung dose and SPECT-weighted mean dose can be reduced by 10.8% and 13.1%, respectively. We suggest that the use of SPECT guided IMRT treatment planning improves the sparing of lung functionality and makes possible dose escalations in patients with non-small cell lung cancers.

Preface

The work presented in this dissertation is based on a clinical study conducted in British Columbia Cancer Agency from 2008 to 2011. Ethics approval was obtained from UBC BCCA Research Ethics Board since Dec,2007 (REB Number H07-02614). Project title is "Using Single Positron Emission Computerized Tomography (SPECT) functional lung imaging in radiotherapy planning and treatment of lung cancer and to assess lung toxicity secondary to radiotherapy treatment".

Part of the work presented in Chapter 2 and Chapter 3 has also been published in peer-reviewed journals. The manuscripts of these publications have been integrated into this dissertation to produce a smooth and unified presentation of the entire SPECT study. I am the first and corresponding author of these publications, meanwhile many collaborators also contributed significantly to it. Reference of the publications and authors are listed here:

- Lingshu Yin, Sergey Shcherbinin, Anna Celler, Anna Thompson, Tsien-Fei Fua, Mitchell Liu, Cheryl Duzenli, Brad Gill, Finbar Sheehan, John Powe, Daniel Worsley, Lawrence Marks and Vitali Moiseenko. Incorporating quantitative SPECT into radiation therapy treatment planning for lung cancer: the impact of attenuation and scatter correction on the SPECT Weighted Mean Dose and Functional Lung Segmentation. *Int.J.Rad.Oncol.Bio.Phys* Vol 78(2); 587-594, 20

- Lingshu Yin, Lisa Tang, Gahassan Hamarneh, Brad Gill, Anna Celler, Sergey Shcherbinin, Tsien-Fei Fua, Anna Thompson, Mitchell Liu, Cheryl Duzenli, Finbar Sheehan and Vitali Moiseenko. Complexity and accuracy of image registration methods in SPECT guided radiation therapy. *Phys.Med.Bio* Vol

55; 237-246, 2010

The inclusion of the published journal articles, in full or in part, in a dissertation is permitted per the author-publisher agreement of Elsevier (publisher of *Int.J.Rad.Oncol.Bio.Phys*) and IOP Publishing (publisher of *Phys.Med.Bio*).

Table of Contents

List of Tables

List of Figures

Glossary

CRT Conformal Radiation Therapy

CTV Clinical Target Volume

DAO Direct Aperture Optimization

DNA Deoxyribonucleic Acid

DSB Double Strand Break

DVH Dose-Volume Histogram

GTV Gross Tumor Volume

IMRT Intensity Modulated Radiation Therapy

MC Monte Carlo

MLC Multi-Leaf Collimator

MLD Mean Lung Dose

OSEM Ordered Subset Expectation Maximization

PET Positron Emission Tomography

PTV Planning Target Volume

RP Radiation Pneumonitis

RT Radiation Therapy

SBRT Stereotactic Body Radiation Therapy

SPECT Single Photon Emission Computed Tomography

SSB Single Strand Break

Acknowledgments

First I would like to thank my research supervisor Dr. Vitali Moiseenko for his endless support and encouragements during the course of my MSc and PhD. His passion on research has always been an inspiration and motivation for me. I would also like to acknowledge other members of my thesis committee, Dr. Alex Mackay, Dr. Anna Celler, Dr. Cheryl Duzenli, and Dr. Chris Waltham, for their input throughout the years.

This SPECT study takes the effort from many people in different institutions. Dr. Anna Thompson, Dr. Tsien-Fei Fua, the late Dr. Finbar Sheehan and Dr. Jonn Wu contributed significantly at the beginning of this study. It would not be possible to bring this study into shape without them. Special thanks to Dr. Mitchell Liu who had amazingly recruited a large number of patients for this study. As a radiation oncologist, his enthusiasm and motivation about functional imaging is invaluable for the entire team. Dr. Lawrence Marks also generously helped us on the manuscript about image reconstruction which was later published in the red journal.

I would like to express my gratitude to Dr. Anna Celler and Dr. Sergey Shcherbinin. As nuclear medicine physicists, they provide unique views and insights about the impact of image reconstruction on radiation therapy. They made me think about research fields often overlooked by radiotherapy physicists. Sergey has also diligently taken care of all the image reconstruction works. Dr. Ghassan Hamarneh and his fellow student Lisa Tang provided critical help regarding the image registration project. I would like to thank all of them for their collaboration which has been a precious experience for me.

Thanks to Dr. Tony Popescu, Dr. Alanah Bergman and Tony Teke (soon to be

Dr. Tony Teke) for their help on Monte Carlo simulation and treatment planning, especially Tony Teke for his patience and help when I was using the computer cluster. The implementation of SPECT scan as part of the radiation therapy also required works from many clinical staff at Vancouver Cancer Centre and Vancouver General Hospital. I thank my colleagues Brad Gill, Carol Marlowe, Dr. John Powe and Dr. Daniel Worsley for their effort in making this a smooth and efficient process.

My sincere appreciation goes to my family and friends in China and Canada for their love and decades of friendship which are part of the momentum keeping me going through the frustrations and gladness in the course of my PhD.

Chapter 1

Introduction

1.1 Backgrounds

Cancer is the most common cause of death worldwide, about 13% of human deaths each year are caused by cancer [1]. Prostate cancer and breast cancer are the most common malignancies in men and women respectively, meanwhile lung cancer is the most common one for the entire population. Over 200,000 patients are expected to be diagnosed with lung cancer every year in North America [2]. Surgery, such as lobectomy, is the most effective and preferred choice of treatment for lung cancer patients. However, a large portion of patients are not eligible for surgery due to sickness and progression of the tumor. Radiation Therapy (RT) with or without chemotherapy has been shown as an effective type of treatment for early stage inoperable patients and late stage lung cancer patients.

Although radiation therapy is capable of delivering sufficient ionizing radiation to kill the tumor cells, it also causes damage to the normal tissues surrounding tumor. Consequently, patients may develop symptomatic radiation-induced complications in normal tissues. Most of the lung cancer patients treated with radiation develop radiation induced lung toxicity such as persistent cough, dyspnea, or in extreme cases severe respiratory insufficiency. Lung toxicity is classified as early Radiation Pneumonitis (RP) exhibited within 6 months after completion of RT and late fibrosis for toxicity diagnosed at follow-ups longer than 6 months. Advanced radiation delivery techniques such as 3D conformal radiation therapy (Figure 1.1),

Intensity Modulated Radiation Therapy (IMRT), Stereotactic Body Radiation Therapy (SBRT) have been developed and widely implemented in the clinics. With these techniques, it is possible to significantly reduce radiation damage to the normal tissue without compromising tumor control. Thus it is clinically feasible to escalate the radiation dose to the tumor without increasing normal tissue complication rates. Current clinical trials in lung cancer dose escalation are mainly focused on three different approaches:

1. Escalating tumor dose using conventional dose fractionation or hypofractionation
2. Conventional radiation therapy with concurrent chemotherapy
3. Stereotactic body radiation therapy

The latter is primarily designed for early stage lung cancer patients. Typical approaches in dose escalation trials as done in the Ann-Arbour [3] and Amsterdam [4] studies involves stratifying patients into different risk groups. Each group is associated with different probabilities of developing RPs as assessed using dose-volume indices or Mean Lung Dose (MLD). Prescription dose delivered to the tumor is escalated accordingly in each risk group. Maximum tolerated dose of each group can be established when more than one patient from a group of six patients enrolled to a specific risk group experienced dose limiting toxicities (such as Grad 3+ pneumonitis). In these studies, assessing of RP risks and treatment planning are strictly based on the data from Dose-Volume Histogram (DVH). The underlying assumption that lung function is homogeneous is not always valid in lung cancer patients. Recently, functional imaging guided radiation therapy has been proposed as a new approach to achieve dose escalation. Using Single Photon Emission Computed Tomography (SPECT) and Positron Emission Tomography (PET), it is possible to map the physiological status of different organs, such as lung perfusion and tumor metabolic activity. Incorporating this new functional information into RT treatment planning allows for more effective sparing of normal tissues and increased tumor control, thus it paves a new way to dose escalation in lung cancer treatment [5].

The goal of this PhD project is to investigate the feasibility and potential benefit of perfusion SPECT-guided dose escalation for lung cancer patients. To achieve

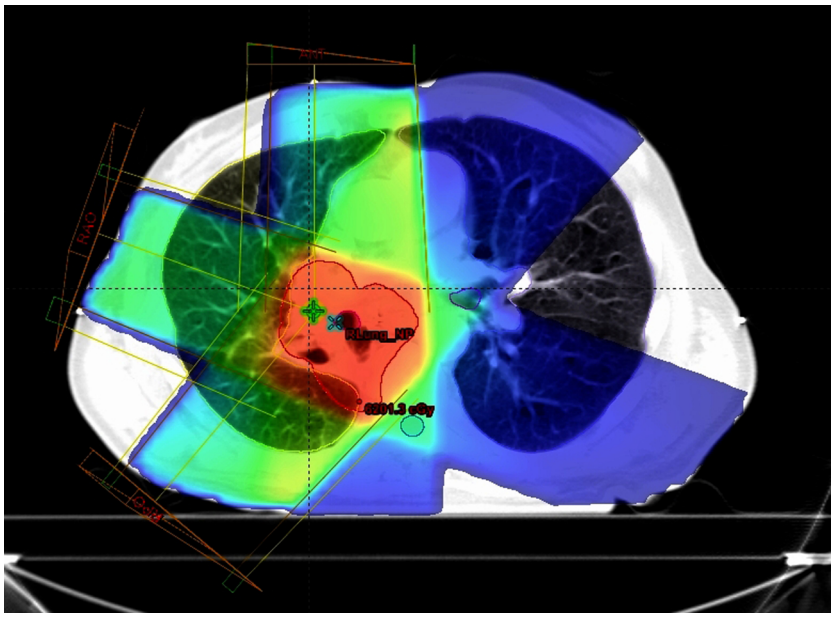

Figure 1.1: A sample 3D conformal radiation therapy plan for lung cancer patients

this, a methodology in the context of perfusion SPECT guided RT treatment planning was developed and implemented in our clinic. Methods and results of each part of this project (i.e. SPECT image reconstruction, image registration and treatment planning) are presented in the following three chapters.

1.2 Introduction to Radiation Physics and Radiation Biology

1.2.1 General Physics in Radiation Therapy

The energy of therapeutic X- and γ-rays ranges from 500kV to more than 18MV. At this energy level, most of the incoming photons will transfer their energy to the patient's body through Compton scattering. Other types of primary reactions include: pair production and photo-electric absorption. Through these processes, a part of, or the entire incident photon's energy is transferred to the medium giving rise to scattered electrons in most situations, whereas the scattered photon will

repeat those above mentioned interactions several times and continue losing its energy until fully absorbed or exit the patient's body. This energy transfered from the photon causes excitation and ionizations of molecules in the medium.

Since more than 80% of cell composition is water, ionizations and excitations of water molecules by photons or the electrons set in motion in the above listed reactions is the predominant path of energy deposition in photon irradiation. Free radicals, such as hydroxyl radical OH*, form as a result of reactions between ionized water molecules (H_2O^+) and other un-ionized water molecules, or as a result of dissociation of an excited water molecule. These free radicals are highly active and capable of altering chemical bonds of other molecules including DNA.

1.2.2 Radiation-induced Cell Lethality

Deoxyribonucleic Acid (DNA) contains all the genetic information for the proliferation and functioning of cells. Radiation induced cell lethality primarily comes from the damage in the DNA which is directly or indirectly brought by photons, electrons and free radicals like hydroxyl radicals.

The molecular structure of DNA has been widely accepted as a double helix model with two strands of sugar-phosphate backbone and bases connected by hydrogen bonds. During irradiation, one or both of the strands can be damaged due to irradiation either by a direct hit from a photon or electron, or by indirect chemical reactions with a free radical (Figure 1.2). Depending on whether a single or two opposite stands are damaged a Single Strand Break (SSB) or a Double Strand Break (DSB) is produced. A single strand break is relatively easier to repair, since the complementary information is stored in the opposite strand and DNA integrity is maintained. Double strand break requires two single strand breaks on opposite strands in close proximity to each other so that DNA integrity cannot be maintained and two open ends form as a result of this damage. The distance smaller than 10 base pairs between two SSB on opposite strands has been suggested in literature as a proximity threshold for two SSB to combine to form a DSB. Because a DSB causes a loss of DNA integrity, DSB is more difficult to repair and these lesions primarily contribute to cell death. Both SSB and DSBs are very common in the lifetime of a cell and most of them can be effectively repaired by various

pathways such as base excision repair, non-homologous end joining, homologous recombination, etc. Thus the mutation rate of mammalian cells is quite low. However, irradiation as used in the clinic can significantly increase the DNA lesion rate to a level where the damage to DNA cannot be faithfully repaired. A fatal mis-repaired and un-repaired DNA strand breaks lead to chromosome aberration interfering with cell mitosis. The damaged cells with certain types of chromosome aberrations will not be able to sustain repeat divisions. This leads to cell death known as reproductive death, i.e. cell lethality associated with cells attempting to divide. Chromosome aberrations which do not interfere with cell division, such as symmetric translocations or inversions, result in transformed cells. These cells are capable of sustaining cell divisions but with corrupted genetic code. A possible outcome of this might be secondary malignancy. These lesions, however, are not of primary interest for tumour control and normal tissue toxicity.

The dominant model describing cell survival probability as a function of dose is the Linear Quadratic (LQ) model as presented below. If a sample of mammalian cells is irradiated *in vitro*, the number of lethal lesions as they are distributed among the cells can be modeled using Poisson distribution. To survive a cell has to contain zero lethal lesions. The proportion of cells with no lethal lesions calculated from the Poisson distribution is:

$$SF = e^{-\bar{L}}$$

where SF is the surviving fraction, $\bar{L}$ is the average number of lethal lesions per cell. Lethal lesions can result from DSB produced by a single electron track (yield proportional to Dose) or by two electron tracks (i.e. binary exchange between two DSB produced by separate tracks, yield proportional to Dose^2). The average number of lethal lesions per cell, $\bar{L}$, can be calculated as the sum of two terms which are linear and quadratic, respectively:

$$\bar{L} = -\left(\alpha D + \beta D^2\right)$$

The quadratic term requires both DSB to be present in the cell at the same time, i.e. the second DSB should be created before the first DSB can be repaired, thus the quadratic term here is dose rate (or dose fractionation) dependent. In an acute irradiation, the duration of irradiation is too short for the repair to take place, the

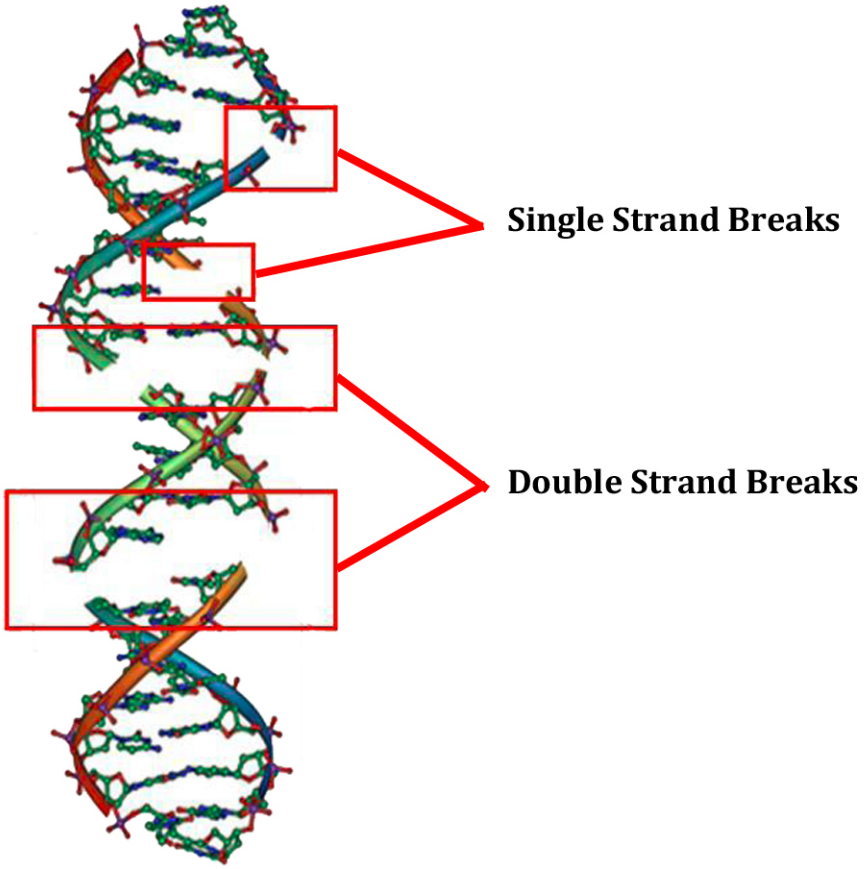

Figure 1.2: Illustration of single strand breaks and double strand breaks in DNA double helix model

surviving fraction of the irradiated *mammalian* cell population can be calculated without taking dose rate effect into consideration:

$$SF = e^{-(\alpha D + \beta D^2)}$$

where SF is surviving fraction, D is dose delivered in acute fashion, α and β are the model parameters. This is the Linear-Quadric (LQ) model which is the most widely used to describe dose-response for cell survival since the first in vitro survival curve

for mammalian cells irradiated with X-rays was reported by Puck et al in 1956 [6].

In current clinical practice, radiation is usually delivered in multiple fractions with equal dose per fraction and each fraction is delivered in an acute fashion. Given sufficient time between fractions to allow for full repair, the probability to survive all fractions is the product of probabilities to survive each fraction

$$SF = e^{-N\left(\alpha d+\beta d^2\right)} = e^{-(\alpha D+\beta d\times D)}$$

where D is total dose delivered in N fractions and d is the dose per fraction. Note that in this formula, increasing dose per fraction without escalating the total dose leads to increased cell killing. In clinical practice, this dose rate/fractionation effect can be used to model the outcome of hypo-fractionated radiation therapy in which dose per fraction is increased while number of fractions is reduced.

1.2.3 Quantitative Analysis and Modeling of Radiation Effects in Normal Tissue and Tumor

Although the LQ model has been well established and is capable of accurately modeling radiation effects on a cellular level, the response of normal tissue as a structure is more complicated. Unlike tumors, for normal tissue and organ, levels of organization cannot be ignored. This implies that the distribution of radiation dose within the normal tissue becomes a rather important factor. In particular organs may have different volume responses based on their unique physiological structures. For example, the spinal cord loses its functionality if one of its elements is incapacitated. This sensitivity to local damage makes organ response highly dependent on the maximum dose within its volume. In contrast, lung is generally less sensitive to maximum dose because loss of functionality in part of lung can be compensated by other parts of the lung. Mean lung dose, a measure of damage to the entire lung volume, is a more predictive value of post RT lung toxicities. Thus the dose volume histogram (DVH) is introduced to give an quantitative representation of fractional volume irradiated at each dose level for different organs.

A typical example of DVH for normal lung and planning target volume (PTV, see defined in section 1.3.1) is shown in Figure 1.3. In this example of lung cancer patient treated with 3D Conformal Radiation Therapy (CRT), the DVH shows

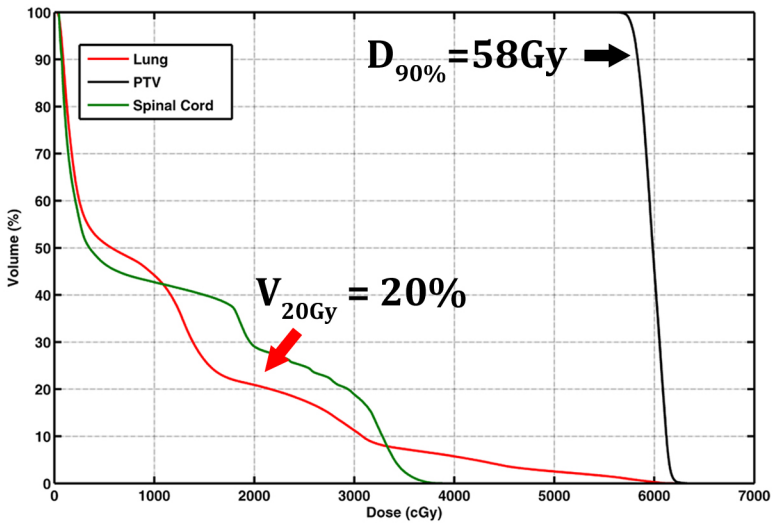

Figure 1.3: Sample DVH of a 3D-conformal RT plan

Table 1.1: Lung tissue tolerance reported in Emami study

Tolerable Dose	Fraction of irradiated volume		
	1/3	2/3	3/3
$TD_{5/5}$(cGy)	4500	3000	1750
$TD_{50/5}$(cGy)	6500	4000	2450

that 20% of normal lung volume receives at least 20Gy, whereas 90% of the PTV receives at least 58Gy.

DVH are routinely used to evaluate treatment plans, analyse and predict clinical outcomes such as early/late normal tissue toxicities and tumor control rate. Based on the consensus of clinical experience, rather than actual clinical outcome data, the most widely used set of tolerance doses delivered to fractional volume of normal tissues was reported by Emami et al [7]. In this study, $TD_{5/5}$ and $TD_{50/5}$, tolerance dose lead to 5% and 50% chance of developing toxicities in five years were reported as uniformly delivered to one third, two thirds or whole volume (Table 1.1).

In the Emami study, tolerance doses and toxicities were reported for uniform irradiation of partial volumes based on comprehensive expert review of clinical data. However, in reality, organs are often irradiated with a non-uniform dose. Therefore, in clinical practice there is a disconnect between the Emami recommendations and realistic DVH. To circumvent this a DVH reduction method was proposed by Kutcher et al [8] along with the Emami study to describe the effect of inhomogeneous dose on healthy tissue. Using this method, a continuous DVH can be reduced to a single value of dose (effective dose) delivered to whole volume which will have same biological effect on tissue as the inhomogeneous dose distribution:

$$D_{eff} = \left(\frac{1}{M} \sum_{i=1}^{M} D_i^{1/n} \right)^n$$

D_{eff} is the effective dose. D_i is dose to voxel i and M is the number of voxels. n is the parameter describing strength of volume effect. For the purpose of clinical use, it was calculated by fitting the Emami data. The value of this parameter reflects sensitivity of organ response to maximum dose or mean dose. For example if n approaches zero an organ is sensitive to the maximum dose such as spinal cord. D_{eff} for these organs will be close to maximum dose in the DVH. In contrast, for organs which are capable of compensating for function loss in partial volume, e.g. lung, the value of n approaches unity. For n=1 D_{eff} is equal mean dose.

The effective dose, D_{eff}, concept is based on reducing a clinical DVH to a single step DVH - dose D_{eff} to whole volume. An alternative concept of effective volume V_{eff} was also proposed [8]. Similar to D_{eff} which has the same effect if uniformly delivered to the entire volume, V_{eff} is the partial volume receiving maximum dose in the DVH which will also lead to the same biological effect as clinical DVH. When comparing different treatment plans, V_{eff} is a straightforward metric of relative risk of developing normal tissue toxicities. Various dose escalation studies have used V_{eff} to stratify patients into different risk groups and treated with different levels of doses. Kutcer-Burman expression for V_{eff} is:

$$V_{eff} = \sum_{i=1}^{M} \frac{V_i}{V_{total}} \left(D_i / D_{max} \right)^{1/n}$$

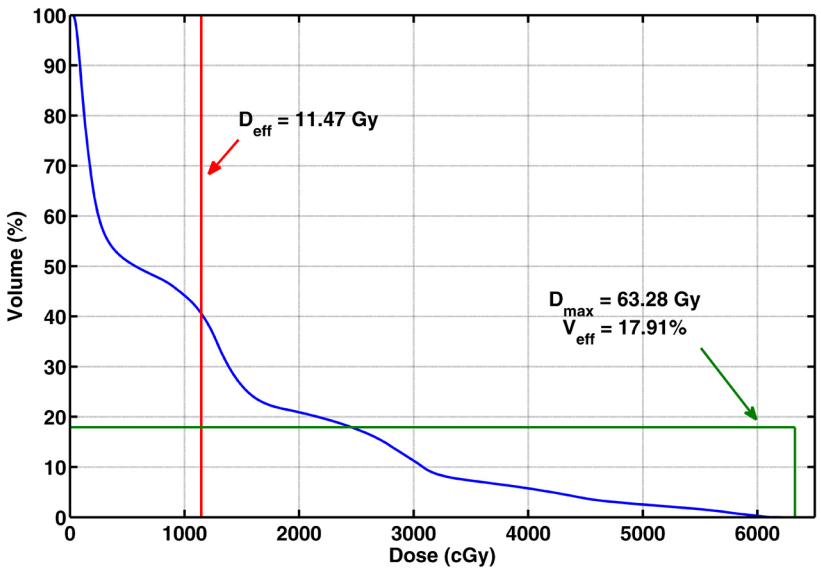

Figure 1.4: V_{eff} and D_{eff} for lung calculated from the DVH in Figure 1.3

where V_i and D_i is the volume and dose of voxel i, M is the total number of voxels, V_{total} is the volume of the structure, D_{max} is the maximum dose in this structure.

Using the DVH reduction method, the effect of inhomogeneous dose distribution in the organ can be represented by the effective dose D_{eff}(Figure 1.4). Thus it is possible to reduce the complexity of data and correlate effective dose with clinical outcome such as probabilities of early and late normal tissue toxicities. Using the DVH reduction method and effective dose D_{eff}, Burman et al [9] fitted a Lyman model to the tolerance dose corresponding to 5% and 50% incidence of complications from the Emami study. Thus it became feasible to estimate the normal tissue complication probability (NTCP) for an arbitrary inhomogeneous dose distribution using the Lyman model:

$$NTCP = \frac{1}{\sqrt{2\pi}} \int_{-\infty}^{t} exp(-\frac{u^2}{2}) du$$

$$t = \frac{D_{eff} - D_{50}}{D_{50} \times m}$$

where D_{50} is the dose to whole organ volume corresponding to a 50% probability of toxicity.

This Lyman-Kutcher-Burman (LKB) model combining Lyman model with Kutcher -Burman DVH reduction method remains the most popular NTCP model. It does not employ a sophisticated mechanistic model to represent dose response of the normal tissue, meanwhile its mathematical form is simple and flexible to model the dose-volume response of various types of organs. It is generally regarded as a good fit for most organs.

Note that the concept of effective dose can also be applied to the dose distribution in tumor where n takes negative values. For tumor response the reciprocal of n, $a = 1/n$, indicates sensitivity to cold spots. For tumors characterized by $a \approx -5$ the sensitivity to cold spots is moderate and tumor is radioresponsive. If $a \approx -20$ tumor is aggressive at local control is sensitive to cold spots. In an extreme case of $a \approx -50$ the probability of recurrence is dominated by a cold spot [10].

For normal tissues models other than the LKB have been also proposed to describe the basic sigmoid function to fit NTCP as well TCP (Tumor Control Probability) dose-response. For example a log-logistic function has been used [11]:

$$NTCP = \frac{1}{1 + \left(\frac{D}{D_{50}}\right)^{4\gamma_{50}}}$$

$$TCP = \frac{1}{1 + \left(\frac{D}{D_{50}}\right)^{4\gamma_{50}}}$$

where γ_{50} is the normalized slope of NTCP or TCP at D_{50}.

After its publication in the early 1990s, the Emami study has become a landmark study in radiation oncology. Since then retrospective analysis and modeling of radiation effect on normal tissue has become an increasingly popular topic. Although these above mentioned concepts such as DVH reduction, TCP, NTCP, etc., are important and indispensible in a research study, conventional dose volume indices such as V_{20Gy} are still routinely used in the clinic as a guideline for RT treatment planning. It would be worthwhile to note that the DVH constraints suggested in the Emami study has been recently updated by the QUANTEC study

Table 1.2: Definition of target responses in RECIST

Complete Response	Disappearance of all target lesions [1]
Partial Response	At least a 30% decrease in the sum of the largest diameter of all target lesions
Progressive Disease	At least a 20% increase in the sum of the largest diameter of all target lesions
Stable Disease	Insufficient shrinkage or increase to qualify for partial response or progressive disease

(QUantitative Analysis of Normal Tissue Effects in the Clinic)[12]. This QUANTEC study analyzed actual clinical data reported in the last two decades since the Emami study, provided updated DVH constraints correlated with end-point specific tissue toxicities and suggested a new set of parameters for the modeling of tissue responses.

These mathematical models correlate radiation dose to clinical outcome from a physicist's point of view, whereas the definition of clinical outcome such as tumor response and various acute/late normal tissue toxicities need to be defined from a physician's perspective. A general consensus has been reached in the definition of solid tumor responses. According to the criteria of Response Evaluation Criteria in Solid Tumors (RECIST)[12], target lesion is defined as the sume of all measureable lesions (largest diameter $>$20 mm in conventional techniques, such as chest X-ray, or $>$10mm in spiral CT scans) up to five lesions per organ and 10 lesions in total. The sum of the longest diameters of all target lesions is recorded as baseline to evaluate tumor response to treatment. All other lesions are identified as non-target lesions. Based on this, the response of each target lesion can be categorized in to complete response, partial response, progressive disease and stable disease (Table 1.2).

The overall response can be further defined based on all possible combinations

[1] Measurements of non-target lesions are not required, meanwhile the definitions of responses in non-target lesions are different.

of tumor responses in target/non-target lesions and whether or not new lesions are apparent. In radiation oncology studies, the portion of patients survived without tumor progression at each follow-up (progression free survival) or time to progression is also reported as a measure of the tumor response in a population.

The grading systems of adverse events caused by normal tissue toxicities are proposed in several studies such as Common Terminology Criteria of Adverse Events (CTCAE Version 3.0)[13], Radiation Therapy Oncology Group (RTOG) acute/late morbidity scoring schema [14], South West Oncology Group (SWOG) toxicity criteria [15] and LENT SOMA table (Late Effects in Normal Tissue, Subjective Objective Management Analytical scale) [16]. In general, Grade 0 suggests no adverse effect, Grade 1 toxicities are minor and require minimum medical attention whereas Grade 5 suggests the toxicity caused the death of the patient. The definitions of Grade 1$\sim$4 toxicities may vary in each system (Table 1.3).

In clinical studies Grade 1 toxicities are typically regarded as not clinically important because these are either asymptomatic or causing minor discomfort. Even if symptomatic they can be managed by non-prescription medication and do not require intervention. Grade 2 or higher complications, e.g. severe cough requiring prescribed medication, are regarded as clinically significant. Dose-volume-response models shown above as they are used in clinical practice are designed to avoid severe toxicities. Therefore the ordinal endpoint, the grade of toxicity, is often dichotomized for the purpose of dose-volume-response analysis. The "event" of observing toxicity is therefore defined as toxicity grade x or higher. The threshold of Grade 2 or higher is often used, however incidence of severe complications, Grade 3 or higher has also been reported [17].

1.3 Radiation Therapy for Lung Cancer Patients

1.3.1 CT Simulation and Volume Definitions

In clinical practice, CT simulation of the patient is performed for the purpose of RT treatment planning. The aim of simulation is to localize tumor volume in three dimensions and setup radiation fields relative to the patient's anatomy. In CT sim-

[2] *Abbreviation*: ADL = Activity of Daily Life

Table 1.3: Definition of lung toxicities in different grading systems

Toxicity	Grade			
	1	2	3	4
Lung acute mobidity (RTOG)	Mild symptoms of dry cough or dyspnea on exertion	Persistent cough requiring narcotic, antitussive agents/ dyspnea with minimal effort but not at rest	Severe cough unresponsive to narcotic antitussive agent or dyspnea at rest/ clinical or radiologic evidence of acute pneumonitis/ intermittent oxygen or steroids may be required	Severe respiratory insufficiency/ continuous oxygen or assisted ventilation
Pulmonary fibrosis (SWOG)	Radiographic fibrosis changes, no symptoms		changes with symptoms	
Pulmonary fibrosis (LENT-SOMA)	Radiological abnormality	Patchy dense on radiograph	Dense confluent radiographic changes limited to radiation field	Dense fibrosis, severe scarring & major retraction of normal lung
Pneumonitis (CTCAE V3.0)	Asymptomatic, radiographic findings only	Symptomatic, not interfering with ADL[2]	Symptomatic, interfering with ADL; O_2 indicated	Life-threatening ventilatory support indicated
Lung function (LENT-SOMA)	10% - 25% reduction of respiration volume and/or diffusion capacity	25% - 50% reduction of respiration volume and/or diffusion capacity	50% - 75% reduction of respiration volume and/or diffusion capacity	$>$ 75% reduction of respiration volume and/or diffusion capacity

ulation, the patient is scanned in the treatment position with radio-opaque markers placed on skin and aligned to the positioning laser system. The same positioning laser system is also installed with the Linear Accelerator (LINAC) which is used to treat the patient. Thus the exact geometry and position of patient during the treatment can be "simulated" in this CT scan. These radio-opaque markers which are visible on the CT scans provide a reference of tumor and other organs' position. The centre of radiation field as well as its shape and angle are set relative to these reference points in the treatment planning. The contours of tumor and other organs can be drawn on this CT scan and subsequently used for treatment planning, thus this CT scan is also named as "planning CT scan".

In order to account for specific features of tumor biology and geometric uncertainties associated with radiation therapy, a set of definitions of target volume in radiation therapy was proposed by the International Commission on Radiation Units and measurements (ICRU). As defined in ICRU Report 50 [18], Gross Tumor Volume (GTV) can be contoured as *"the gross palpable or visible/demonstrable extent and locations of malignant growth"*. In order to account for microscopic malignances not visible on a CT scan, the Clinical Target Volume (CTV) which is *"a tissue volume that contains a demonstrable GTV and/or subclinical microscopic malignant disease, which has to be eliminated"* can be contoured by extending GTV with a margin. The goal of radiation therapy is to ensure that the CTV receives a curative dose prescribed by the radiation oncologists. However, undesired underdose (cold spots) in the CTV might happen due to the geometrical uncertainties of patient set-up, intra- and inter-fraction organ motion and deformation during the treatment which will lead to the failure of tumor control. Thus a geometrical volume concept: Planning Target Volume (PTV) was suggested in ICRU Report 50 [18]: *"The Planning Target Volume (PTV) is a geometrical concept, and it is defined to select appropriate beam sizes and beam arrangements, taking into consideration the net effect of all the possible geometrical variations and inaccuracies in order to ensure that the prescribed dose is actually absorbed in the CTV"*. In practice, PTV is usually contoured as CTV plus a safety margin with the size of margin dependent on tumor site and clinical protocol used (Figure 1.5). For lung cancer patients, tumor motion due to breathing motion is substantial. For the lung base (inferior lung) or mid-lung this motion correlates with diaphragm

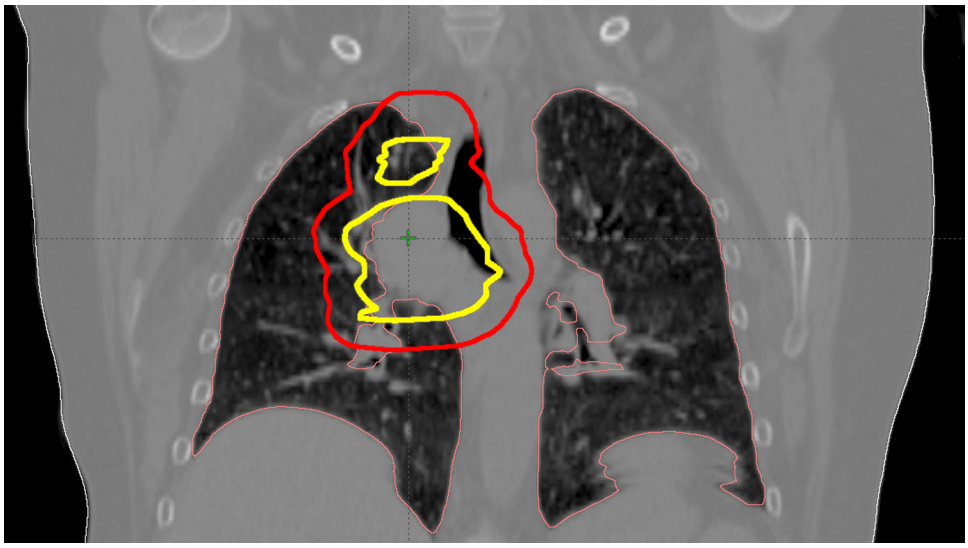

Figure 1.5: Coronal view of GTV(yellow) and PTV(red) as defined in ICRU Report 50[18]

motion, thus the margin along superior-inferior direction is usually larger than the margin on lateral direction. For lung apex (superior lung) lateral motion is more pronounced. However, if advanced methods, such as respiration gating or tumor tracking are used, the margins can be reduced.

After target volumes and organs at risk (OAR) are contoured, the next step of treatment planning is to select an optimal setup of radiation fields and beam intensities to deliver desired dose to the target while satisfying dose volume constraints on OARs.

1.3.2 Treatment Modalities and Techniques

Medical Linear Accelerator

Most lung cancer patients are treated using megavoltage (MV) X-rays from a medical linear accelerator (LINAC). The schematic of a LINAC is shown in the Figure 1.6

Electrons are emitted from the electron gun with an initial energy around 50keV. Microwaves produced from the klystron or magnetron are fed into the waveguide

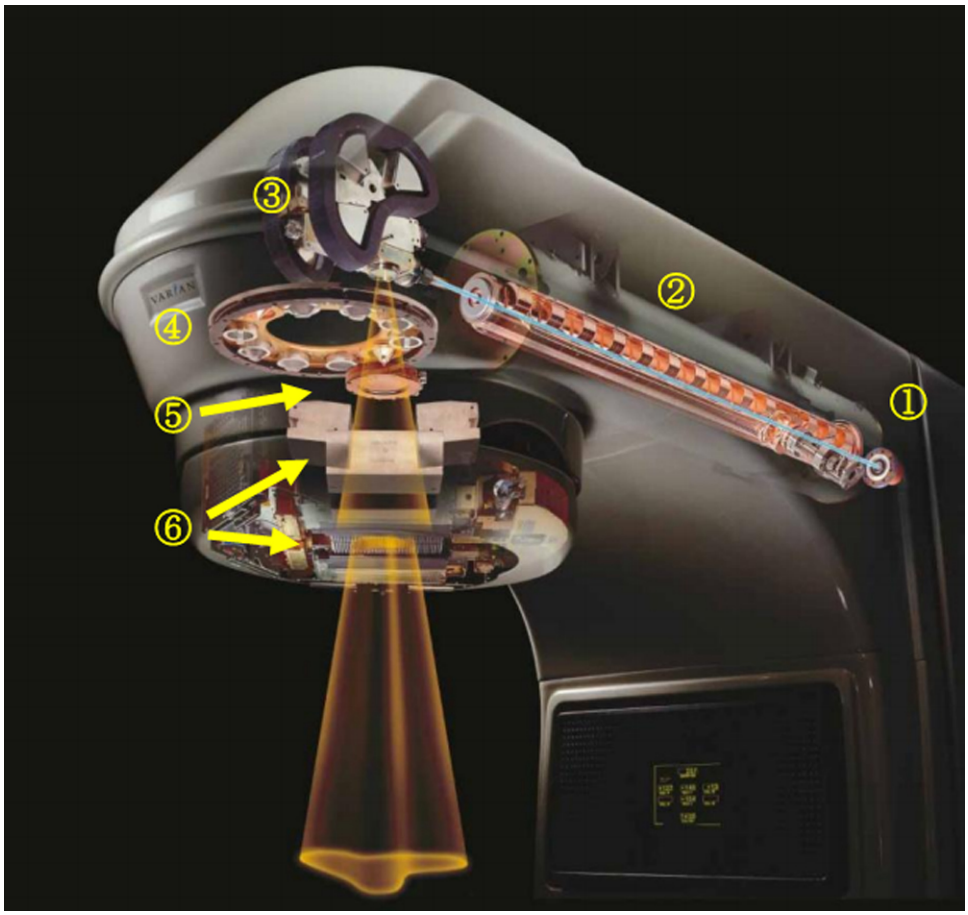

Figure 1.6: Cross section view of a LINAC (image from Varian Inc) including: (1) electron beam, (2) waveguide, (3) bending magnet, (4) a tray of flattening filters used at different photon energies, (5) two sets of ion-chambers monitoring the radiation output, (6) two pair of jaws (up) and multi-leaf collimators(bottom)

with coupled cavities thus generating a standing or traveling electromagnetic wave. The electrons injected into the waveguide can be accelerated to 4$\sim$25MeV before exiting the waveguide. A bending magnet is placed at the end of waveguide to bend electron beams by 270 degrees (or 90 degrees depending on the manufacturer and energy of electrons) before hitting the high density target. The bending of the electron beam and filtering slits are designed to allow electrons only in certain energy range to hit the target thus controlling the energy of output X-rays. Most of the high energy X-rays emitted from the target are generated from the Bremsstrahlung process. For electrons in the MeV energy range Bremsstrahlung photons are predominantly produced in forward direction. A flattening filter and two pair of collimators are placed along the path of the X-ray to modulate the photon beams with uniform intensity and desired rectangular field size.

Multi-Leaf Collimator (MLC)

A Multi-Leaf Collimator is often used to fine tune the shape of the photon beams. A typical MLC consists of two banks of leafs with more than 40 pairs of leafs (Figure 1.7). Each leaf can independently move in and out of the radiation field, thus providing various shapes of the field. A Varian Millennium 120 MLC model has 60 pairs of leaves made of high density alloy. The central 40 leaf pairs are 0.5cm wide and the remaining leafs (10 pairs on each side) are 1cm wide. In treatment planning, MLC can be shaped to match the contour of PTV in a Beam's Eye View thus protecting normal tissues around the PTV. The position of the MLC can also be controlled to create non-uniform beam intensity and deliver a more conformal dose to the tumor target.

Treatment Techniques

Currently, 3D conformal radiation therapy (CRT), and intensity modulated radiation therapy (IMRT) are common types of radiation therapy used to treat lung cancer patients.

3D-CRT is the technique used routinely to treat lung cancer. In 3D-CRT, radiation is delivered from 3$\sim$4 gantry angles. At each gantry angle, the shape of radiation beam is collimated by the MLC which is set conformal to the PTV (plus

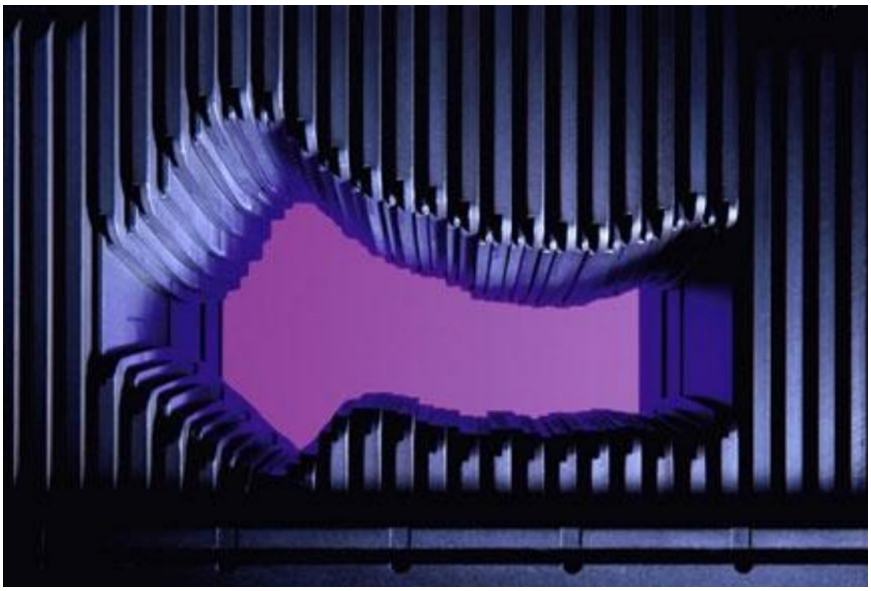

Figure 1.7: Varian Millennium 120 MLC model (image from Varian Inc)

a margin for penumbra) in Beam's Eye View. The radiation beam usually has uniform beam intensity, however in some case, wedges and compensators are placed in the path of X-rays to acquire an oblique beam profile. Forward treatment planning is used in 3D-CRT. The beam orientation, beam modifiers (e.g. wedges) and weights of each field are manually adjusted in iterative fashion to reach an optimal dose distribution.

Compared to 3D-CRT, IMRT is an advanced radiation delivery method which provides better normal tissue sparing and conformal target volume coverage. In IMRT, MLC leaves are used to modulate each individual radiation beam to reach an optimal non-uniform beam intensity which satisfies the goals on tumor dose coverage and normal tissue sparing. This is often done in inverse treatment planning by deploying an algorithm to search for the best fluence profiles. Pre-set gantry angles specific for tumor sites are often used, however, gantry angle optimization may be also utilized. During inverse planning, the goal of treatment planning, i.e. dose coverage of PTV and normal tissue sparing, can be translated into a simple numeric value. The function which quantitatively reflects how close the plan is to the desired plan is called an objective function $f(x)$, where x are the parameters to

modulate the intensity of radiation. This function gives a quantitative measure of the "quality" of the plan. Optimization routine will search for solution to minimize the difference between a desired plan and iteratively tested plans in a trial and error process until it reaches a minimum or maximum. From the mathematical perspective, the process of treatment planning is therefore simplified to an optimization problem:

$$\mathbf{max} f(x) or \mathbf{min} f(x); f \in R, x \in R^n$$

A typical example of planning constraints for PTV would be at least 98% of PTV has to receive at least 95% of prescription dose and maximum dose in PTV cannot exceed 115% of prescription dose. For OARs constraint can be expressed as maximum dose, e.g. no part of spinal cord may receive more than 57 Gy - a typical constraint for spinal cord for RT delivered in 35 fractions. Alternatively dose-volume constraints are imposed, e.g. for rectum not more than 5% may receive 75 Gy or more and not more than 15% may receive 70 Gy or more.

The difference between SPECT guided treatment planning and conventional DVH driven planning is essentially how the objective function $f(x)$ is formulated. Information from perfusion SPECT studies can be incorported into this function to allow for better sparing of lung function. This will be covered explicitly in Chapter 4.

SBRT is a new technique which delivers a hypofractionated dose, 12Gy/fraction $\times$ 4 fractions or 20Gy/fraction in 3 fractions rather than conventional 2Gy/fraction $\times$ 30 fractions in 3D-CRT and IMRT. Patients with single (less than 5 cm in largest dimension), N0 (no regional lymph node metastasis), M0 (no distant metastasis), peripheral (bronchial tree plus 2 cm margin constitutes an exclusion zone) tumors are eligible. RT is delivered using multiple beams. The RTOG 0618 phase II SBRT trial specifies that non-opposing non-coplanar fields are preferable. At least seven, preferably $\geq$ 10 fields of roughly equal weighting are recommended in this study [19]. The high dose volume in normal tissues can thereby be significantly reduced by using multiple non-coplanar radiation beams. SBRT protocols also require advanced image-guidance and motion management. This in its turn allows reducing the PTV margin. The relatively smaller size and shallower position

of tumors in patients eligible for SBRT also contribute to improved lung sparing. Thus a much higher dose can be delivered in each fraction without causing excessive toxicities. SBRT is a promising new technique which demonstrated superior tumor control and toxicities in several clinical trials. However, in the current practice at many clinics, only patients with peripheral tumors are eligible to have SBRT due to the damage to bronchial trees and blood vessels when treating patients with more deep seated tumors. Meanwhile 3D-CRT does not provide much freedom for SPECT guided inverse treatment planning. Thus IMRT naturally becomes the modality of choice to incorporate perfusion SPECT imaging into radiation therapy.

1.4 Clinical Outcomes of Patients Treated with 3D-CRT

1.4.1 General Management of Lung Cancer

Major histologic types of lung cancers include: epidermoid carcinoma, adenocarcinoma, large cell carcinoma and small cell carcinoma. Progression of lung cancer can be divided into three different pathways: local (intrathoracic), regional (lymphatic spread) and distant (extrathoracic spread). Among these histologic types of lung cancer, small cell carcinoma has the fastest doubling time of tumor growth and highest incidence of distant metastasis. Thus management of lung cancer is generally categorized as treating small cell and non-small cell lung cancer (NSCLC). Stage of the cancer can also be classified based on the size, location of primary tumors and the presence of regional (lymphatic) or distant (extrathoracic) metastasis, as proposed by Moutain [20]:

- Stage I: In stage I, the primary tumor is in the lung only (no regional lymph node metastases). Stage I is divided into stages IA and IB, based on the size of the tumor.
- Stage II: In stage II, cancer has either spread to nearby lymph nodes or to any of the following:
  - Chest wall, parietal pleural, diaphragm, phrenic nerve, mediastinal pleura and parital pericardium

Stage II is divided into stage IIA and stage IIB, based on the size of the tumor and whether it has spread to the lymph nodes.

- Stage III: In stage III, cancer has either directly invades any of the following:
  - mediastinum, heart, great vessels, trachea, recurrent laryngeal nerve, esophagus, vertebral body, carina, separate tumor nodule(s) in a different ipsilateral lobe

  or spread to:
  - ipsliateral mediastinal, subcarinal lymph node;
  - contralateral mediastinal, contralateral hilar, scalene, supraclavicular lymph node in the lower neck;

  Stage III is divided into stage IIIA (which is sometimes treated with surgery) and stage IIIB (which is rarely treated with surgery).

- Stage IV: In stage IV, cancer has spread to an organ out of the thorac or to another lobe of the lungs.

In general, lung cancer patients with non-small cell carcinoma should undergo surgery if the tumor is resectable. Meanwhile the use of thoracic 3D-CRT is indicated in suitable patients with inoperable stage I-II or stage III NSCLC and limited stage small cell lung cancer. Current standard of dose fractionation for these patients was established by the RTOG 73-01 Phase III trial conducted in the 1970s [21]. In this trial, the effect of dose fractionation schemes on tumor control and survival was compared in stage III NSCLC patients randomized to receive treatment of 40Gy in 20 daily fractions, 50Gy in 25 fractions and 60Gy in 30 fractions [21]. The standard RT dose was thereafter defined as 60Gy in 30 fractions which gives the lowest local failure rate in this trial (Table 1.4). Median survival and 5-year survival are typically $\sim$10 months and 5% respectively in stage III patients treated with 3D-CRT.

Chemotherapy was later on added to RT to improve tumor control (Table 1.5). It was demonstrated in a Phase III trial that chemotherapy followed by radiation

Table 1.4: Tumor response rates reported from RTOG-7301 trial [21]

	40 Gy	50 Gy	60Gy
Local tumor response rate (complete + partial response)	48%	53%	56%
Incidence of intrathoracic failure	44%	39%	33%

Table 1.5: Results from randomized studies in concurrent chemoirradiation Vs radiation therapy alone for locally advanced NSCLC.

Study	Treatment	Dose (Gy)	Median survival (month)	Two years' survival
Soresi et al [24]	RT alone	50	11	25%
	Weekely chemo + RT		16	40%
Blanke et al [25]	RT alone	60∼65	11.5	13%
	Weekely chemo + RT		10.6	18%

therapy improved survival compared to RT alone [22]. Later Phase III trials revealed that concurrent chemo-radiotherapy, i.e. chemotherapy and radiation therapy administrated at the same time, significantly improved survival compared to chemotherapy followed by radiotherapy in a sequential matter [23]. Median survival and 5 year survival were 16.5 months and 15.8% respectively in concurrent treatment vs. 13.3 months and 8.9% respectively in sequential treatment. Concurrent chemo-radiation therapy has become a standard of care for stage III NSCLC patients treated with curative intent (∼60Gy in 2Gy per fraction).

Imaging modalities, dose calculation algorithms as well as verification systems for patient position, treatment delivery and dosimetry have also advanced considerably in the last two decades. Compared to contouring of gross tumor volumes and lymph nodes on an X-ray portal image, CT based simulation provides 3D-

images with better resolution and allows for more accurate delineation of GTVs. PET scans using ^{18}F-FDG (fluorodeoxyglucose) has been widely used to detect metabolic activities. This allows for detecting small regions of high tracer uptake, e.g. positive nodes, which cannot be resolved on CT. Therefore, a more accurate staging can be made and appropriate patient management chosen. Simple dose calculation algorithms often assume homogeneous medium or use one-dimensional corrections for inhomogeneity, i.e. along the beam path and not accounting for scatter component. Dose distributions for target volumes and normal tissues as "seen" in the treatment planning with these algorithms are not accurate. Unfavorable underdose in PTV is likely to happen due to inadequate corrections for inhomogeneous medium. Also, normal lung is likely to receive larger dose than the planning system shows if dose calculation does not account for photon attenuation. Thus advanced dose calculation algorithms with accurate inhomogeneity corrections are essential to acquire dose distributions especially in intrathoracic irradiations (see Section 4.2.1). Meanwhile several newly developed techniques such as 4D-CT and cone beam CT as well as active breathing control systems provide means to reduce geometrical uncertainties caused by respiration or patient setup errors in daily treatments. Thus a smaller safety margin around the GTV can be used which reduces the volume of normal lungs receiving high doses and thereby reduces the risk of pulmonary toxicities.

1.4.2 Clinical Outcome: Tumor Control

Individual tumor response to irradiation can be measured by the change of tumor size through repeated CT imaging throughout or after the treatment. Guckenberger et al.[26] and Bral et al.[27] reported a continuous 1.2%$\sim$1.74%/day decrease of the tumor volume in stage III patients treated with concurrent chemoirradiation (60-67.2Gy in 30 fractions). Feng et al.[28] also reported an average -26% (+15% to -75%) total change of the GTV volumes in stage I-III NSCLC patients. Metabolic activity measured by the tracer uptake and standard uptake volume (SUV) in ^{18}F-FDG PET imaging are also used as a surrogate of local response to treatment. Mean reduction in the gross tumor volume as defined by the tracer uptake in PET images ranged from 40$\sim$60% [27, 28]. These findings also

Table 1.6: D_{50} and γ_{50} of locoregional progression free survival at 12, 24 and 30 months

	12 months	24 months	30 months
D_{50}	64±7 Gy	72±2.5 Gy	84.5±8 Gy
$\gamma 50$	1.3 (0.9∼3)	2.0 (1∼4)	1.5 (0.8∼3)

suggests potential benefits of adapting treatment plans accounting for the shrinkage of tumor volumes [26, 28, 29].

However, overall tumor control is still poor. In the dose escalation trial conducted in the University of Michigan, Ann Arbor, 89 of the 108 patients developed tumor progression post treatment [30]. 65 of them had local or regional failure. The 5-year locoregional progression-free survival was 29% despite the fact that these patients were treated with dose from 63 to over 90Gy. Total dose was found to be a statistically significant factor correlated to locoregional progression-free survival. In the group of patients treated with 67, 80, and 97 Gy, the 5-year locoregional progression-free survival rates were 12%, 35%, and 49% respectively [30].

The rate of locoregional progression-free survival (assumed equivalent to TCP) can be estimated using the logistic TCP models.

$$TCP = \frac{1}{1 + \left(\frac{D_{50}}{D}\right)^{4\gamma_{50}}}$$

Martel et al.[31] reported D_{50}, dose at 50% locoregional progression free survival and γ_{50}, the normalized slope of sigmoid-shaped dose response curve at 12, 24 and 30 months post treatment (Table 1.6).

It was found that currently used dose fractionations (30∼60Gy in 30 fractions) are insufficient to yield significant probability of tumor control (>40%) (Figure 1.8). γ_{50} which gives approximate percent increase in TCP per increase in percent dose evaluated at D_{50} was reported approximately 1.3∼2. It also agrees with the finding that approximately 1% gain in TCP per 1 Gy increase in the range of 63-69Gy [30]. This suggests that larger dose (>84Gy) is more favorable of longer (>30 months) locoregional progression free survival. Several dose escalation trials have been conducted to explore opportunities to improve tumor control

and overall survival [26–30, 32–34].

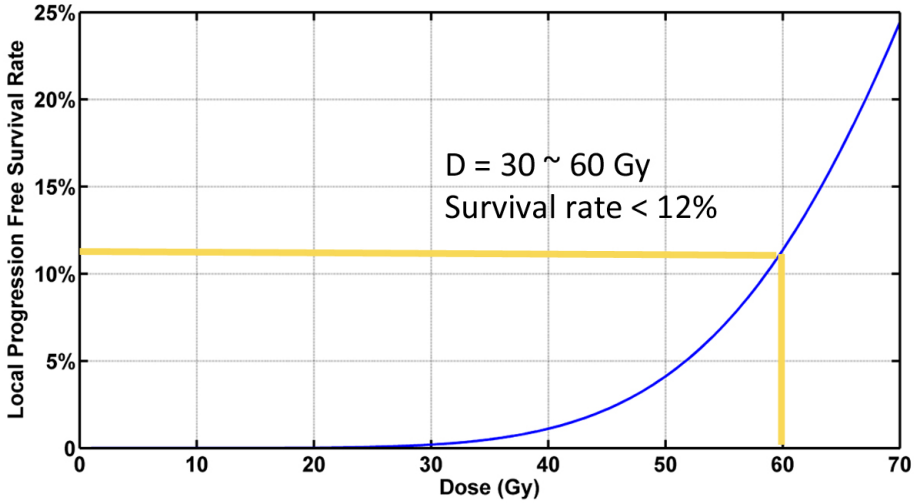

Figure 1.8: 30 months' locoregional progression free survival as a function of dose in logistic model (D_{50} = 84.5 Gy, γ_{50} = 1.5)

1.4.3 Clinical Outcome: Normal Tissue Toxicities

Common toxicities seen after the 3D-CRT treatment are associated with lung, skin and esophagus. Among them RT-induced lung injury is the most clinically significant one and the leading dose limiting toxicity (DLT) when escalating dose delivered to the tumor. Approximately 5-20% of patients treated with radiation will develop a degree of symptomatic RT-induced lung injury such as pneumonitis and fibrosis. Radiation Pneumonitis (RP) typically occurs 1-6 months post radiation treatment. It is an acute inflammation of lung tissue causing shortness of breath, cough and occasionally fever. Pulmonary fibrosis, a later radiation side effect, results in symptoms such as progressive dyspnea and cough that may develop months to years post treatment. The degree of these toxicities varies from mild to life threatening. Meanwhile, significantly more patients will experience sub-clinical RT-induced injuries without clinical symptom, such as reductions in pulmonary function tests, abnormalities seen on radiographic scans (CT, perfusion/ventilation scans).

Table 1.7: Dose-volume-outcome data suggested in the QUANTEC study [38]

Endpoint	Dose-volume parameters	Rate
Symptomatic penumonitis	V_{20Gy} <30%	<20%
	Mean lung dose = 7Gy	5%
	Mean lung dose = 13Gy	10%
	Mean lung dose = 20Gy	20%
	Mean lung dose = 24Gy	30%
	Mean lung dose = 27Gy	40%

A large amount of retrospective dose volume histogram (DVH) analysis suggest that V_{xGy} values (percentage of lung volumes irradiated no less than x Gy) are correlated with RP risks [17, 35–37]. In these studies, the dose level in predictive V_{xGy} values ranged from 5∼40Gy which suggests a gradual response of RP risks as a function of radiation dose, i.e. there is no threshold dose value below which there is no risk. Among the variety of reported V_{xGy} values, V_{5Gy} and V_{20Gy} are usually considered as more strongly correlated to RP risks and often used as clinical constraints for treatment planning. For example, the typical constraints when treating lung cancer patients with prescription dose of 60Gy/30 fractions in Vancouver Cancer Centre is that less than 35% of the both lung minus GTV or PTV receives more than 20Gy, i.e. V_{20Gy} <35%. When treating patients with IMRT, due to the large portion of low dose volume usually seen in IMRT, constraints on V_{5Gy} are also used in treatment planning.

LKB model has been used to predict normal tissue complication probabilities for RP. It was found that TD_{50} is depending on the grade of RP being considered. However, the volume parameter n which represents tissue characteristics is very consistent. In the QUANTEC review, n was estimated to be 1.03 with 95% confidence interval from 0.67∼1.39 [38]. This suggests that lung is a parallel organ and more sensitive to mean dose rather than local dose hotspots. Thus mean lung dose (MLD) model as a simple and effective tool has also been widely adopted to predict RP probabilities. A gradual response of RP with increased MLD was also found which, again, confirmed that there is no safe dose level below which RP will

not occur. RP risks as a function of MLD can be expressed as:

$$p = \frac{exp(-3.87 + 0.126 \times MLD)}{1 + exp(-3.87 + 0.126 \times MLD)}$$

This fit gives the dose related to 50% chance of symptomatic pneumonitis, is 30.8Gy and the renormalized slope of dose response curve is 0.97. This suggests that the rate of pneumonitis can be reduced by approximately 3% if 1Gy reduction in mean lung dose at 30Gy level can be achieved (1Gy/30Gy $\times$ 0.97 $\approx$ 3%). In the QUANTEC study, it was suggested to limit V_{20Gy} to $\leq$ 30-35% and MLD to $\leq$ 20-23Gy in order to limit the risk of symptomatic RP to $\leq$ 20% in conventional 3D-CRT with 2Gy/fraction [38] (Table 1.7).

1.4.4 Dose Escalation Studies for Lung Cancer Patients

RT-induced lung injury is not only the most common toxicities in lung cancer patients treated with RT, it is also the major limiting factor which prohibits further escalating tumor dose to achieve a better tumor control. Bral et al.[27] reported that, when dose prescribed to the tumor was escalated to 70.5Gy in 30 fractions, $\geq$ Grade 2 lung toxicities were observed in 43% of patients within 90 days of treatment. Although Grade 2 acute esophageal toxicity was seen in 33% of patients, late toxicities were exclusively related to lung injury (40% of patients experienced $\geq$ Grade 2 lung toxicities 90 days after treatment). Toxicity report from RTOG-9311 dose escalation trial also reported that lung injuries consists of most of late toxicities when prescription dose was escalated to 70.9-90.3Gy [4]. In the dose escalation trial conducted by Belderbos et al.[4] at Netherland Cancer Institute, maximum tolerated dose (MTD) was successfully escalated to 74.25 $\sim$ 94.5Gy for patients in different risk groups. Five out of the nine dose limiting toxicities are related to lung injury (four Grade 3 RP, one Grade 5 RP). More than 50% of the patients experienced $\geq$ Grade 3 shortness of breath three months after the treatment. Note that administrating chemotherapy concurrently with radiation therapy significantly increased lung toxicities. Schild et al [32] reported that maximum tolerated dose was 74Gy in a Phase I dose escalation trial with concurrent chemotherapy. Whereas it was reported that the prescription dose can be safely escalated to more than 90Gy without concurrent chemotherapy in the patient group with least risk of

RP[3, 4]. Thus more effective sparing of lung and pulmonary function are required in order to reduce lung toxicities and escalate the dose currently used in RT.

1.5 Motivations of Incorporating Perfusion SPECT Imaging into Radiation Therapy

As discussed in the previous section, for most patients undergoing RT, DVH-based dosimetric parameters such as the mean lung dose (MLD) and V_{20Gy} (volume of lung receiving at least 20Gy) are used to estimate the risk of RT-associated lung injury. In RT planning the treatment plan is optimized to cover the planning target volume (PTV) usually by the 95% isodose line while fulfilling constraints placed on the dose-volume distribution to normal tissues, (including MLD and V_{20Gy}), to avoid severe (Grade 3+) pulmonary toxicity. However, these metrics are imperfect predictors. MLD and V_{20Gy} are easily calculated from a Dose Volume Histogram (DVH), but do not account for spatial information, and assume homogeneous function distribution in the lung volume. However in normal lung, the volume at the base of the lung has greater perfusion and contributes more to lung function than the apex. In addition, many patients with lung cancer have background lung disease such as chronic bronchitis and emphysema secondary to cigarette smoking again causing inhomogeneous perfusion. Tumor progression may also cause temporal shutdown of pulmonary blood vessels leading to inhomogeneous lung perfusion (Figure 1.9). The perfusion images in Figure 1.9 suggest that no perfusion/blood flow can be found near tumor (GTV) due to tumor pressure against the blood vessels. This is further confirmed by this patient's follow up scan after the treatment where tumor shrinkage resulted in re-opening of the blood vessels and re-perfusion was found in previously un-perfused areas. Yorke et al.[39] reported that MLD to the lower half of the lung is more predictive of RP than MLD to upper half lung, and Graham et al.[17] noted increased RP in patients with lower lobe tumors versus upper lobe tumors. Tumors of the lung base were associated with a statistically significant higher risk of RP than the apices in a study by Seppenwoolde et al.[40]. The authors also demonstrated that MLD alone was insufficient to predict the incidence of radiation pneumonitis. Thus the MLD and V20Gy alone may not be the best predictive markers for RP. Detailed information about the distribution of lung

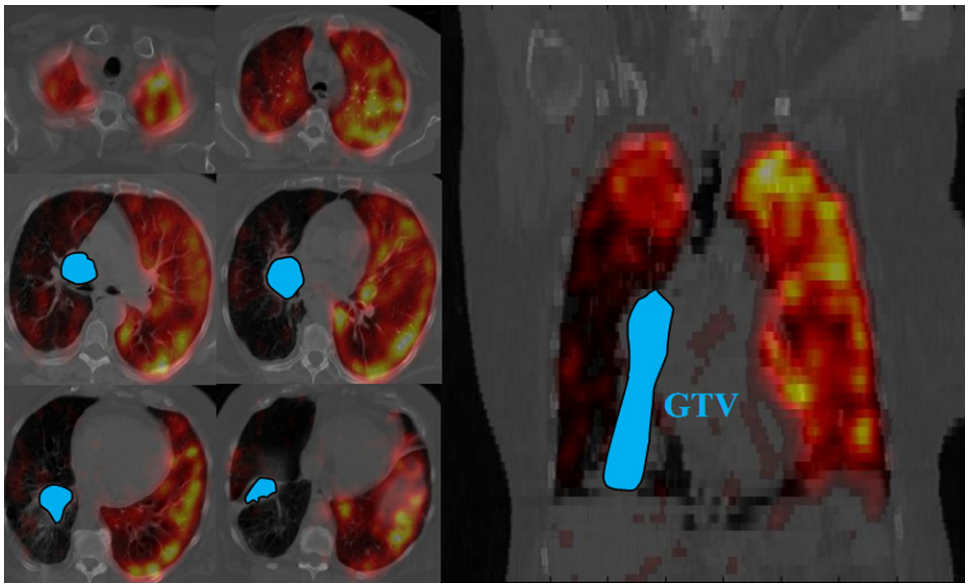

Figure 1.9: Transaxial(left) and coronal(right) views of lung perfusion overlaid with CT images. Color index from red to yellow corrsponding to low and high lung perfusion

function would be especially important for patients with lung tumors. Incorporated into radiation treatment planning, functional information could potentially lead to improvements in outcomes.

^{99m}Tc-macroaggregated albumin (MAA) SPECT is a means of imaging the pulmonary microvasculature as a surrogate marker for lung function. The use of SPECT to evaluate lung function for the purpose of optimizing beam angles was first proposed by Marks et al.[5, 41]. SPECT weighted mean dose (SWMD) [42] and dose function histogram (DFH) [41] were also proposed as effective method to evaluate the impact of radiation on lung functionality, and to provide information for SPECT guided radiation therapy for patients with lung cancer. Lind et al. further reported that SPECT perfusion weighted mean lung dose correlated better with RP than MLD as calculated from a CT scan [43]. Meanwhile, Seppenwoolde et al. also reported that incorporating the local perfusion data with mean regional dose explained the difference in radiosensitivity between posterior and anterior lung [40]. Several studies have demonstrated that when perfusion SPECT was in-

corporated into treatment planning, it was possible to achieve better lung function sparing without compromising dose coverage on the target and volume sparing of the lung [42, 44–47]. These results suggest that through the use of SPECT guided treatment planning, the lung toxicities can be limited to the level currently seen in the clinic while boosting the target dose to a higher level. Thus, it was decided that it would be worthwhile to quantitatively assess the potential benefit of dose escalation using SPECT guided treatment planning and estimate the maximum dose tolerable for different group of patients in this dose escalation study.

1.6 SPECT Program at Vancouver Cancer Centre and Vancouver General Hospital

Upon approval from the research ethics board, the SPECT study jointly implemented by BC Cancer Agency - Vancouver Cancer Centre (VCC) and Vancouver General Hospital (VGH) was initiated in 2008 with the support from the Michael Smith Foundation for Health Research. A team of radiation oncologists, radiologists, medical physicists and therapists was assembled to implement perfusion SPECT imaging into radiation therapy, assess radiation damage on lung perfusion and investigate the potential improvement on clinical outcomes from this modality. The final goal of this project is to initiate a perfusion SPECT guided dose escalation trial for lung cancer patients.

From February 2008 to May 2011, 22 patients were recruited into this study (Table 1.8). All patients were diagnosed with primary lung cancer or intra-thoracic metastatic cancers including 18 non-small cell lung cancer patients and 2 small cell cancer patients. Patients enrolled in this study gave a formal consent to have one perfusion SPECT scan (after the RT simulation but prior to the beginning of treatment) as an initial assessment of the lung function. If the physical status of the patient allowed for it, another post-RT SPECT was acquired 3$\sim$4 months after the treatment as an assessment of radiation damage to lung function. Eight patients were excluded from this study for several reasons including:

1. Additional radiation treatment requested by treating oncologists between two scans;

Table 1.8: Characteristics of the enrolled patients

	Patients with 1^{st} SPECT scan	Patients with both 1^{st} and 2^{nd} SPECT scans
Total number of patients	22	14
Histology/Cytology:		
NSCLC[3]	18	12
SCLC	2	1
Lung metastasis	2	1
Sex:		
Male	14	7
Female	8	7
Age:		
Min	48	48
Median	65	66
Max	87	87
Type of Tx		
Palliative 3D-CRT	7	3
Radical 3D-CRT	8	6
SBRT	7	5

2. One patient couldn't tolerate the toxicity of radiation therapy after 10 fractions, thus radiation therapy is cancelled;

3. Two patient deceased shortly after the treatment;

4. Four patients could not make travel arrangement or declined the 2nd scan for personal reasons.

Most of the patients in this study received radiation therapy in Vancouver Cancer Centre with perfusion SPECT scans conducted in Vancouver General Hospital except two patients who were treated and SPECT-scanned in Fraser Valley Cancer Centre and Surrey Memorial Hospital respectively. During the RT simulation,

[3]*Abbreviation*: NSCLC = Non-small cell lung cancer, advanced stage NSCLC patients are mostly treated with conventional fractionaion; SCLC = small cell lung cancer. Palliative 3D-CRT: 3D Conformal RT with palliative intent, typically 20Gy/4 fractions $\sim$ 40Gy/15 fractions; Radical 3D-CRT: 3D Conformal RT with radical intent, typically 50Gy/20 fractions $\sim$ 63Gy/35 fractions; SBRT: Stereotactic Body Radiation Therapy, typically $\sim$48Gy/4 fractions

Figure 1.10: SPECT scan setup (image courtesy of Dr.Anna Thompson)

all patients were immobilized and scanned in the treatment position (supine with head rest and knee supports, arms raised and supported above the head). Patients treated with 3D-CRT were scanned with free breathing, whereas patients receiving SBRT were scanned with abdominal compression. In the simulation, a planning CT was acquired using a Picker^{TM} or GE LightSpeed^{TM} CT scanner, the planning CT images were reconstructed at 0.96 x 0.96 x 5 mm^3 voxel size. Radio-opaque makers were placed on the patients' skin as a reference for contouring structures and treatment setup.

In each case, SPECT scan was acquired following the planning CT scan. Prior to the scan, with the patient in a supine position, 185 MBq of ^{99m}Tc-macroaggregated albumin (MAA) was injected intravenously. The SPECT scanner bed was fitted with the flat couch top used in RT treatment. The same immobilization devices (head rests, arm and knee supports) as during planning CT scan were used to ensure that the patient's position in SPECT scan was consistent with the position in RT treatment (Figure 1.10). The lung perfusion scan was acquired using Infinia-Hawkeye SPECT-CT camera (GE Healthcare) with the low energy high resolution (LEHR) collimator. The detectors were positioned in H-mode (relative angle 180°), the acquisition matrix was 128x128 and a total of 120 projections (60 camera stops per head), with 20s/stop were acquired over a total of 360° camera rotation with a non-circular orbit (NCO). This scan was followed by a low dose CT scan performed with the same SPECT-CT camera. Both SPECT and CT scans were performed

while the patient was free breathing. This low dose CT scan was subsequently used for creation of the patient-specific attenuation map and for planning-CT to SPECT co-registration.

The workflow of incorporating the perfusion SPECT scan into RT planning consists of three parts, which are also components of this project:

1. 3D reconstruction of perfusion SPECT images from the planar projections. In this part of the project, the impact of quantitative SPECT reconstruction on treatment planning was investigated. A robust SPECT based metric of lung function sparing which was not sensitive to SPECT reconstruction algorithms was selected. Results and discussions of this part are presented in Chapter 2.

2. Co-registering perfusion SPECT images with planning CT images to bring both image sets acquired at different location into the same reference system for treatment planning. For this purpose, the accuracy of several image registration algorithms has been evaluated. One of them was chosen as the standard registration algorithms used in this project. (See Chapter 3)

3. Intensity modulated radiation therapy (IMRT) treatment planning based on SPECT images. In this last part of the project, a Direct Aperture Optimization (DAO) based treatment planning program was developed. A planning study comparing SPECT and DVH driven treatment planning was conducted using this program. Safe dose escalation limits were established by comparing SPECT guided RT plans and clinical RT plans. (See Chapter 4).

Chapter 2

SPECT Imaging and the Impact of Image Reconstruction on Treatment Planning

Single Photon Emission Computed Tomography (SPECT) is an imaging modality where functional information about patient's physiology is acquired by recording γ rays (photons) emitted by the radiopharmaceutical injected into the patient's body. Unlike CT or X-ray which use external radioactive sources to measure physical information (attenuation) of the object being scanned, in SPECT imaging these radioactive sources are located inside the patient and bound to specific location of physiological interest. A typical lung perfusion radiopharmaceutical such as ^{99m}Tc-macroaggregated albumin (MAA) consists of aggregated human albumin (MAA) labeled with ^{99m}Tc which is a metastable isotope with 6 hours half-life and emits detectable 140 keV γ rays. MAA is manufactured with more than 90% of particles between 10$\sim$90 micrometers in size and the maximum size not exceeding 150 μm. Immediately after intravenous injection, more than 80% of MAA is trapped in the pulmonary alveolar capillary bed due to its limited size meanwhile γ rays are emitted from ^{99m}Tc labeled on the aggregrated particles. In SPECT, three dimensional images of radiopharmaceutical distribution are reconstructed from the projections recorded at multiple angles around the patient. The distribution of radioactive aggregated particles in the normally perfused lung is uniform throughout

Table 2.1: Examples of radiopharmaceuticals used in clinical SPECT imaging

Radiopharmaceutical	Chemical Componds	Clinical Use
^{99m}Tc-MDP	methylene diphosphonate	Bone metastases
^{99m}Tc-HMPAO	hexamethyl propylene amine oxime	Brain perfusion studies
^{99m}Tc-MIBI	methoxy isobutyl isonitrile	Myocardial perfusion imaging
^{99m}Tc-MAG3	mercapto acetyl tri glycine	Kidney/renal imaging
^{131}I-NaI	NaI (sodium iodide)	Detecting abnormal thyroid anatomy or physiology

the vascular bed, and will produce a uniform image. Areas of reduced perfusion will be revealed by a correspondingly decreased accumulation of the radioactive particles, and these areas are imaged as areas of decreased photon density. Thus using ^{99m}Tc-MAA in SPECT imaging provides indirect measurement of spatial distribution of lung perfusion (blood flow). ^{99m}Tc is the most widely used radioactive isotope in nuclear medicine. Other isotopes such as ^{131}I are also being used. These isotopes can be produced in nuclear reactors or through other approaches. Chemical compounds with different diagnostic intent are also available for use in combination with these isotopes, thus SPECT provides means of imaging various physiological functionalities of human body(Table 2.1).

2.1 Anger Camera

Cameras used in SPECT to record γ ray emissions are usually referred to as Anger cameras since these devices share many essential features of Hal Anger's early design [48]. A typical Anger camera usually consists of a collimator, scintillation crystal (scintillator), array of photomultiplier tubes (PMT) and electronics to collect the data (Figure 2.1).

The purpose of the collimator is to limit the possible directions of γ rays reach-

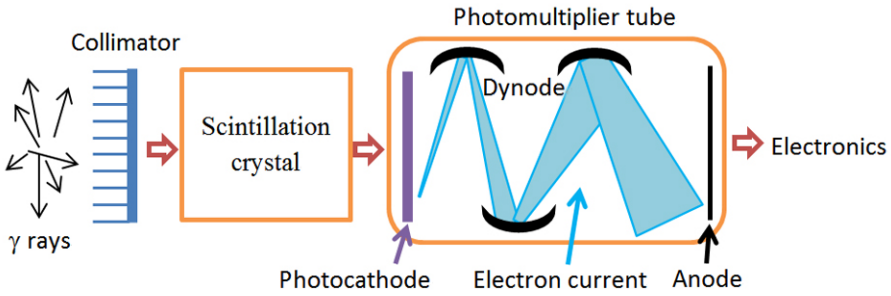

Figure 2.1: Schematic design of the Anger camera

ing the camera, as well as scatterd γ rays. In perfusion SPECT studies, high density (usually lead) septa are usually placed in parallel before the scintillator, thus only photons in the direction approximately orthogonal to the detector plane will be accepted (Figure 2.2a). Depending on the energy of emitted γ rays and desired resolution, four types of parallel-hole collimators are routinely used in nuclear medicine clinics: LEHR (low-energy, high-resolution), LEAP (low-energy, all-purpose), MEAP (medium-energy, all-purpose), and HEAP (high-energy, all-purpose). The septa in MEAP and HEAP are usually thicker to avoid photons with relatively higher energy penetrating the septa and creating artifacts in the image. Meanwhile longer septa provide better resolution, accept less scatter photons, but lower efficiency for collecting emitted photons (Figure 2.2c).

The scintillation crystal absorbs the γ photons and converts some of their energy into visible light photons through a process known as scintillation. During the scintillation process, the energy of γ photons is absorbed by the crystal lattice and transferred to the electrons in the valence bands. The electrons move to higher conduction bands and return to the valence bands through many intermediate energy levels which are created between two bands by intentionally introducing lattice impurities. The energy interval between intermediate energy levels is carefully chosen within the energy range of visible photons, thus visible light is created as a result of γ ray absorption in the scintillation crystal.

The light output from the scintillator is transferred to an array of PMTs through the light guide. Photocathode is a coated plate of photosensitive compound on the front plate of each PMT. Light photons impinged on the photocathode are absorbed

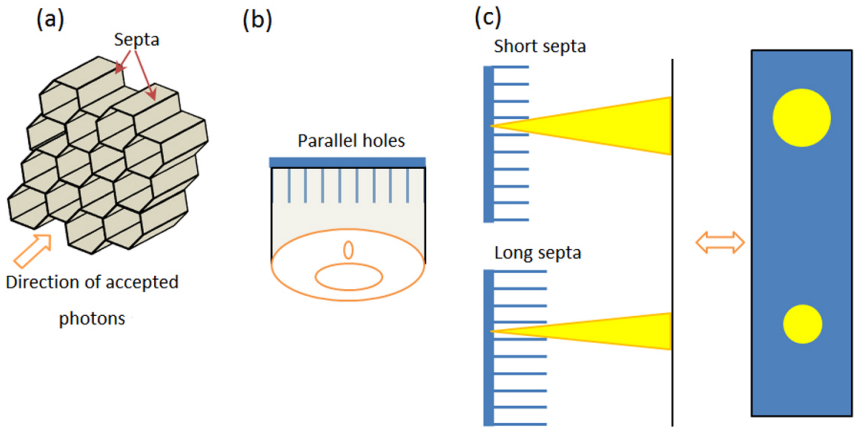

Figure 2.2: Collimator in Anger camera: (a) Design of the septa, (b) Field of view difference between parallel and converging holes; (c) Resolution difference between short and long septa

through the photo-electric process, emitting 1∼3 photoelectrons per photon. Photoelectrons are accelerated by the high voltage in a stepwise fashion by the dynodes placed along the vacuum tube. Each dynode emits 6∼10 secondary electrons when struck by an election. Typically 8∼10 dynodes are used in each PMT, thus the signal can be multiplied by 105∼108 times. The final electron intensity that reaches the anode is proportional to the light output from the scintillator which, in turn, depends on the energy of the absorbed γ photons, thus the energy of the photon triggering this chain of events can be calculated. Only photons in the pre-set energy window will be recorded to generate 2D projection of γ ray emissions. 3D distribution of radio-isotopes can be further reconstructed from the 2D projections.

2.2 Image Reconstruction and Quantitative Correction

2.2.1 Iterative Image Reconstruction Algorithms

Currently for SPECT image reconstruction, filtered back projection (FBP) algorithms is often replaced by iterative reconstruction algorithms including the Ordered Subset Expectation Maximization (OSEM) algorithm [48, 49]. In SPECT image reconstructions, the value of pixel i in the projection space (p_i , $i = 1 \cdots m$)

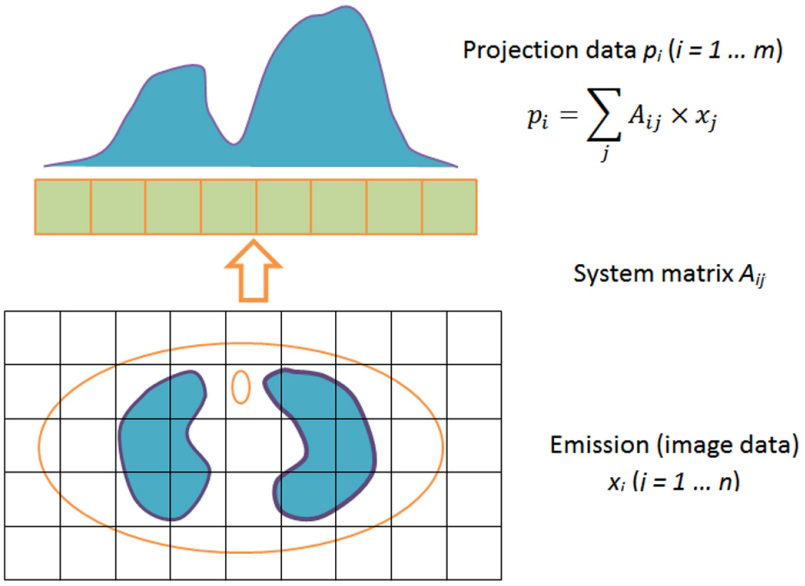

Figure 2.3: Modeling of γ ray projection

corresponds to the sum of detected γ rays originating from all possible pixels of image space (x_j, $j = 1 \cdots n$) to this pixel. The physical process of γ ray projection can be modeled using a system matrix A_{ij} which contains a pixel wise correspondence between image space and projection space (Figure 2.3). This system matrix A_{ij} describes the imaging process, thus prior to developing a specific image reconstruction algorithm, it should be obtained through analytcial calculation of physical process involoved in image acquistion such as attenutation, linear blurring or through Monte Carlo simulation.

Thus the projection data (p_i , $i = 1 \cdots m$) corresponds to the product of the system matrix A_{ij} and the activity in voxel j (x_j, $j = 1 \cdots n$).

$$\begin{bmatrix} p_1 \\ \vdots \\ p_m \end{bmatrix} = \begin{bmatrix} A_{11} & \cdots & A_{1n} \\ \vdots & \ddots & \vdots \\ A_{m1} & \cdots & A_{mn} \end{bmatrix} \begin{bmatrix} x_1 \\ \vdots \\ x_n \end{bmatrix}$$

The problem of image reconstruction becomes solving x_j from A_{ij} and p_i in

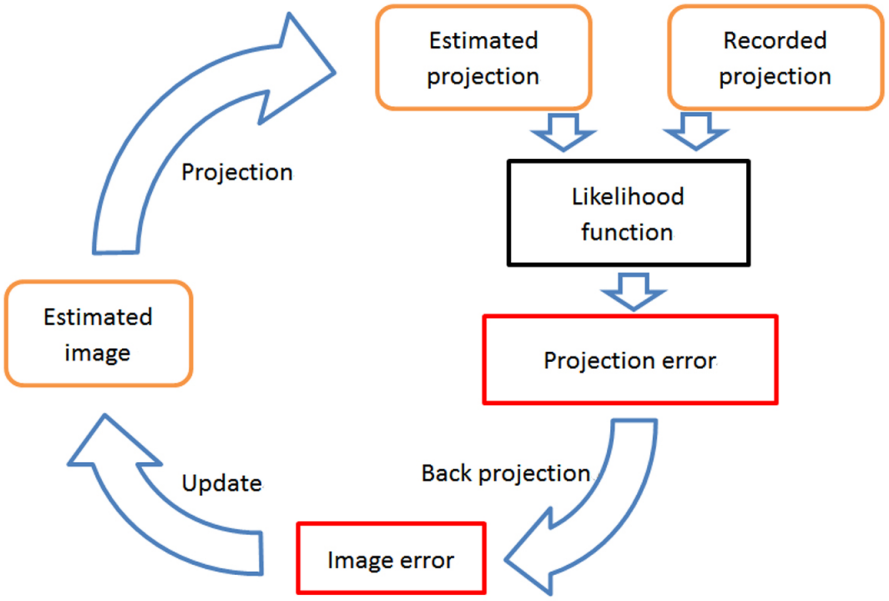

Figure 2.4: Flowchart of iterative MLEM image reconstruction algorithms

$$x = A^{-1}p$$

However, directly solving the inverse matrix of A_{ij} is computationally prohibitive due to its size. Iterative OSEM methods are most commonly used to solve this problem (Figure 2.4). In OSEM algorithms, projections from an initial estimate of SPECT image can be calculated using the system matrix. The projection space error between estimated and recorded projection is in turn back-projected to the image space. Accurate SPECT image can be reconstructed from iteratively updating the estimated SPECT image from the image space error in previous iteration [49]. In OSEM algorithms, the projection data is also grouped into several mutually exclusive subsets. Projection and updating of estimated image are performed on each subset sequentially in every iteration. Thus the image error converges at a much faster rate which greatly accelerates the process of image reconstruction .

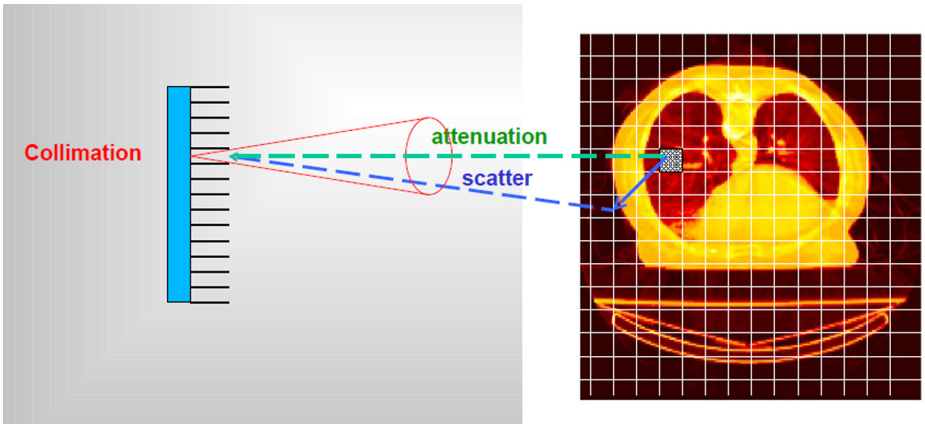

Figure 2.5: Attenuation, scatter and collimator blurring in SPECT image reconstruction (image courtesy of Dr. Sergey Shcherbinin)

2.2.2 Quantitative Correction in SPECT Image Reconstruction

As aforementioned, the system matrix A_{ij} models the physical process of data acquistion. It also provides the unique advantage allowing user to incorporate the physical performance of the imaging system and γ ray transport into the image reconstruction. This includes the correction for collimator blurring, attenuation and scatter of γ rays. The resolution of the collimator depends on the distance from it, meanwhile γ rays can be scattered away from their original paths or absorbed due to attenuation (Figure 2.5).

If not correctly accounted for, these effects all have a negative impact on the accuracy of the reconstructed SPECT image. The following experiment carried out by our collaborators at the Medical Imaging Research Group (MIRG) at UBC demonstrated the importance of quantitative corrections in SPECT image reconstruction (Figure 2.6).

In this example, two identical tubes containing ^{99m}Tc with same activity were placed at different positions within a water filled lung phantom. Considerable difference in the intensity and shape of the two identical sources can be seen in images not accounting for attenuation and scatter. After attenuation, scatter and collimator blurring are incorporated into the reconstruction, the difference is much smaller. Although not a standard practice in lung SPECT imaging, attenuation can be easily

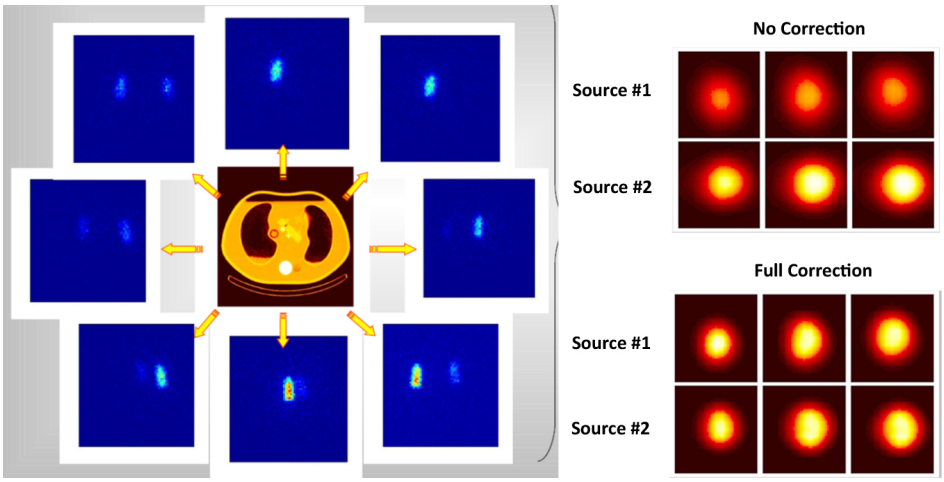

Figure 2.6: Projections taken from the experiment (left) and transversal view of ^{99m}Tc sources in different reconstructions (right) (image courtesy of Dr. Sergey Shcherbinin)

corrected using a hybrid SPECT-CT scanner. Corrections for scatter and collimator blurring require more sophisticated modeling of the physical process of imaging. The detailed approaches and methods for these quantitative corrections are beyond the scope of this thesis. Their impact on SPECT guided treatment planning will be explicitly discussed in the next section.

2.3 The Impact of Reconstruction on Treatment Planning

2.3.1 Motivation

The use of SPECT to evaluate lung function for the purpose of optimizing beam angles was first proposed by Marks et al.[41]. Several investigators have incorporated SPECT data into RT treatment planning optimization (Seppenwoolde et al.[42], McGuire et al.[45], Lavrenkov et al.[46, 47], Shioyama et al.[44], Christian et al. [50]). Generally two approaches: SPECT weighted mean dose (SWMD) and functional lung volume segmentation have been proposed previously.

Optimizing treatment plans based on SWMD was first demonstrated by Sep-

penwoolde et al.[42], where the beam angles and fluences were optimized to minimize the SWMD without compromising target dose coverage. The other approach, functional volume (fV) segmentation, was more widely used (Lavrenkov et al.[46, 47]), because it can be readily utilized in commercial treatment planning systems (TPS). In this approach, a new organ at risk, functional lung ($fV_{x\%}$, the volume of lung which exhibits more than x% of the maximum SPECT intensity, the maximum being defined as a maximum voxel uptake), is segmented by applying a pre-set threshold to SPECT perfusion map. All voxels exhibiting SPECT perfusion above this threshold are designated as belonging to functional lung. Treatment planning is then performed by applying dose-volume constraints, e.g., V_{20Gy}, to this functional, rather than full normal lung [46, 47].

The quantification of SPECT images is sensitive to the kind of reconstruction methods. Given the growing interest in using SPECT-based optimization, it is reasonable to question the impact of these technical factors on the resultant SPECT images and consequently the SPECT guided treatment planning. Our preliminary studies [51, 52] suggested that these technical factors can have meaningful effects on the reconstructed SPECT images. Specifically, for a representative plan, the function weighted dose to 50% of lung volume exhibiting the strongest SPECT intensity was 6.9 Gy when no corrections were applied and 7.6 Gy with all corrections applied (Thompson et al.[52]).

In this study we aim to systematically evaluate the impact of the method of SPECT reconstruction on mapping lung perfusion and on SPECT-guided treatment planning. The two methods of incorporating SPECT into planning which are based on SWMD (Seppenwoolde et al.[42]) or functional lung segmentation (Lavrenkov et al. [46, 47]) were investigated based on previous clinical experience and predictors of radiation pneumonitis. Advocates of these methods have not considered the impact of SPECT reconstruction, which is often simply defined by the available hardware and vendor-provided reconstruction software. In this study we only address the sensitivity of SWMD and fV segmentation to SPECT reconstruction correction methods, as they guide RT planning. Merits of SWMD and fV based metrics as they apply to predicting lung complications are not assessed. Ideally the method of choice should be transferable from clinic to clinic without overly stringent requirements for consistent methods of SPECT reconstruction.

2.3.2 Methods

The present analysis is based on the pre-RT SPECT/CT acquistions of 9 patients enrolled in this study, eight with inoperable non-small (NSCLC) and one with limited stage small cell lung cancer (SCLC). The procedures of SPECT scans and CT simulations were carried out as described in Chapter 1.

Image Reconstruction

For each patient, the data acquired during SPECT/CT scan was used to generate four different SPECT image sets using four different image reconstruction methods. These different scenarios were chosen to assess the impact of different attenuation and scatter correction techniques. In all reconstructions the same reconstruction matrix (128 x 128 x 128) and same voxel size (4.4 x 4.4 x 4.4 mm^3) were used. All of the datasets were reconstructed using the ordered subsets expectation maximization (OSEM) algorithm with the same 10 subsets and twelve iterations. The reconstructed images were filtered with a 3D Gaussian filter (3×3 pixel kernel).

CAM (Camera reconstruction): SPECT images were reconstructed using the OSEM algorithm with an advanced version of the vendor's software (Evolution-for-Bone^{TM}, GE HealthCare) which included 3D resolution recovery (RR) and attenuation correction (AC) based on the narrow-beam attenuation map from the low dose Hawkeye CT scan (a narrow-beam attenuation coefficient corresponds to pure photon absorption and does not account for scattered photons). An order 10 Butterworth filter with the cutoff equal to 0.48 of the Nyquist frequency was used in these reconstructions. Since this set of images was reconstructed using vendor software that is used in the clinic, it was selected as a reference set when comparing reconstructions, and addressing their impact on clinical treatment planning.

OSEM-BB: In this reconstruction method, in addition to resolution recovery, attenuation correction (AC) using a CT-based attenuation map with μ-coefficients corresponding to the broad-beam (BB) values was implemented. The BB attenuation map, which was obtained by scaling the narrow-beam attenuation map by a factor of 0.8, allowed indirect accounting for scattered photons. This approach

Table 2.2: Hierarchy of SPECT reconstruction methods. All reconstructions used iterative OSEM algorithm and included resolution recovery correction (RR).

	Method 1 (CAM)	Method 2 (OSEM-BB)	Method 3 (OSEM-APD)	Method 4 (OSEM-NOC)
Attenuation Correction (AC)	included	included	included	none
Scatter Correction (AC)	none	Indirect, using broad-beam attenuation coefficient	direct scatter modeling (APD method) incorporated into reconstruction	none

effectively removes scattered photons from the image, but does no correct for their spatial distribution. The OSEM-BB method was included in our analysis as it is very simple and easy to implement, and to the best of our knowledge, closely resembles the method used by the commercial GE software (Method 1).

OSEM-APD: This algorithm incorporated resolution recovery (RR) as well as corrections for attenuation and scatter (SC). In this case, AC was done using a CT-based narrow-beam attenuation map and SC was done using an advanced approach which is based on the analytical photon distribution (APD) method [53]. It is believed to be the "best" algorithm since it exactly models scatter distribution using patient specific attenuation maps and the physics of photon interaction with matters, using Klein-Nishina formulae [54].

OSEM-NOC: In this method, only RR correction was included in the reconstruction.

The summary of quantitative corrections that were included in the reconstruction is presented in Table 2.2.

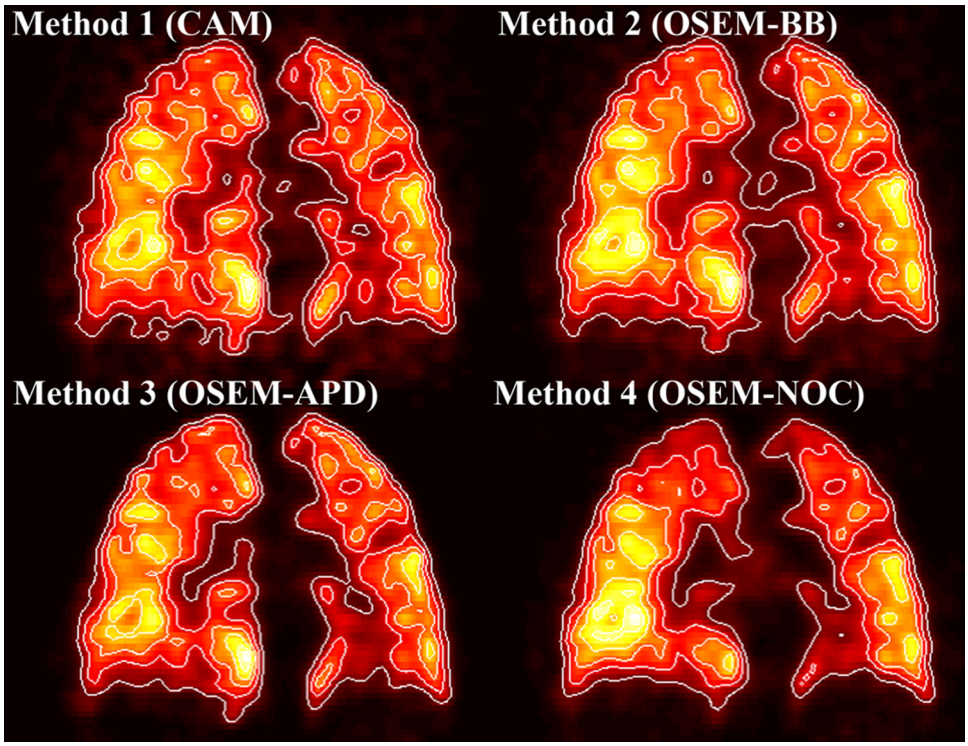

Figure 2.7: Coronal image for four SPECT reconstruction methods. White lines represent iso-contours of the 20,40, 60, 80% of maximum SPECT uptake respectively. All images are scaled to their individual maxima.

Figure 2.7 shows coronal slices of a lung perfusion SPECT scan obtained from each of these four reconstructions.

Image Registration

The low resolution CT scans obtained from the SPECT-CT scanner and the planning CT were registered based on reference points placed by radiation oncologists on the patients to mark selected anatomical and physiological landmarks. For registration, the low resolution CT was deformed and rotated to minimize the distance between pairs of landmarks in the two CT sets. Subsequently, the SPECT image was also deformed and rotated in the same way as the low resolution CT, in order to be co-registered it to the planning CT image.

Because the planning CT was linked with the 3D dose distribution, and the low-dose SPECT-CT was linked with the SPECT data, this CT-CT registration provided the transformation matrix to link the SPECT and 3D dose data.

Analysis Methods

Planning CT images were segmented using Eclipse treatment planning software (Varian, Palo Alto) to define the lung (by a radiation therapist), and gross tumor volume (GTV; by a treating physician). A "normal lung" volume was defined as the whole lung volume minus GTV. Only the SPECT counts within this "normal lung" volume were used in the analysis relating SPECT counts to radiation doses. The planning target volume (PTV) was created by expanding the GTV by 1.5 cm in the anterior, posterior and lateral directions and by 2.0 cm in the superior and inferior directions.

Comparison of fV segmentations For each patient, the lung was segmented into functional volumes, ($fV_{x\%}$), by applying a threshold x=10, 20, $\cdots$, 90% of maximum SPECT intensity. The combined volume $fV_{x\%}$, comprising all voxels exhibiting SPECT signal above the threshold x% was defined as the functional volume corresponding to the given method of SPECT reconstruction. The procedure was performed for all four SPECT reconstructions.

The spatial agreement in $fV_{x\%}$ between the first and each of the remaining three reconstruction methods was then calculated as the ratio of the shared $fV_{x\%}$ volumes over the total volume of $fV_{x\%}$ in these two reconstructions:

$$fVR^{i}_{x\%} = \frac{fV^{i}_{x\%} \cap fV^{1}_{x\%}}{fV^{i}_{x\%} \cup fV^{1}_{x\%}}, i = 2,3,4; x = 10,20,\cdots,90$$

As mentioned, the images reconstructed using the vendor's software (CAM) served as a reference here. A perfect agreement between $fV_{x\%}$ would make $fVR^{i}_{x\%}$ equal to one, whereas a smaller $fVR^{i}_{x\%}$ would mean less agreement between $fV_{x\%}$ in each reconstruction. Additionally, the volumes of $fV_{x\%}$ for each reconstructed image, and differences between these volumes were also calculated and reported.

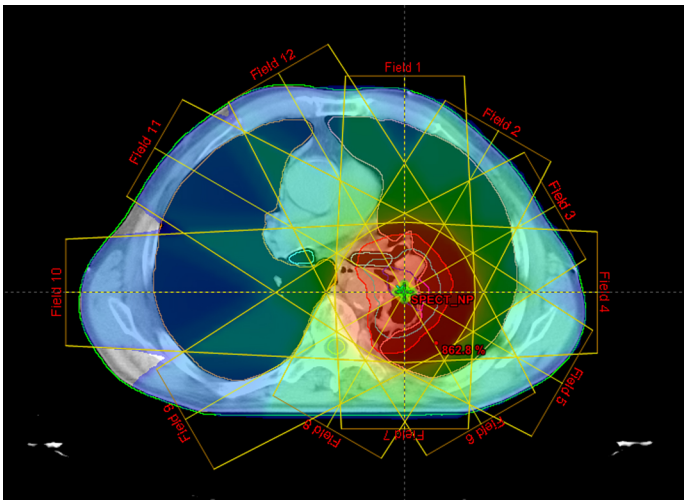

Figure 2.8: An example of the setup of the twelve radiation fields.

Comparison of SPECT Weighted Mean Dose (SWMD) calculations

Setup of treatment plans To systematically study the effect of SPECT reconstruction on SWMD, a variety of field sizes for twelve equally spaced gantry angles were tested. The rationale for this was that if SPECT reconstruction affects SWMD for a variety of field sizes and gantry angles in a systematic fashion, the observed trends would apply to any specific RT plan. The isocenter was placed on the PTV center of mass (Figure 2.8). The field sizes were 5cm x 5cm, 7.5cm x 7.5cm and 10cm x 10cm for each gantry angle. Each field delivered 6000 MU, thus the mean lung dose from each field is comparable to those in clinically used plans with a prescription dose of 60 Gy.

Calculation of SWMD and SWMD dependence on SPECT reconstruction In order to quantify the differences between the SWMD from different reconstruction methods, the SPECT weighted mean dose was computed for each image set. The dose distribution from each field and SPECT reconstruction were exported to Matlab (MathWorks, Inc) for calculation and analysis. From the *i*th SPECT reconstruction and dose distribution from the field at gantry angle *j*, SWMD can be

calculated as:

$$SWMD_i^j = \frac{\sum_k S_k^i \times D_k^j}{\sum_k S_k^i}, j = 0^\circ, 30^\circ, 60^\circ, \cdots, 330^\circ$$

where S_k^i and D_k^j are the number of counts in the kth voxel in the above mentioned "normal lung volume" in the SPECT image from ith reconstruction method and dose to the kth voxel from the field at gantry angle j, respectively. Since 3 field sizes were considered for each gantry angle for 9 patients, for each combination of the reconstruction method i and gantry angle j, twenty seven sets of $SWMD_i^j$ were available. For each of the patients, there were 144 calculated SWMDs available for further analysis, i.e., 4 methods of SPECT reconstruction times 12 gantry angles times 3 field sizes.

In order to compare the impact of different reconstruction methods on SWMD, the "Difference" figure of merit was created. It was defined as the ratio of the difference of $SWMD_i^j$ obtained from the investigated reconstruction method (method i) and the $SWMD_1^j$ obtained from the reference method (CAM), both at a given gantry angle j. This difference ($Diff_i^j$) was calculated as:

$$Diff_i^j = \frac{SWMD_i^j - SWMD_1^j}{SWMD_1^j}, j = 0^\circ, 30^\circ, 60^\circ, \cdots, 330^\circ; i = 2, 3, 4$$

The minimum and maximum results of the $Diff_i^j$ for each group of i and j were reported. In order to avoid canceling out of positive and negative $Diff_i^j$s, $\left|Diff_i^j\right|$ was used to calculate averaged differences.

For the comparison of SPECT weighted mean dose and functional volumes, the SPECT image sets from the four reconstruction methods were used (CAM to OSEM-NOC with 12 iterations applied in the image reconstruction). Thus in total, for each patient there were 108 values of $Diff_i^j$(three plans with 12 radiation fields and three reconstruction methods other than the reference method) and 27 values of $fVR_{x\%}^i$ (x = 10, 20, 30, $\cdots$, 90 respectively in the three alternate reconstruction methods).

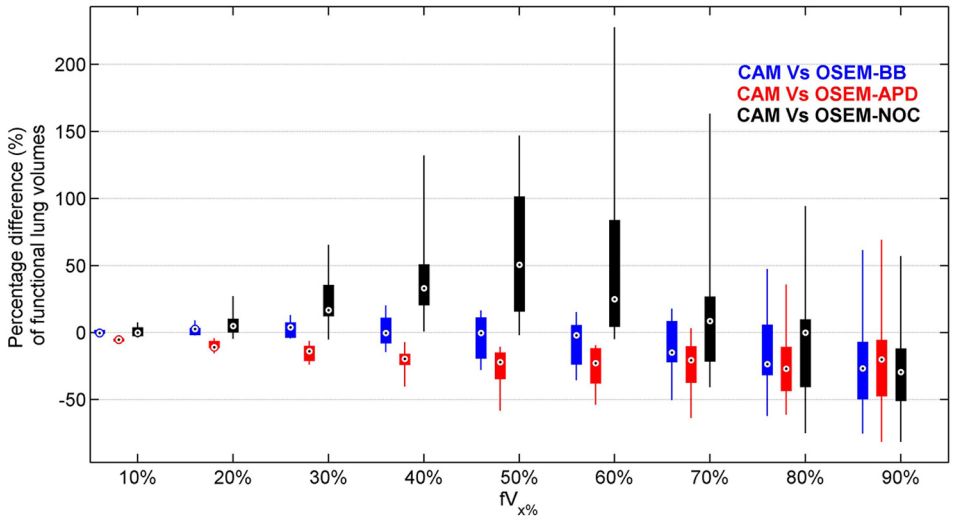

Figure 2.9: Percentage difference of the volumes of the functional lung defined by segmentation of each reconstruction. SPECT intensity threshold, plotted on the horizontal axis is a proportion of the maximum intensity in percent. The box and whisker plot shows lower quartile, median, upper quartile values (box) and maximum and minimum values (whisker).

2.3.3 Results

Functional Volume Segmentation

The difference in the volumes of segmented functional lung in each reconstructed image as a function of the threshold used in the segmentation is plotted in Figure 2.9

Compared to reference images (CAM), OSEM reconstructions with attenuation and scatter correction provided lower volumes of functional lung for most of the patients. This is a result of more accurate correction for scatter which removed image blur due to scattered photons, especially for high perfusion regions (Figure 2.9). When using 40-60% of the maximum SPECT uptake as a threshold in functional lung segmentation, the differences of absolute volume were on the order of $\sim$25%. Meanwhile on average, the OSEM reconstructions without corrections considerably overestimated the functional lung volume considerably at $fV_{40-60\%}$.

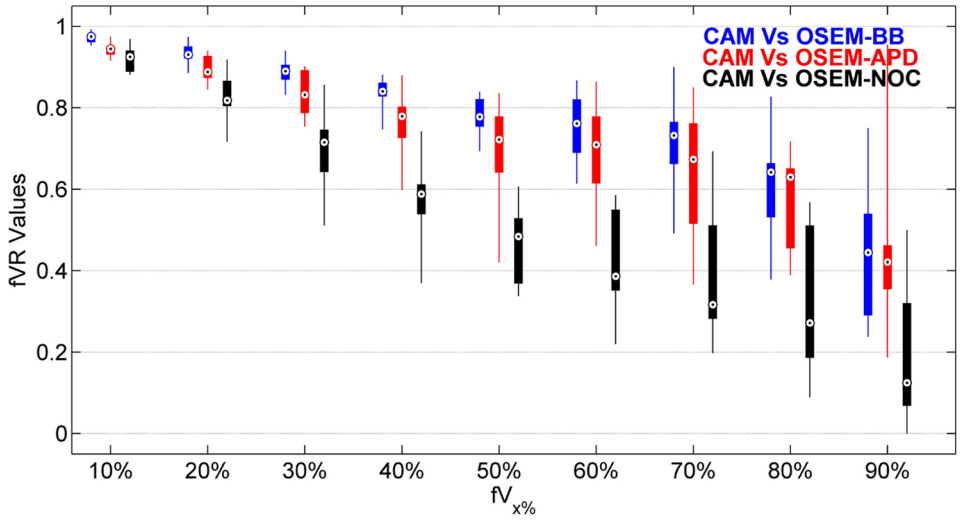

Figure 2.10: The agreement between functional volumes (represented as the fVR value) from each reconstruction method as a function of threshold used in the segmentation. SPECT intensity threshold, plotted on the horizontal axis is a proportion of the maximum intensity in percent. The meaning of box and whisker plots is the same as in Figure 2.9

The differences varied by more than 100% in some cases.

As noted in the previous section, the degree of spatial agreement between segmented functional volumes (denoted as fVR) in different reconstructions can be calculated. The analysis of spatial agreements of functional lung volumes for images reconstructed using methods 2-4, relative to those reconstructed with CAM, as a function of the threshold used in the segmentation, is shown in Figure 2.10. Substantial variations in functional volumes were seen throughout the continuum of thresholds, including the 40-60% region which has been suggested to be the ”most clinically relevant” by others (Lavenkov[47]). The degree of agreement between segmented images obtained from different reconstructions, i.e. fVR, decreases at higher thresholds; i.e., the consistency between segmented high perfusion regions is less than for regions inclusive of low perfusion. This is somewhat expected because larger thresholds mean smaller functional volumes and smaller volumes would be prone to larger relative variation.

Table 2.3: Relative absolute difference $\left|Diff_i^j\right|$ (%) in SWMD as compared to CAM reconstructions. Attenuation and scatter corrections used in each method are specified in Table 2.2

	OSEM-BB			OSEM-APD			OSEM-NOC		
Field size (cm × cm)	5 × 5	7.5 × 7.5	10 × 10	5 × 5	7.5 × 7.5	10 × 10	5 × 5	7.5 × 7.5	10 × 10
Min	0	0	0	0	0	0	0	0	0
Mean	1.56	2.0	1.33	1.67	2.83	0.71	7.95	7.11	6.29
Max	7.53	6.55	4.20	10.9	12.5	2.66	27.1	26.7	19.5
Overall Mean		1.63			1.74			7.12	

Calculation of SPECT Weighted Mean Dose (SWMD)

The statistics for absolute values of $Diff_i^j$ are presented in Table 2.3. The mean, the maximum and minimum of $\left|Diff_i^j\right|$ were calculated for all the patients and gantry angles at each field size. Additionally, the overall mean, averaged over all three plans with different field sizes is also provided.

For SPECT images reconstructed with only resolution recovery (RR) correction (no AC and SC) (OSEM-NOC), the calculated overall mean value of $\left|Diff_i^j\right|$ is approximately 7%; maximum difference reaches 27%.

There were smaller differences in SWMD between methods 1, 2 and 3, i.e., when attenuation correction was incorporated into the SPECT reconstruction algorithm. Overall mean of $\left|Diff_i^j\right|$ were 1.63% and 1.74% for OSEM-BB and OSEM-APD reconstructions respectively, with a maximum difference of less than 13% (Table 2.3).

The angular dependence of relative differences $Diff_i^j$ is shown in Figure 2.11. The results from statistical analysis are also shown in Table 2.4. In the current protocol used in our cancer centre, when lung cancer patients are treated with 3 field conformal RT, beam angles of 0, 70, 140 degrees or 0, 290, 220 degrees are used. Thus we chose 0,60,150 degrees and 0, 210, 300 degrees (for left and right

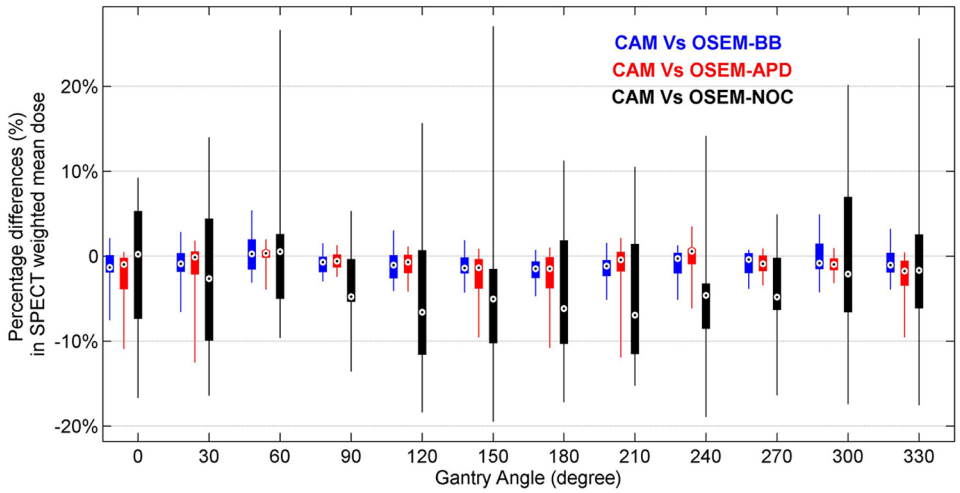

Figure 2.11: The difference in SWMDs as a function of gantry angle. The meaning of box and whisker plots is the same as in Figure 2.9

sited tumors respectively) which are the closest gantry angles used here as clinically relevant beam angles in the following analysis. The SWMD values obtained from reconstruction without attenuation correction and scatter correction (OSEM-NOC) consistently demonstrated large variations from CAM (standard deviation $\sim$8%), over all gantry angles, as compared to OSEM-BB and OSEM-APD methods (standard deviation $\sim$2%). When approximate (OSEM-BB) or more accurate (OSEM-APD) attenuation and scatter corrections were included in the reconstructions, the differences from CAM reconstructions in SWMD values are relatively smaller ($\sim$2%). This is consistent with those calculated from clinically relevant beam angles.

Number of iterations in the image reconstruction

The number of iterations used in the image reconstruction might also affect our results. Our previous studies[52] demonstrated that, from the same scan, the size of functional volumes will decrease and converge to a constant value with increasing number of iterations. Meanwhile, the point where the volume will converge varies between patients. We chose to use twelve iterations to reduce this potentially con-

Table 2.4: Angular dependence of $Diff_i^j$ (%) in SWMD as compared to CAM reconstructions

	OSEM-BB	OSEM-APD	OSEM-NOC
Median $Diff_i^j$ over all gantry angles (%)	-1.05	-0.67	-4.28
Standard deviation $Diff_i^j$ over all gantry angles (%)	1.84	2.43	8.39
Median $Diff_i^j$ at clinical relevant gantry angles (%)	-1.05	-0.68	-3.34
Standard $Diff_i^j$ at clinical relevant gantry angles (%)	2.05	2.50	9.14

founding factor in our analysis. However, the number of iterations varies between clinics due to different settings in vendor's software and clinical protocols which could potentially affect the results of functional volume segmentation and SWMD calculation. Thus, we also compared the size of functional lung volumes using reconstruction method 1, with 4 and 12 iterations respectively. A sample set of data from Patient 1's scan is presented in Table 2.5 showing a large difference ($>$30%) in the volumes. In contrast, the SWMDs calculated in reconstructions using different number of iterations were very close (difference$<$1%). The data from Patient 1's scan is presented in Table 2.6.

2.3.4 Discussion

In this study, the impact of SPECT reconstruction with attenuation, scatter and resolution recovery corrections on SPECT guided radiotherapy planning was quantified. Iterative reconstruction algorithms, such as ordered subsets expectation maximization (OSEM) allow the user to incorporate sophisticated corrections into the reconstruction process, resulting in quantitatively accurate and less noisy images.

Table 2.5: The volume (cm^3) of $fV_{40-60\%}$ in the reconstruction performed using vendor's software with different number of iterations

	$fV_{40\%}$	$fV_{50\%}$	$fV_{60\%}$
Method 1, 4 iterations	1174.38	657.38	324.38
Method 1, 12 iterations	815.25	388.13	155.63
Percentage difference(compared to Method 1, 12 iterations)	30.6%	69.4%	108.4%

Table 2.6: SPECT weighted mean dose (cGy) in reconstructions using vendors software with different number of iterations

Field Size	5cm × 5cm	7.5cm × 7.5cm	10cm × 10cm	5cm × 5cm	7.5cm × 7.5cm	10cm × 10cm
Gantry Angle (degree)	90	180	90	180	90	180
Method 1, 4 iterations	319.40	60.06	720.95	143.61	1286.99	273.70
Method 1, 12 iterations	320.97	59.97	722.41	143.38	1286.59	272.75
Percentage difference	0.5%	0.1%	0.2%	0.2%	0.0%	0.3%

In parallel, increased availability of hybrid SPECT/CT systems and the growing popularity of iterative reconstruction techniques, which are gradually replacing filtered backprojection (FBP) in clinical nuclear medicine studies, calls for a systematic investigation of their effect on functional lung guided RT.

Information about lung function obtained from the SPECT studies depends on the reconstruction algorithm, and whether or not this algorithm includes corrections for resolution loss, photon attenuation and scatter in the body. It is reasonable to question the impact of these technical factors on the resultant SPECT images and consequently the SPECT guided treatment planning. Such an analysis is needed to ensure consistency for inter-institutional clinical trials of SPECT guided RT. However, the issue of SPECT reconstruction has not been extensively addressed in previous SPECT guided RT studies. In some papers, the reconstruction technique was not even mentioned [42, 45], and some used simple FBP with Chang attenuation correction (AC)[46, 47, 50]. Since Chang AC assumes uniform tissue density, which is clearly not the case in the lung region, the method was slightly modified to work in non-homogeneous cases. Only Shioyama et al. [44] employed an iterative reconstruction which included CT-based patient-specific attenuation correction, however the parameters used in the reconstruction weren't specified.

Due to the limitation of current commercial TPS, most current SPECT guided RT studies rely on functional lung segmentation. Sub-volumes are treated as new "organs" and given different constraints and priorities based on their functionality. When using this approach, accurate $fV_{x\%}$ segmentation is crucial for accurate treatment planning. However, in the iterative OSEM SPECT reconstructions, several factors including attenuation and scatter correction, number of iterations and other filters used post-reconstruction, all contribute to the resolution and accuracy of SPECT images, and therefore the accuracy of functional lung volume segmentations (Figure 2.12).

In our study, the images reconstructed by the vendor's software (CAM) which is generally available for clinical use, served as a standard in the analysis. This method uses the OSEM algorithm with AC and RR in the image reconstruction. When reconstructions with different sets of corrections were compared to this reconstruction, large variations were observed in the segmented functional lung volumes. More than a 50% difference in $fV_{40-60\%}$ was observed between reconstruc-

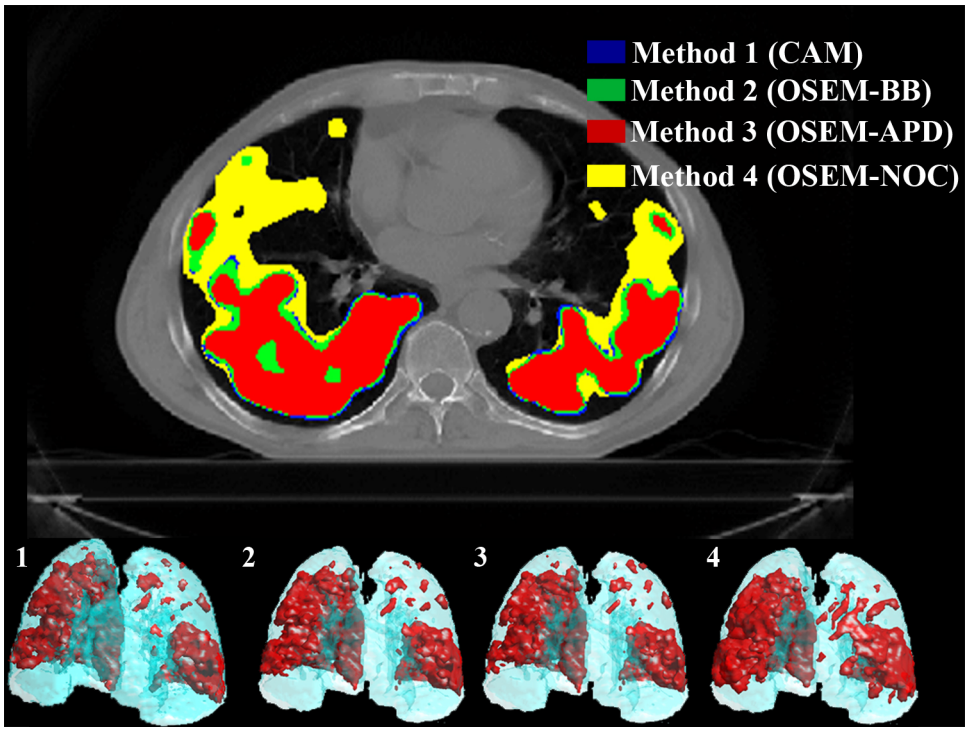

Figure 2.12: SPECT and CT scans of Patient 2. Top: Transverse view of $fV_{40\%}$ in the four SPECT reconstructions overlaid on the planning CT images. Bottom: Volume rendering of lung (cyan) and $fV_{40\%}$ (red) in the four SPECT reconstructions (From left to right: CAM to OSEM-NOC method)

tions with and without attenuation and scatter correction applied.

The impact of this difference on the results of current studies of SPECT guided RT for lung cancer patients may be clinically meaningful. The functional lung volume segmentation approach is sensitive to several image reconstruction related factors such as attenuation correction and scatter correction. This variation of functional volumes is more severe at high perfusion levels which are the target of dose sparing in SPECT guided RT. As a result, using generalized threshold values will create variation in both the functional lung volumes and the V_{20Gy} in each functional volume between each reconstruction (Table 2.7). This implies that functional lung segmentation might not be a robust approach to SPECT guided RT.

Table 2.7: Volumes (cm^3) of $fV_{40,50\%}$ and V_{20Gy} in each $fV_{x\%}$ (Patient #2).*

	V_{20Gy} in $fV_{40\%}$	$fV_{40\%}$	V_{20Gy} in $fV_{50\%}$	$fV_{50\%}$
CAM	160.63	1104.63	73.25	485.38
OSEM-BB	164.13	1102.25	71.5	483.88
OSEM-APD	132.38	872.88	55.88	343.75
OSEM-NOC	211.63	1511.8	100.13	781.50

Dose volume constraints on each functional lung subvolume in one clinic may not be transferable to other institutions as the segmentation of functional volume itself is sensitive to characteristics of the image reconstruction algorithm.

Conversely, the SWMD appears to be less effected by the type of SPECT reconstruction. The largest differences in SWMD were found with comparing CAM (clinical reference image) to OSEM-NOC (reconstructions without any attenuation and scatter correction), where the average difference was $>7\%$ (Table 2.3). When CT-based AC was used, differences between CAM reconstructions and the other two SPECT reconstruction methods (OSEM-BB and OSEM-APD) were smaller, overall differences $\leq 2\%$. Both of these values are less than the $\sim 25\%$ differences seen in the functional volume segmentation. Thus, compared to the functional lung volume segmentation, SWMD calculations are less sensitive to the type of reconstruction, providing that the accurate AC (based on the non-homogenous attenuation map) is employed.

2.3.5 Conclusion

The impact of different SPECT image reconstruction and attenuation/scatter correction methods on quantitative SPECT guided radiation therapy treatment planning was investigated. Four sets of perfusion SPECT images were reconstructed using different scatter/attenuation correction methods for nine lung cancer patients. SPECT weighted mean dose was calculated for twelve equally spaced radiation beams and functional lung volumes were segmented using thresholds defined as percentage of the maximum SPECT uptake values. When reconstructions with different attenuation/scatter were compared to reference images reconstructed us-

ing vendor software, a large variation in functional lung volumes and V_{20Gy} of them was observed. Nevertheless the SPECT weighted mean doses calculated from all reconstructions with accurate CT based attenuation correction were generally consistent regardless of the types of scatter corrections. In conclusion, when using SPECT perfusion imaging during treatment planning optimization/evaluation, the SWMD (SPECT-weighted mean dose) may be the preferred figure of merit as it is less affected by reconstruction technique, compared to the threshold-based functional lung volume segmentation.

Chapter 3

Implementation and Evaluation of Image Registration Methods in SPECT Guided Radiotherapy

Within the scope of SPECT guided treatment planning, three different sets of images or data need to be co-registered to each other, i.e. planning CT images, perfusion SPECT images and dose distributions should share the same reference system. Using the CT simulator and in-room laser setup systems as introduced in Chapter 1, dose distribution and planning CT image are inherently co-registered to each other in routine RT treatment planning. Meanwhile perfusion SPECT images can be co-registered to planning CT images directly using external radioactive markers or indirectly with the help of a hybrid SPECT-CT camera.

The hybrid SPECT-CT camera is becoming widely used in nuclear medicine departments. In this system, a CT scanner is mounted aside the SPECT camera, thus a CT scan can be carried out immediately after the SPECT scan while the patient is still on the couch. The CT image provides anatomical information in addition to the functional information from the SPECT image. It is also being used to correct for photon attenuation during SPECT image reconstruction, as described in Chapter 2. In our study, this set of CT images is co-registered to the planning CT images, thus in-directly co-registering the perfusion SPECT images with planning CT images.

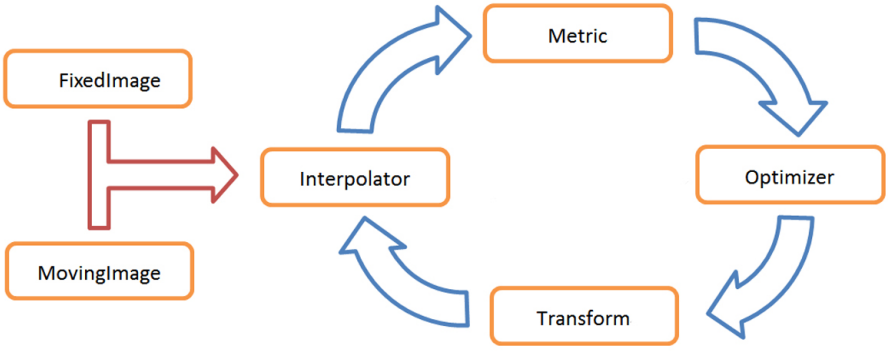

Figure 3.1: The framework of image registration as implemented in ITK

3.1 Image Registration Framework

Generally, a 2D or 3D image can be viewed as a grid of points with scalar or vector values associated to each point. A spatial transform is a point to point correspondence between two images. The process of image registration is to find the best spatial transform which maps the objects from one image to the homologous objects on the other image.

The ITK (Insight Segmentation and Registration Toolkit, Kitware Inc.) is a popular open source code package for image registration purpose. In ITK, image registration can be carried out within its framework with four types of components (*Transform*, *Optimizer*, *Interpolator* and *Metric*) and two inputs (*Fixed Image*, *Moving Image*). The *Transform* component defines the spatial mapping between grid points in two images. Within this framework, image registration is solved as an optimization problem with the goal of finding the best parameters of *Transform* component that bring the *Moving Image* into alignment with the *Fixed Image* (Figure 3.1).

During the optimization, either the *Fixed Image* or transformed *Moving Image* can be resampled by the *Interpolator* to match their voxel sizes and number of voxels in each dimension. The resampled images are fed into the *Metric* component which is used to measure how well two images are matched. This measure serves as a reference for the *Optimizer* to search the solution space of *Transform* parameters to solve the image registration problem. The final output from the framework is a

transformed *Moving Image* which is co-registered to *Fixed Image*.

3.2 Motivation

Using SPECT in RT treatment planning requires careful registration of functional SPECT images with anatomical CT images that are used for therapy planning. When SPECT images are acquired using a hybrid SPECT/CT camera this registration is relatively easier than it is in situation when only SPECT data are available, as it can employ CT-to-CT registration. In this case the CT set acquired from a hybrid SPECT/CT scan, is first registered to the planning CT. The transformation and warping obtained from this registration is then applied to the SPECT image so that it too is registered to the planning CT. Several methods of registering images exist. Previously reported clinical studies used landmark-based registration [46, 47, 50] using either fiducial markers placed physically on the skin, or using anatomical and physiological landmarks that have been identified manually as corresponding pairs in both CT images. Automated non-rigid registration methods resolve a displacement field such that when it is applied to one image, this image becomes aligned with the target second image. Non-rigid methods often involve a set of parameters that control the amount of regularization being enforced on the displacement field; these will affect the resulting spatial transformation or the corresponding displacement vector field.

In this study we report on the use of six registration methods to register CT images for the purpose of aligning the corresponding SPECT images to the planning CT. The methods used vary in their complexity from the simplest rigid co-registration, to 3-D affine transform based on control points placed on the skin or lung landmarks, to non-rigid registration using a B-spline transformation, or diffeomorphic demons and level set non-rigid registration. We performed initial experiments to empirically determine the values for these parameters that would allow us to successfully register our image sets, but would not restrict the transformation excessively. We also evaluated the quality of co-registration using various validation metrics.

3.3 Methods

Institutional ethics approval was acquired prior to recruiting patients. Ten patients (6 Males aged: 50±10yrs, 4 females 40±10yrs) recently diagnosed with lung cancer and referred for radiation therapy consented to have a perfusion SPECT scan for the purpose of this study. Nine of these patients were diagnosed with non-small cell lung cancer (NSCLC) and one with small cell lung cancer (SCLC).

Detailed procedures and imaging parameters of perfusion SPECT scan has been presented in section 1.6. Treatment planning and dose calculations were performed on the planning CT set. Thus, it was selected as the *fixed CT image* in the image registration. The low resolution CT image acquired during the SPECT scan was labled as *moving CT image* and registered to the *fixed CT image* through various image registration algorithms employed in this study. The original SPECT image was subsequently registered to the planning CT (*fixed CT image*) as a result of the CT-CT registration.

3.3.1 Image Co-registration Methods

Skin Control Point Based Registration ('Skin Method')

In this method, a set of 8-12 control points on the skin contour was selected on the *moving CT Image* and *fixed CT Image* respectively. These control points were used simulate the radioactive fiducial markers which were previously used to register SPECT images from a stand-alone SPECT scanner with no CT capability [46, 47, 50]. A 3-D affine transform is used to minimizes the distance between the corresponding control points in a least-square sense.

Lung Control Point Based Registration ("Lung Method")

This method employs the same approach to find image transformation as the 'Skin Method'. But here, instead of selecting control points on the radio-opaque markers, these were manually located within the lung in the *moving CT Image* and *fixed CT Image*.

Rigid Registration ("Rigid")

The *fixed CT image* and *moving CT image* were transformed rigidly to minimize the negative value of the mutual information (MI) metric between the two images[55]. A regular step gradient descent optimizer was used to drive the optimization with maximum step length 0.15, minimum setp length 5×10^{-6} and 200 iterations.

B-Spline Non-Rigid Registration ("B-Spline")

We employed a gradient-descent based optimizer to resolve the parameters of a B-spline transform that minimizes the negative value of the MI metric as in Rigid Registration. The combined use of B-Spline regularization, and MI was found to be suitable for CT lung registration by De Craene et al.[56]. Two levels of registration were used with the first and second levels using 15 and 34 nodes on the B-spline grid respectively.

Diffeomorphic Demons Non-Rigid Registration ("Demons")

This is an optical-flow-like technique which has been applied to lung CT registration by Wang et al.[57]. We used the diffeomorphic version of this technique as done by Vercauteren et al.[58], which ensures that the computed transformation has a differentiable inverse so that the topology of anatomical structures is preserved after registration. Two levels of registration were used with 25 iterations in each level. Maximum update step length was set to 2.

Level Set Non-Rigid Registration ("Level Set")

This method is in essence a more-efficient and computationally faster version of the Demons method, wherein a level-set model is used to model deformations[59]. Two levels of registration were used with 25 iterations in each level. The deformation field was smoothed with a smoothing kernel (standard deviation set to 2) during the iterations.

3.3.2 Evaluations Methods

The results for CT-CT registration can be evaluated qualitatively or quantitatively using different figures of merit. The success of registration for our purposes also

requires that the deformation field, when applied to the SPECT images, creates valid images. The warped SPECT images should be clinically realistic, i.e. indicates the same normal or reduced perfusion region as seen in the original scans, as well as acceptable for use in therapy planning. For non-rigid registration, if the regularization on the displacement field is insufficient, the algorithm might twist the deformation field to over-correct for the images differences due to noise or intra-scan motion, thus causing folding and discontinuities in the generated displacement field (e.g. displacement vectors of two adjacent voxels may cross over each other). When applied to SPECT images , it would yield false or implausible activity distributions.

A common quantitative assessment of image registration is to calculate the Target Registration Error (TRE) using two sets of corresponding landmarks identified in the registered images by clinical experts[60]. This approach is not suitable for lung images, however, as reproducible identification of landmarks in lung is difficult. A variety of automatic image registration metrics[57, 59, 61] can be calculated from a registered image pairs; these include: RMS_{int} - the Root-Mean Square of Intensity Differences, MAD_{int} - Median-Absolute Deviation of Intensity Differences, and MID_{int} - Maximum Intensity Differences. The corresponding equations for RMS_{int} and MAD_{int} are:

$$RMS_{int} = \sqrt{\frac{1}{N}\left(I_F(x) - I_M(x)\right)^2}$$

$$MAD_{int} = Median\left(|d(x) - Median\left(d(x)\right)|\right)$$

where $I_{F(x)}$ and $I_{M(x)}$ are fixed and moving CT image intensities, respectively; $d(x) = I_{F(x)} - I_{M(x)}$.

In our analysis, the maximum intensity difference was defined as the intensity difference which was larger than 95% of all differences. For simplicity, we shall now refer to RMS_{int}, MAD_{int} and MID_{int} collectively as intensity-based measures. While these metrics may reflect the success of the optimization procedure in registering the images, they unfortunately do not assess the validity of the deformations computed by the algorithms, as will be shown later.

Qualitative validation involved the use of individual experts to assess image

registration through the use of difference images, or display tools such as image overlays. This method suffers from a lack of a quantifiable metric to rank the quality of a given registration, and like the calculated metrics, cannot clearly reflect the validity of the deformation fields. After the completion of image registration, two radiation oncologists identified reference points on selected anatomical and physiological landmarks (e.g., the most anterior, lateral and posterior extent of lung parenchyma, the junctions of the anterior and posterior mediastinum with chest wall and most lateral extent of mediastinal contour within each hemi-thorax) on the planning CT and registered CT sets in a double-blind study. The TRE was then calculated as the average distance between locations of these reference points as placed by radiation oncologists in the two CT sets.

Evaluation of SPECT-CT registration validity requires an additional assessment step. Since CT images were used as input images in the registrations, CT registrations were performed to preserve count density. However, we found that after the SPECT images were deformed and differences in voxel sizes were corrected, the difference in total SPECT counts before/after registration were small (within 3%). As commonly used in SPECT guided treatment planning studies [46, 47], functional volume were segmented using certain SPECT intensity as a threshold. Thus we compared the difference in the functional volume of SPECT images before and after registration through the use of activity histograms. The intensity histograms of the original SPECT and the registered SPECT images were calculated in voxels with more than 10% of maximum SPECT intensities. Then, we calculated the histogram difference of the SPECT intensities ($HIST_{SPECT}$) as the sum of absolute volume (instead of number of voxels to account for difference in voxel sizes) difference in each bin:

$$HIST_{SPECT} = \sum_i \left| V^i_{moving} - V^i_{registered} \right|$$

where V^i_{moving} and $V^i_{registered}$ are the volume of i th bin in the intensity histogram of the original and registered SPECT image sets, respectively. We adopted this metric to quantify the change seen in the SPECT image after application of the transformation. Although a small value of this metric does not necessarily suggest a good registration, a large value does indicate that substantial part of SPECT

activity distribution has been affected by registration.

We also scrutinized the spatial transformations to assess the plausibility of the deformation. The determinant of Jacobian of the displacement field gives information about local volume changes. It is defined as the determinant of the first partial derivatives of the transformation. Negative Jacobian values indicate inconsistent transformation, i.e. singularities or foldings. To assess the amount of singularities in the deformation field, we computed JAC_{disp}, the percentage of negative values in the Jacobian determinant as done in Urschler et al.[61]. Ideally this measure should be 0.

3.4 Results

The results of the six registration methods which were tested in this study, averaged over ten patients are shown in Table 3.1. We can see a marked improvement in the intensity-based measures from manually placed control points to automatic rigid registration, and the same trend again can be seen for automated rigid to non-linear registration. The reduction in image differences is consistent with the reduction of TRE based on experts' review (Table 3.1). However, from the visual examination of the registered SPECT images, we found that those generated from Level set and Demons registrations were not clinically realistic. Examples are shown in Figure 3.2 where false SPECT counts (local maxima in intensity values in highlighted regions) can be seen. This was largely due to singularities (folding, etc.) in the deformation field (Figure 3.3). We also examined the level of preservation in the activity distribution in the registered SPECT images; values of the SPECT-based metric are reported in Table 3.1 as $HIST_{SPECT}$. The average values of selected CT-based and SPECT-based metrics were normalized to the same scale and are shown in Figure 3.4. CT-based and SPECT-based metrics increase in opposite directions. This suggests that, while the use of non-rigid registration may result in improved alignment between registered CT images, the resolved deformations as obtained by the Demons and Level set registration algorithms actually did not result in valid registered SPECT images.

Table 3.1: Averaged results of the metrics used in this study

	Skin	Lung	Rigid	B-Spline	Demons	Level set
RMS_{int}(HU)	230.77	205.60	158.01	123.39	79.68	63.68
MAD_{int}(HU)	44.5	40.3	34	29.1	19.2	16.9
MID_{int}(HU)	577.4	507.5	358.5	258	167.9	110.5
TRE(mm)	5.63	3.81	3.28	1.90	1.12	0.68
$HIST_{SPECT}$ (mm^3)	7225	7832	6444	9594	18572	15483
JAC_{disp}(%)	0	0	0	0.2571	37.88	24.69

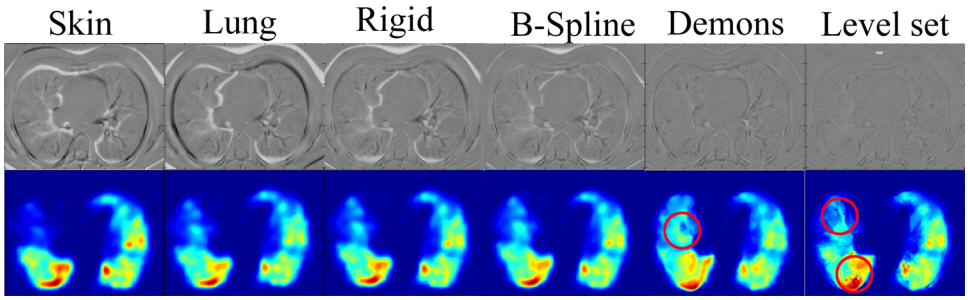

Figure 3.2: Above: Slices of the difference image computed between the *moving CT image* and the *fixed CT image* after each registration. Below: Slices of the SPECT images warped with the deformation field from each registration. Circles indicated areas where SPECT signals are clinically invalid.

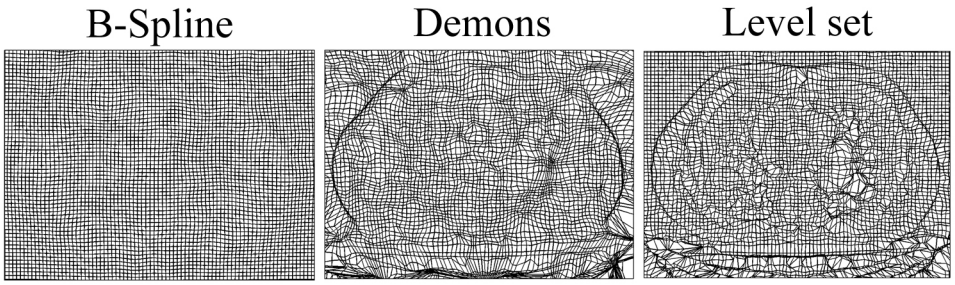

Figure 3.3: Slices of the deformation fields obtained from B-Spline, Demons and Level set registrations. These slices correspond to those shown in Figure 3.2

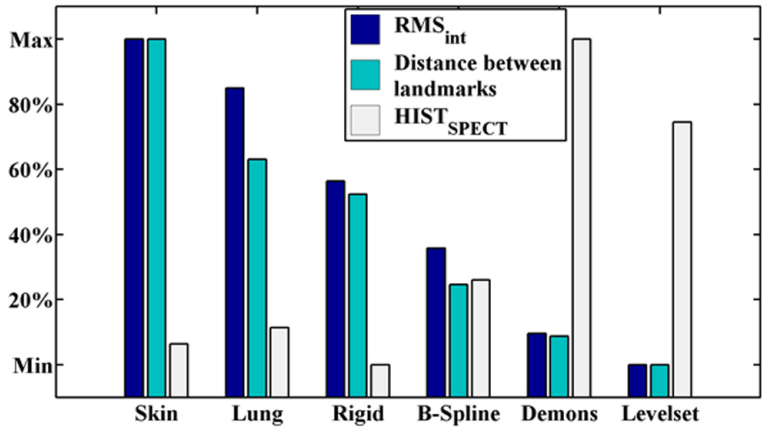

Figure 3.4: Renormalized average values of selected CT-based and SPECT-based metrics.

3.5 Discussion and Conclusion

In this study, we compared the accuracies of six CT-CT registrations methods, three of which were linear registration methods that have been previously reported [44–47, 50]. Of these three linear registration methods, Rigid (which is based on the mutual information computed from the intensities of both images and is not based on manually defined point correspondences) was demonstrated to perform the best based on the intensity metrics and anatomical landmarks. In the two control point-based registration methods, the Skin method was found to be inferior to the Lung method. This suggests that control points identified on anatomical landmarks in lungs provide better information for correct registration than those defined by the skin markers. We further introduced the use of three automated, non-rigid registration methods (B-Spline, Demons and Level set) for image registration in SPECT guided RT. Improvements in both the image intensity based metrics, and TRE based metrics were observed in all three the non-rigid methods. However, upon applying the deformation field obtained from Demons and Level set to the perfusion SPECT, it was determined that the activity distributions in the SPECT images were unacceptably altered. This was likely related to several factors outside the registration algorithm itself. First of all it is known that the quality of

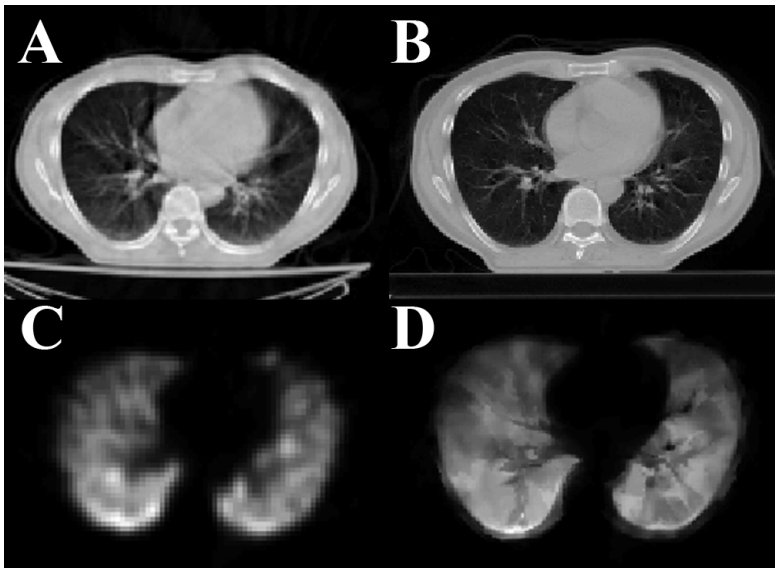

Figure 3.5: A sample of transaxial CT slice (A: *moving CT image*. B: *fixed CT image*) and SPECT images (C: original SPECT image. D: registered SPECT image from Level set registration). Invalid SPECT counts can clearly be seen in the gray scale.

CT images from SPECT/CT camera is not as good as that of the conventional CT images. The artifacts as well as noise may have impacted the robustness of the registration algorithms in such a way that they also correct for differences due to these artifacts and noise (Figure 3.5) rather than ture mis-matching between CT images, thus producing invalid deformation fields and warped SPECT images. Meanwhile, a typical planning CT scan takes several minutes, whereas SPECT and subsequent low resolution CT scans can take more than half an hour. All the participated patients had lung cancer and poor lung function, thus we did not make any additional efforts to allow for patients' comfort during the scans. Consequently, breathing motions during these scans, which are not accounted for or modeled by the non-rigid registration algorithms, may have also contributed to errors in registrations.

Neither intensity-based metrics, nor TRE based metrics reflected the problem of invalid deformation field in deformable registrations. This suggests that the use of metrics derived from CT image sets alone (i.e. based on control points or image similarity) does not adequately reflect the quality or accuracy of the actual regis-

trations. Consequently, in lieu of manually inspecting the obtained displacement fields and registered SPECT images, calculation of the JAC_{disp} and $HIST_{SPECT}$ measures served as a useful 'sanity check' on the registration solutions. We draw two important conclusions here:

1. When applying the deformation parameters obtained from registration of CT to CT, it is important to examine how the SPECT image will be deformed.

2. Controlling the smoothness of the displacement vector field by setting the regularization parameter is an important issue that can be crucial in deciding whether the resulting SPECT image is valid or not.

In the future work, the non-rigid registration algorithms will be modified so as to explicitly enforce volume-preservation (positive Jacobian), as proposed in Noblet et al.[62], and the preservation of SPECT count distributions. Further, we are currently exploring approaches for automatically setting the regularization parameters either based on training data or quantifying image reliability as in [63–65].

While this study focused on deformable co-registration for the purpose of registering SPECT images to the planning CT, the results have broader implications. Deformable co-registration is becoming a common feature of treatment planning systems and adaptive radiation therapy (ART). Properly implemented ART requires that doses to normal tissues and target volumes are tracked through treatment on a voxel-by-voxel basis [66]. Imaging modalities such as daily MVCT used in Tomotherapy can be used for the purpose of daily image acquisitions [67]. Currently published deformable co-registration studies have emphasized a need for daily MVCT pre-processing [68], and for the evaluation of co-registration accuracy using metrics similar to those used in this study, as well as visual examination of delineated contours. In this study, we had the benefit of inspecting the accuracy of co-registration by comparing pre- and post-warp SPECT intensity distributions in lung. We showed that certain quantitative evaluation methods of CT-CT co-registration have ranked the Demons and Level set methods as the best even though subjective evaluations of the deformed SPECT images did not indicate so. This applies to both metrics based on Hounsfield Units and calculations of TRE. The latter is often seen as a definitive clinical validation. This is unfortunate because

our experimental results have clearly shown that these measures are insufficient for validation purposes. We conclude that clinical implementation of ART should also incorporate subjective evaluations of registration results by oncologists, therapists, or physicists before treatment plan adaptations are made.

Chapter 4

SPECT Guided IMRT Treatment Planning

4.1 Motivation

As part of the pre-requisites for SPECT guided IMRT treatment planning, the impact of SPECT reconstruction on treatment planning and the accuracy of SPECT - planning CT registration have been investigated in Chapter 2 and Chapter 3 respectively. The next step is to prove the concept of the SPECT guided RT, and compare it with the conventional dose-volume constraints based IMRT treatment planning.

To achieve this goal, we aim:

1. To develop a method for IMRT optimization in lung cancer radiotherapy utilizing both lung perfusion SPECT information and Monte Carlo (MC) dose calculation.

2. To compare lung sparing of both anatomic and functional volume in IMRT plans generated with conventional dose-volume constraints versus SPECT-guided plans.

4.2 Beamlet Dose Calculation Algorithm Using Monte Carlo Simulation

An accurate dose calculation algorithm is the key component of a treatment planning system. In this study, we implemented a Monte Carlo based beamlet dose calculation algorithm and Direct Aperture Optimization (DAO) for IMRT treatment planning. The concept of Monte Carlo simulation and beamlet dose calculation are introduced in this section.

4.2.1 Importance of Dose Calculation Accuracy

Until recently, most of the dose calculation algorithms implemented in clinical treatment planning system were *kernel-based convolution* algorithms, such as the pencil-beam kernel algorithm [69, 70], the convolution-superposition algorithm [71] and the collapsed-cone algorithm [72]. In the pencil-beam kernel algorithm, the radiation field is segmented into a finite grid of small beamlets or pencil beams. The deposited dose from a single beamlet can be pre-calculated or measured as a dose *kernel*. Thus the total deposited dose is calculated as the convolution of primary photon fluences and the dose *kernel*.

$$D(x,y,d;SSD) = \frac{(SSD+{d_{ref}}^2)}{(SSD+d)^2} \int\int_{-\infty}^{+\infty} F(x',y') P_{int}(x',y',d) K(x-x',y-y',d) dx'dy'$$

where

- SSD = Source to Surface Distance
- d = depth of dose calculation
- d_{ref} = reference depth set by the user
- $K(x,y,d)$ is the measured or calculated dose deposition kernel of a pencil beam

The actual primary photon fluence is obtained by multiplying the idealized fluence $F(x',y')$ by a depth dependent off-axis intensity profile $P_{int}(x',y',d)$ which accounts for the off-axis scattering due to the flattering filter. This is an over-simplified method as the dose *kernel* $K(x,y,d)$ is assumed to be spatial invariant

without any corrections for differences in energy spectrum at different depths. It also lacks the ability to account for lateral electron scatter in materials other than water. It has been shown to miscalculate dose by as much as 15%, in the presence of inhomogeneous media, especially lung. Thus 1D path-length correction for regions of inhomogeneity, such as the Modified-Batho method, is often used to account for tissue inhomogeneities [73, 74]. However, the accuracy of these methods is not sufficient when applied to dose calculation in lung (Figure 4.1). Advanced models incorporating tissue inhomogeniety corrections such as collapsed-cone algorithm and analytical anisotropic algorithm can improve calculations to a certain degree. Nevertheless, the Monte Carlo method with simulation of radiation transport remains the gold standard for benchmarking dose calculation accuracy.

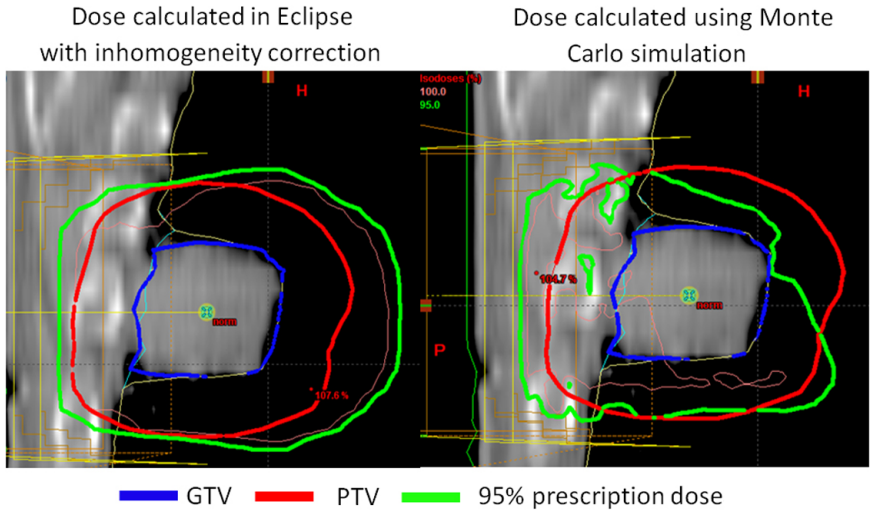

Figure 4.1: Comparison of dose calculated in SBRT treatment plans using pencil beam analytical algorithms and forward recalculation with Monte Carlo simulations. Left: Dose distribution from treatment plan optimized in Eclipse with inhomogeneity correction. PTV is well covered by the 95% prescription dose. Right: Dose distribution from the same plan but calculated using Monte Carlo. Significant under-dose in PTV can be found. (Image courtesy of Dr. Vitali Moiseenko)

The obstacle to implement Monte Carlo based methods into clinical treatment planning is the calculation time (usually $>$ 12 hrs) which is not clinically accept-

able. However for research purpose, the high computation time can be acceptable. In this study, we implemented a Monte Carlo based beamlet dose calculation method proposed by Bergman et al [75]. The accuracy and computation performance have been demonstrated elsewhere [75]. The following is a brief introduction of the general concept of Monte Carlo simulation in radiation therapy and beamlet dose calculation.

4.2.2 Monte Carlo Simulation Methods

The Monte Carlo method is a way of simulating physical and mathematical problems by stochastic sampling of random variables. In the Monte Carlo method, uniformly distributed random numbers are generated as an input. Given the specific probability density function in the problem, the distribution of input variables is transformed in to the distribution of the variables of interest. Thus it provides a means to simulate the processes of the physical systems.

For example, in the simulation of transport of x-ray photons through matter, several properties of this process can be simulated including:

1. Types of interactions (photoelectric effect, Compton scattering, pair production, etc)
2. The fraction of energy transferred from the photon to the scattered electron or the energy absorbed by the medium
3. The energies and directions of scattered photons and electrons.

The following is an example of Monte Carlo simulation in sampling scattered photons in Compton scattering. The Klein-Nishima formula gives the differential cross-section for photons with initial energy $h\nu$ in Compton scattering

$$\frac{d\sigma_c}{d\Omega_\theta} = \frac{{r_0}^2}{2}\left(\frac{h\nu'}{h\nu}\right)^2\left(\frac{h\nu}{h\nu'} + \frac{h\nu'}{h\nu} - sin^2\theta\right)$$

where θ is the scattering angle, r_0 is the classic radius of electron, $h\nu$ and $h\nu'$ are the energy of incident and scattered photons respectively.

$$h\nu' = \frac{h\nu}{1+\alpha(1-cos\theta)}; (\alpha = h\nu/0.511MeV)$$

Thus the differential probability density function which is the probability of having photons scattered at angle θ is given as

$$p(\theta) = \frac{\frac{d\sigma_c}{d\Omega_\theta} \cdot 2\pi sin\theta}{\int_0^\pi \frac{d\sigma_c}{d\Omega_\theta} \cdot 2\pi sin\theta d\theta} = \frac{1}{\sigma_c} \frac{\pi sin\theta \cdot {r_0}^2 \cdot \left[1 + cos^2\theta + \alpha^2 \cdot \frac{(1-cos\theta)^2}{1+\alpha(1-cos\theta)}\right]}{\left[1+\alpha\left(1-cos\theta\right)\right]^2}$$

where σ_c is the total cross section of Compton scattering

$$\sigma_c = 2\pi {r_0}^2 \left\{ \frac{1+2\alpha}{\alpha^2} \left[\frac{1+\alpha}{1+2\alpha} - \frac{ln(1+2\alpha)}{\alpha} \right] + \frac{ln(1+2\alpha)}{2\alpha} - \frac{1+3\alpha}{(1+2\alpha)^2} \right\}$$

Note that the azimuthal dependence of the solid angle has been integrated out in this equation. Cumulative density function $P(\theta)$ can be calculated from the integral of of differential density function:

$$P(\theta) = \int_0^\theta \frac{d\sigma_c}{d\Omega_\beta} \cdot 2\pi sin\beta d\beta$$

and also be used to sample the scattered angle θ from uniformly distributed random variables. Assume photons with initial energy 5 MeV are simulated. For each photon, the following steps are carried out in the simulation

1. Generate a random variable r which is uniformly distributed from 0 to the maximum of $P(\theta)$
2. Solve the angle θ which gives $\theta = P^{-1}(r)$. This will be the scattered angle of the photon simulated in Compton scatterring.

The above process can be repeated for every photon for particular interaction (Figure 4.2 and Figure 4.3) until a statistically large number of photons have been simulated. When it is difficult to solve the cumulative density function, an *Acceptance Rejection Method* can also be used to simulate the scattering process of photons.

At a microscopic scale, using this approach, a *history* of each photon in the Compton scattering can be created for analysis. This *history* includes the angle and energy of the scattered photons, as well as the scattered electrons. Furthermore, other types of reactions such as photoelectric effect and pair production for

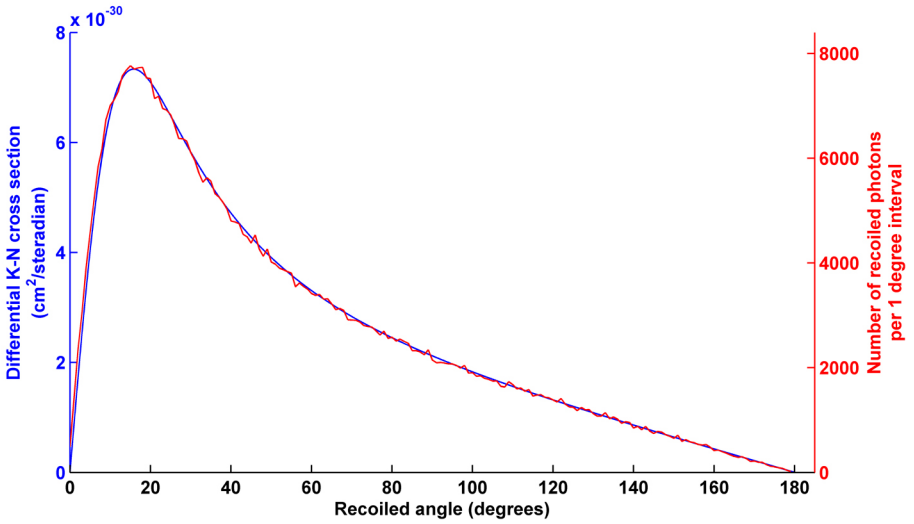

Figure 4.2: Differential K-N cross section from analytical calculation (blue) compared to distribution of photon recoiling angles in Monte Carlo simulation (red). 5×10^5 photons with initial energy 5MeV were simulated.

photons or scattering of secondary electrons can also be simulated thus giving a more realistic simulation of high energy photon transport in the media.

At a macroscopic scale, when the initial and subsequent reactions of millions of photons are simulated, the history of every photon or daughter particles from the secondary interactions can be recorded. In the context of medical physics, the big picture of particle transport can be accumulated from the histories of all the photons and other particles. This big picture includes information such as frequency of certain type of reactions, spatial and energy distribution of particles as they go through different materials and the energy deposition at different locations which are used for Monte Carlo dose calculation in radiation therapy physics.

4.2.3 Simulation Using BEAMnrc and DOSXYZnrc

Several Monte Carlo radiation transport code packages have been published for applications in radiation therapy, such as EGSnrc, VMC++, GEANT4, etc. The EGSnrc (Electron Gamma Shower - National Research Council) code was developed from 1970's to 1980's by Stanford University and the National Research

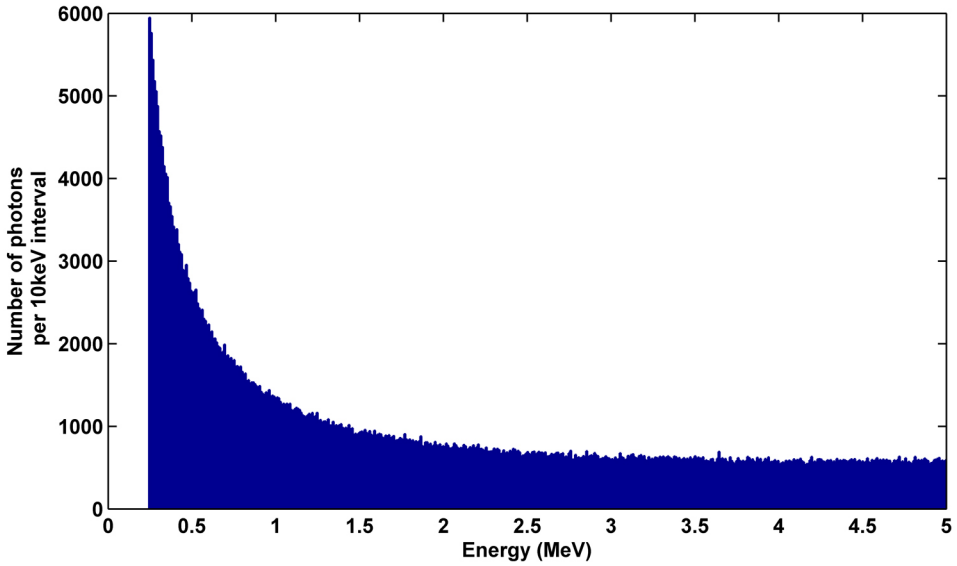

Figure 4.3: Energy distribution of recoiled photons in Monte Carlo simulation of Compton scattering. 5×10^5 photons with initial energy 5MeV were simulated.

Council of Canada [76]. It is capable of simulating the radiation transport of charged particles or photons in almost any compound or mixture medium. A broad range of particle energies can be simulated (from $\sim$1keV to several thousand GeV).

The types of interactions that can be simulated for the x-ray photon transport includes those predominant in radiation therapy such as photoelectric effect, Rayleigh (coherent) scattering, Compton (incoherent) scattering and pair production. The electrons set in motion in these primary interactions produce a cascade of secondary particles and photons (electron shower). These electrons undergo a continuous energy loss due to radioactive loss generating photons in Bremsstrahlung radiation or collisional loss causing excitation or ionization of atoms which can also be simulated in EGSnrc.

In this study, two different Monte Carlo simulation codes based on EGSnrc were utilized. The BEAMnrc code was used to simulate radiation transport from the LINAC to the patient's body. The result from BEAMnrc simulation was used to calculate energy deposition (dose) in the patient's body by the DOSXYZnrc code.

BEAMnrc code

The BEAMnrc code is a Monte Carlo simulation system for modeling radiation sources used in modern radiation therapy. This code was developed in 1995 as part of the OMEGA project with collaboration between National Research Council of Canada and the University of Wisconsin [77]. In the BEAMnrc code, the geometry, material composition and relative geometry of different components of a virtual LINAC are pre-specified based on those from the manufacturer manual for a real LINAC (Figure 4.4). These components include:

1. Target and primary jaws
2. Flattering filter
3. Built-in ion-chamber (to monitor radiation output)
4. Mylar mirror
5. Two pairs of secondary collimating jaws in X, Y directions

The above component modules are necessary for simulating radiation transport within a LINAC. Depending on specific radiation therapy applications, additional modules such as compensators or MLC can also be added at the end of the component module chain in the simulation.

At the beginning of the BEAMnrc simulation, the energy and spread (full width half maxima of a Gaussian shape) of the incident electron beam on the tungsten target is specified by the user. The x-ray spectrum emitted from the target and the particle transport through different component modules along the direction of radiation beam are sequentially simulated in BEAMnrc. The result of the simulation is a *phase space* file which contains the tracking histories of primary photons and other secondary particles emerging from the target. More specifically, this includes the trajectories of photons or electrons (direction, energy, location of last interaction, etc) and the amount of energy deposited in locations of interest. This information is recorded at a *scoring plane* perpendicular to the direction of radiation beam at a user specified distance away from the target.

This *scoring plane* or *phase space* is usually located at the end of the component modules which will not change. It can be used to calculate the radiation

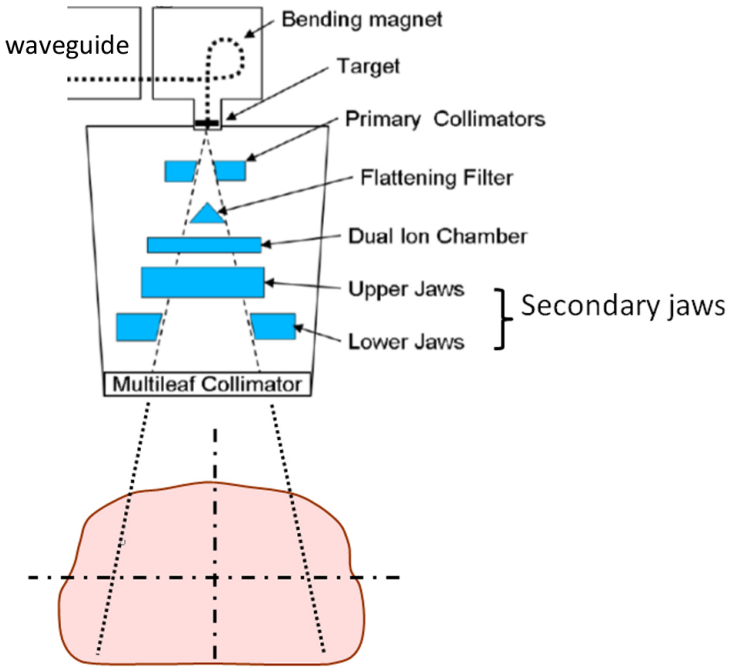

Figure 4.4: Schematic of components in a virtual LINAC

output, profiles of beam intensity, energy spectra etc., of a virtual LINAC and compared against those measured from a true LINAC. Thus the parameters of the incident electron beam (energy, spread, etc.) can be fine-tuned to match the real measurement. It can also be used to analyze radiation from different component of the LINAC. When the *scoring plane* is placed above the MLC or secondary jaws, it can be re-used by the BEAMnrc when the field size (defined by MLC or secondary jaws) has changed. Thus the radiation transport in the components above which it has not changed does not need to be re-simulated. The CT scans of a patient can be converted into a virtual ”phantom” with accurate calibration and conversion between CT numbers and electron density. The *phase space* file can also be directed at this patient phantom for the purpose of calculating absorbed dose in DOSXYZnrc.

DOSXYZnrc code and absolute dose calculation

Similar to the BEAMnrc code, DOSXZYnrc code is also an EGSnrc based Monte Carlo simulation package [78]. The intent of this code is to calculate absorbed radiation doses within a 3D voxelized phantom. This phantom can be manually constructed by the user or generated from a set of CT scan which requires an accurate calibration curve between CT numbers and electron density. The density, interaction cross-section of different media in this phantom are defined according to the ICRU (International Commission on Radiation Units) standard. Pre-simulated *phase space* file can be used as the radiation beam directed at the patient phantom.

The result of the DOSXYZnrc simulation is a ".3ddose" file which contains the dose distribution in a matrix format, including the location of the first voxel and the number of voxels in x,y,z direction, the size of each voxel, and the dose deposited in each voxel. The dose reported in this file is normalized to Gy per incident electron on the target.

$$D_{abs} = D_{xyz} N_e$$

where D_{abs} and D_{xyz} are absolute dose (Gy) and renormalized dose (Gy per particle) respectively. N_e is the number of incident electrons on the target.

During the treatment, the radiation output from a real LINAC is measured by built-in ion-chambers in the LINAC head assembly. The output is reported in the number of monitor units (MU). The calibration of a real LINAC invloves measurements with another calibrated ion-chamber placed in the water phantom. The calibration protocol presently used in clinic, TG-51 [79] requires that measurements are performed at 10 cm depths and the LINAC is calibrated to deliver 1 cGy per MU at a reference depth. This calibration process of a real LINAC can also be simulated in Monte Carlo, thus the number of electrons incident on the built-in ion-chamber in the LINAC head per MU can be obtained by comparing the relative dose (dose per particle) and calibrated absolute dose (1 cGy in TG-51 protocol) at the measurement point. Taking electron back-scatter from the jaws and MLC below the built-in ion-chamber into account, the absolute deposited dose in the Monte Carlo simulation can be calculated as [80]:

$$D_{abs} = D_{xyz} \times \frac{0.2053Gy}{2.461 \times 10^{-15}Gy + D_{ch}^{back}} MU$$

where D_{ch}^{back} is the dose delivered to the built-in ion-chamber per back-scattered electron which depends on the size of the field, usually on the order of 10^{-17} Gy per incident particle. Note that the numbers in this equation were obtained from LINAC specific simulations, thus slight variation between different LINAC can be expected. In general, it was found that 1 MU corresponds to

$$N_e = 8.129 \times 10^{13} \pm 1.0\%(per\ \ MU)$$

electrons incident on the target for a Varian Clinac 21EX accelerator model [80].

4.2.4 Beamlets Separation and Dose Calculation

As mentioned earlier the BEAMnrc *phase space* is a collection of histories recorded for each particle crossing the *scoring plane*. The history of each particle is stored as either 7 or 8 variables including (in this order) LATCH, energy (MeV), X-position (cm), Y-position (cm), X-direction cosine, Y-direction cosine, particle weight, and Z-position of the last particle interaction (optional). Depending on the scoring mode chosen in BEAMnrc, each variable usually occupies 32 bits in the *phase space* file. The first LATCH variable (bits 1 to 23 of the 32-bit variable) is allocated to the geometric mapping of each particle's history. If a particle passes through or interacts in a geometric region with an assigned mapping the corresponding LATCH bit is set to 1. In this way one can determine from the resulting phase space which particles interacted in different regions in the accelerator. Bits 24 to 28 in the LATCH variable are used to record the geometric region in which a secondary particle was created. Bits 29 and 30 store the charge of the particle and whether or not the particle is a contaminant particle. Bit 31 is used to record particles which cross the scoring plane more than once. Finally, bit 0 is used to record whether a bremsstrahlung or positron annihilation event occurs in the particle's history.

In the Monte Carlo based beamlet dose calculation the LATCH variable is mod-

ified to map small beam elements (beamlets) to binary beamlet numbers [81]. The method of generating beamlets begins with a *phase space* that has already been simulated by the accelerator model. This *phase space* is set just above the MLC which is 65cm away from the target in our LINAC model. The chosen *phase space* is then divided up by placing on it an invisible grid of beamlets with individual size 2.5mm x 5mm (Figure 4.5). The total number of beamlets is determined by rounding down the size of the field divided by the size of the beamlets at each direction. Partial beamlets on the outer border of the grid are not used to avoid potentially low statistical reliability. For inverse treatment planning, the outer boundary is specified by the X and Y jaws of the secondary collimator. The beamlets are labeled from 1 to N. The *phase space* is then read in particle by particle, and the beamlet it belongs to is determined by the x and y positions of each particles in the *phase space*. All particles lying outside the specified grid are included in a single beamlet (labeled $N+1$). The beamlet index of each variable is converted to binary code and stored in bits 1 to 21 of the LATCH variable.

After the beamlet index has been assigned to each particle in the phase space, a sorting algorithm is used to sort and separate particles of identical LATCH value into smaller individual phase space files. The BEAMnrc and DOSXYZnrc input files are also modified to assure that the number of simulations for each particle is consistent with those before the LATCH filtering. An example of the DOSXYZnrc simulation of a beamlet *phase space* is shown in Figure 4.6.

During the treatment planning, D_i, the dose deposited at voxel i, can be calculated using the beamlets from the Monte Carlo simulation

$$D_i = \sum_j w_j \cdot D_i^j$$

where D_i^j is the dose contributed by beamlet j to the voxel i. w_j is the weight of each beamlet which can be modulated in direct aperture optimization (DAO).

4.2.5 Validation of Dose Calculation Accuracy

The accuracy of Monte Carlo based beamlet dose calculation in direct aperture optimization has been previously reported elsewhere [75]. The dose distributions

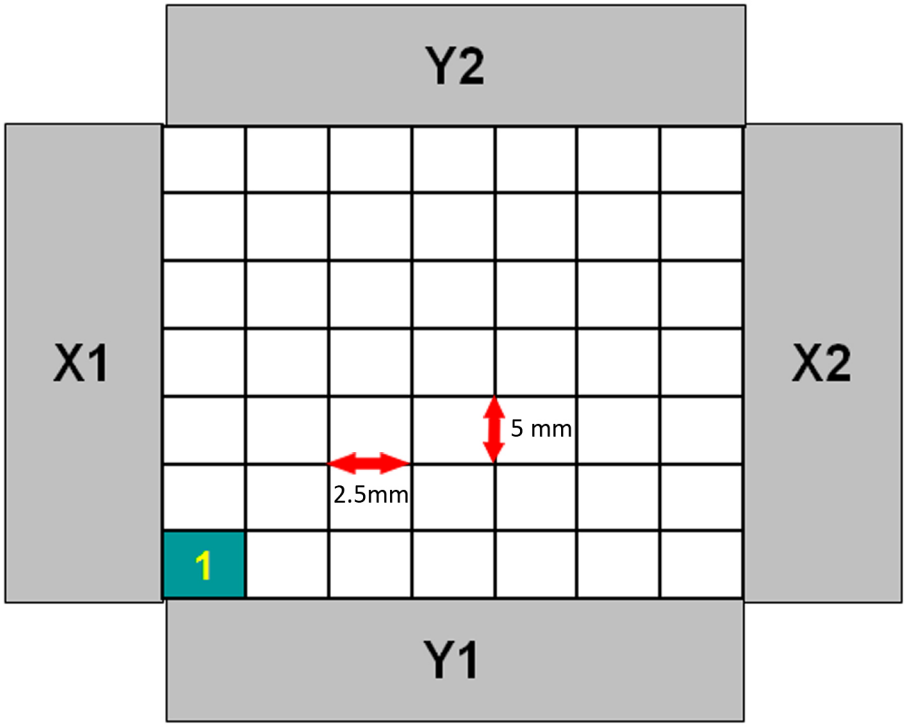

Figure 4.5: The grid used to assign the beamlet index. (The size of grid is not drawn to scale)

from IMRT plans can be calculated separately using Monte Carlo generated beamlets and Monte Carlo simulation without segmenting *phase space* into beamlets. The result from the beamlet dose calculation was found in good agreement with Monte Carlo simulation as well as film measurement. Various methods have been used to compare dose calculated using different methods, such as line dose profile, dose difference, distance-to-agreement, iso-dose lines etc. In order to compare complex dose distributions as usually seen in clinical IMRT plans, the gamma factor is proposed as a composite analysis method offering more quantitative comparison based on both dose difference and distance-to-agreement metrics. It is currently used as the quality assurance (QA) method for dose calculation in IMRT plans of patient in our clinic. In this study, in order to validate the accuracy of the beamlet dose calculation in the intrathoracic region, we performed gamma factor

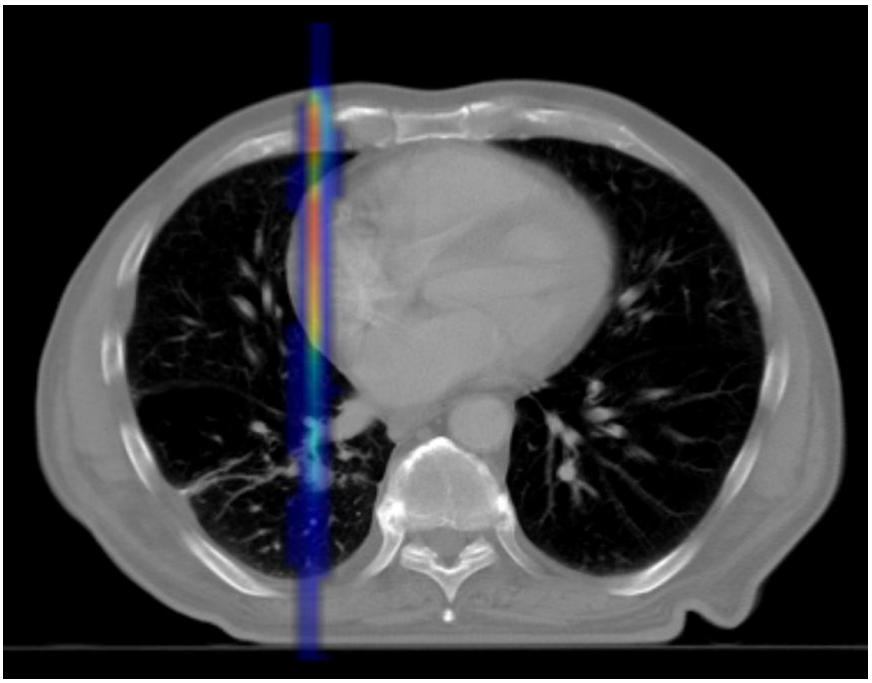

Figure 4.6: Dose distribution of one beamlet

analysis for dose calculated using Monte Carlo generated beamlets.

Dose difference (DD) is most useful for comparing regions where the dose gradient are quite low [82].

$$\%\%DD = \frac{calculated\ \ dose - measured\ \ dose}{calculated\ \ dose} \times 100\%$$

However, in the simple example of a one dimensional open field dose profiles, it is clear that the DD is very sensitive to small shifts in the isodose line positions in high-gradient regions. Meanwhile, distance-to-agreement (DTA) which calculates the distance from a point of interest to the same dose value nearby is a more robust metric of dose difference in high gradient region.

Note that, DTA can be very large in low gradient regions where DD is usually small. It rapidly becomes clear that both DD and DTA are essential in order to comprehensively assess the difference between different dose distributions. The gamma analysis proposed by Low et al. [83] is the most widely used to describe the

quality of agreement of two dose distributions. The acceptability criteria suggested by Van Dyk et al. [82] is a 3% dose difference and 3 mm distance-to-agreement. The implementation of gamma analysis for comparing 3D dose distributions is essentially a voxel by voxel calculation of gamma factor:

$$\Gamma(r_m, r_c) = \sqrt{\frac{r^2(r_m, r_c)}{{\Delta d_m}^2} + \frac{\delta^2(r_m, r_c)}{{\Delta D_m}^2}}$$

$$\gamma(r_m) = minimum\{\Gamma(r_m, r_c)\}, \quad for \ \ all \ \ r_c$$

where

- $r(r_m, r_c)$= the distance between measurement (r_m) and calculation point (r_c)
- Δd_m= maximum distance-to-agreement considerable (often set to 3mm)
- $\Delta(r_m, r_c)$= percentage difference between dose at r_m and r_c
- ΔD_m= maximum percentage dose difference considerable (often set to 3%)

The acceptance criteria of IMRT dose calculation QA currently used in our clinic requires more than 95% of voxels having gamma factors $\gamma(r_m)$ less than 1. The following is an example of the gamma analysis of IMRT plans optimized with DAO and Monte Carlo generated beamlets dose calculation (Figure 4.7).

The gamma analysis is performed in the regions which have more than 50% of prescription dose (Gy). More than 95% voxels in this region passed the test. Figure 4.8 is an example of iso-dose lines in dose calculated using beamlets and Monte Carlo simulation.

Although the Monte Carlo generated beamlets dose calculation is an accurate method, it would be worthwhile to note that, several factors can contribute to the uncertainty of the dose calculated using this method. The transmission at the round tip of MLC leaf (typically 40% for 6MV photon beams) is much larger than the remaining part of the leaf (1.6% as used in Eclipse treatment planning system). Thus the assumption that the beamlet can be "opened" or "closed" by the MLC leaf in a binary fashion does not always apply. Interleaf leakage also contributes

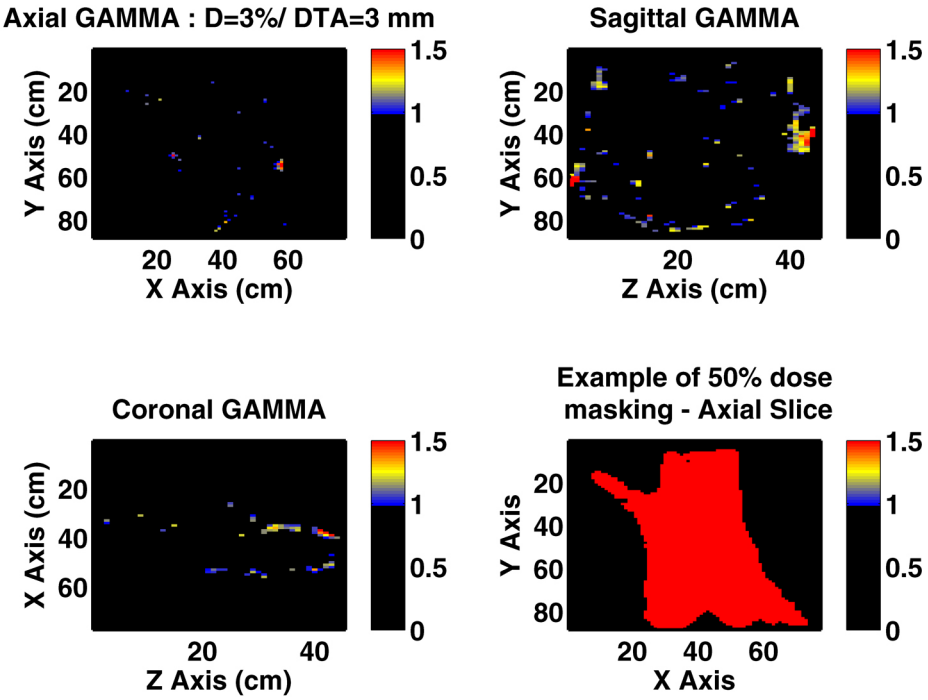

Figure 4.7: 2D distribution of Gamma factors. Color scales are truncated to show only those voxels larger than 1. Note that the gamma analysis is carried out in the volume¿50% prescription dose, i.e. red regions in right bottom figure

to dose errors outside the field. In order to maintain statistical accuracy when the phase space is segmented in to beamlets, the number of simulated particles or histories should be much larger than the number usually used for BEAMnrc and DOSXYZnrc simulations in the intrathroacic region.

4.3 Inverse Planning

IMRT treatment planning, due to the scale of parameters that need to be solved, is usually conducted as inverse planning where the treatment plan is designed in an iterative trial and error process. An accurate dose calculation algorithm is required to calculate the dose delivered to the patient. Other than the dose calculation

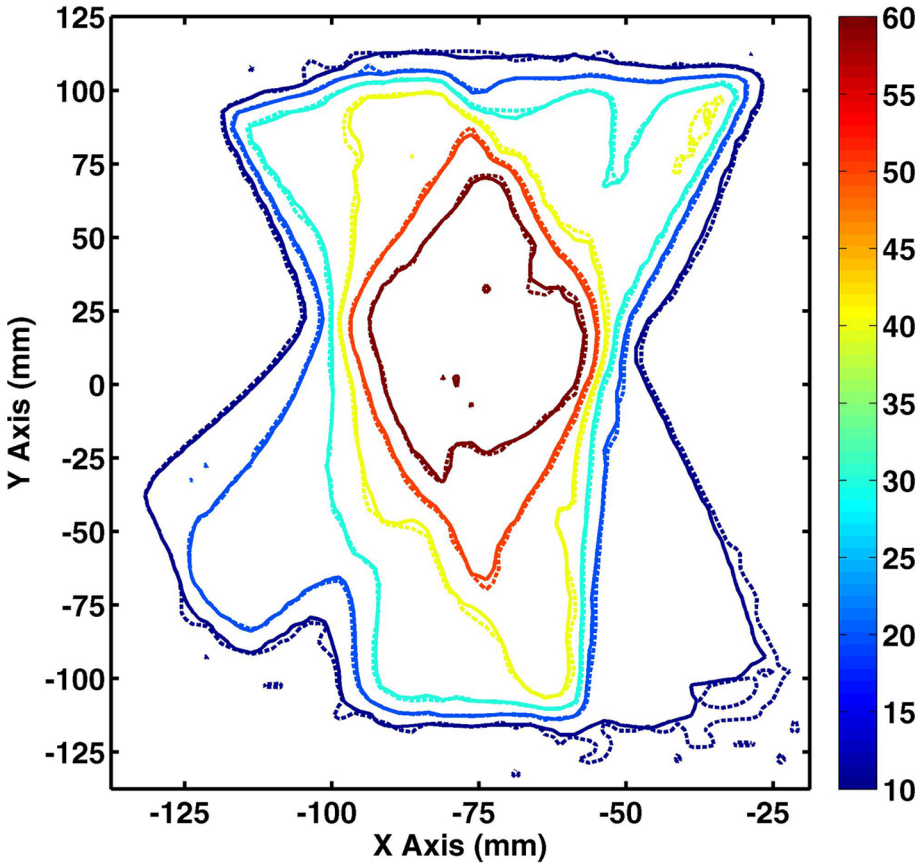

Figure 4.8: 2D Isodose shows good qualitative agreements between dose calculated using beamlets (solid line) and Monte Carlo simulation (dashed line). The iso-dose lines are set at 10Gy interval from 10Gy to 60Gy.

algorithm, there are two main components involved in IMRT inverse planning optimization.

1. The objective function serves as a metric to quantitatively compare the different setups of treatment parameters (gantry angle, fluence of each beam, etc) during treatment planning. The objectives of current RT treatment planning include i) delivering the prescription dose uniformly to PTV and ii) minimizing dose delivered to Organ At Risk (OAR). Thus the mathematical

format of the function is usually designed to calculate the fractional volumes of PTV and of OARs which do not meet the dose volume constraints of each structure. However the objective function can be formulated in such a way that the functional and the physiological information can be incorporated into the treatment planning. Thus the objective function is directly related to the clinical outcome or the functional sparing of OARs. Treatment plans with optimal clinical outcome rather than optimal dose distribution can be generated using this methodology.

2. The optimization algorithm searches the solution space for parameters which will minimize or maximize the value of the objective function. These parameters are used to modulate the fluence of each beam. They are iteratively adjusted during the inverse planning until the objective function reaches a global minimum or maximum. Various optimization algorithms focusing on how to efficiently adjust these parameters throughout the optimization process have been proposed and implemented in RT treatment planning.

4.3.1 DVH Based Objective Function

The first step in IMRT treatment planning is to construct the mathematical formulation of the objective function which is used to guide the process of inverse treatment planning. As discussed in Chapter 1, dose volume indices are correlated with different clinical outcomes such as normal tissue toxicities and tumor control. Thus in conventional IMRT treatment planning, these indices are usually incorporated into objective function as dose-volume constraints for optimizing treatment plans. The most commonly used type of objective function is the least square function [84]:

$$f = \sum_{i,j} w_j \cdot \left(D_{i,j} - D_j^p \right)^2$$

where w_j is the weight of structure j which renders the relative importance of each structure in radiation therapy. D_{ij} is the dose in ith voxel in structure j, D_j^p is the prescription or desired dose in structure j.

The optimization algorithm will search the solution space to find a plan which

minimizes f thus reducing the difference between calculated dose D_{ij} and prescribed or desired dose D_j^p. This equation is an over-simplified one as it is impossible to give each structure a uniform dose and it ignores the dose volume constraints required by radiation oncologists. A more sophisticated objective function which incorporates dose-volume constraints on inhomogeneous dose distribution is usually used.

$$f = f_{Target} + \sum f_{OAR}$$

where the PTV part of the objective function f_{Target} includes both minimum and maximum dose constraints thus a uniform dose distribution within target can be achieved.

$$f_{Target} = \frac{1}{N}\left[w_{min} \cdot \sum_j H(D_{min} - D_j) \cdot (D_{min} - D_j)^2 + w_{max} \cdot \sum_j H(D_j - D_{max}) \cdot (D_j - D_{max})^2\right]$$

w_{min} and w_{max} are weights for maximum and minimum dose (D_{min} and D_{max}) constraints in target. D_j is the dose in jth voxel, N is total number of voxels in the structure. The step function $H(x)$ is used to avoid penalizing for overfulfilling the constraint.

$$H(x) = \begin{cases} 0, x < 0 \\ 1, x \geq 0 \end{cases}$$

The OAR part of the objective function includes multiple dose-volume constraints for each OAR

$$f_{OAR} = \frac{1}{N}\left[w_{OAR} \cdot \sum_j H(D_j^{V_{x\%}} - D_{V_{x\%}}) \cdot (D_j^{V_{x\%}} - D_{V_{x\%}})^2 + \cdots\right]$$

where w_{OAR} is the weight for each dose-volume constraints in the OAR. $V_{x\%}$ is the x% "hottest" volume of each OAR, $D_j^{V_{x\%}}$ is the dose in each voxel of this sub volume and $D_{Vx\%}$ is the dose constraint for this sub-volume.

For example in Figure 4.9, no more than 15% of lung volume can receive dose exceeding 20Gy in RT, this will set $D_{V_{15\%}}$ equal to 20Gy. If dose of any voxel in

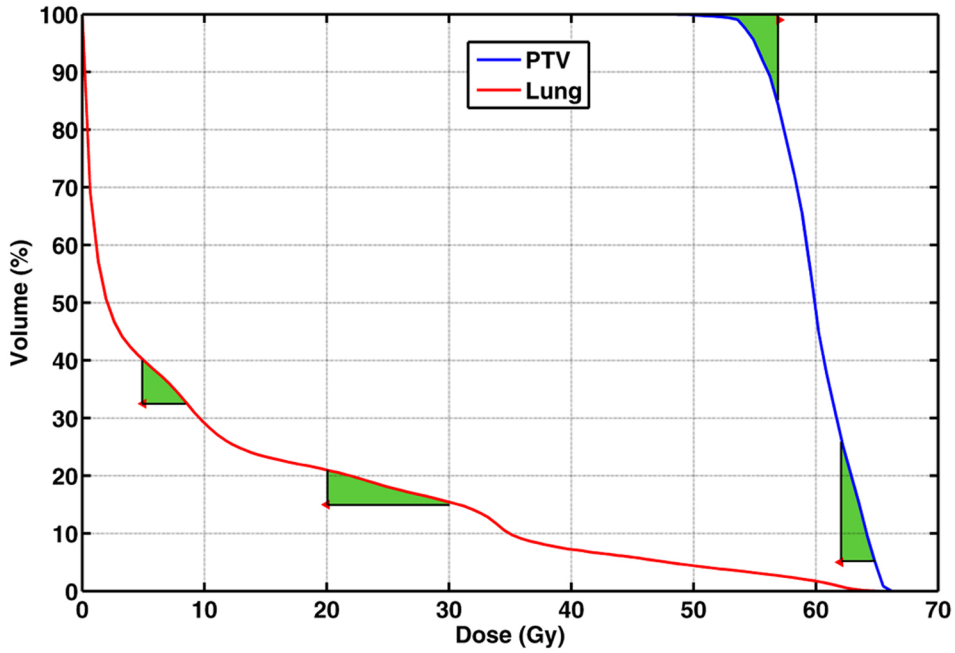

Figure 4.9: DVH of PTV and lung. Maximum and minimum dose volume constraints are placed as red markers on the figure. The green area represents those voxels which violate these constraints.

this sub-volume $V_{15\%}$ notated as $D_j^{V_{15\%}}$ exceeds 20Gy, the objective function will be punished by the step function $H(x)$.

4.3.2 SPECT Based Objective Function

As proposed in Chapter 2, SPECT Weighted Mean Dose (SWMD) is a more robust metric of functional sparing that functional lung segmentation approach as it produces more consistent results when different SPECT reconstruction algorithms are employed. Thus in the SPECT based objective function, we incorporate SWMD as one of the optimizing objectives to minimize functional damage on lung in RT treatment planning.

$$SWMD = \frac{\sum_i S_i \times D_i}{\sum_i S_i}$$

where S_i and D_i are SPECT counts and dose in voxel i, respectively. The rest of planning objectives also include delivering uniform dose to PTV while minimizing dose delivered to OAR (other than lung). However, instead of using dose-volume constraints, Equivalent Uniform Dose (EUD) is introduced as optimization constraints for all the other structures. Niemierko first proposed the concept of EUD for tumors which takes into account the effect of dose fractionation and tumor response using mechanistic formulation and linear-quadratic model [85]. If uniformly delivered, EUD will lead to same cell kill in the tumor volume as a non-uniform distribution from a treatment plan. Thus it is biologically equivalent to the non-uniform dose distribution. The EUD (also know as effective dose, D_{eff}) concept has been used to manipulate DVH for normal tissues in numerous studies. The main purpose of this is to make a complex shaped DVH interpretable and also to rank and accept/reject treatment plans. A commonly used phenomenologic formulation of EUD, which is also used in the popular LKB NTCP model [8], is based on a power law:

$$EUD = \left(\frac{1}{M} \sum_{i=1}^{M} D_i^{1/n} \right)^n$$

where M is the number of voxels in each structure.

The fitting parameter n can be derived from correlation between dose-volume indices and actual clinical outcome, thus it represents the volumetric response characteristics of different normal tissues (see Section 1.2.3). For tumor response this power can also be applied, the parameter $a = 1/n$ takes negative values and is indicative of sensitivity to cold spots, as described in [86]. It has been demonstrated that treatment plans optimized based on EUD can still meet conventional dose-volume constraints for each structure [86]. Recently several commercial treatment planning system (TPS) have provided EUD based optimization as an option in lieu of DVH based optimization.

In this study, the objective function utilizing both SWMD and EUD for optimization is formulated based on the logistic function proposed by Wu et al.[87] with a few modifications.

In the target part of the objective function f_{Target} :

$$f_{Target} = \frac{1}{1+\left(\frac{EUD_0}{EUD_{Target}}\right)^{\gamma_{Target}}} \times \frac{1}{1+\left(\frac{\mu_{Target}}{\mu_0}\right)^{\gamma_h}}$$

EUD_0 is the desired EUD (constraints) for the target. EUD_{Target} is the calculated target EUD with n set equal to -0.1, which, if recast with a reciprocal value means $a = -10$. γ_{Target} sets the priority of f_{Target} as compared to other structures since it controls the steepness of f_{Target} as a function of EUD_{Target} (Figure 4.10).

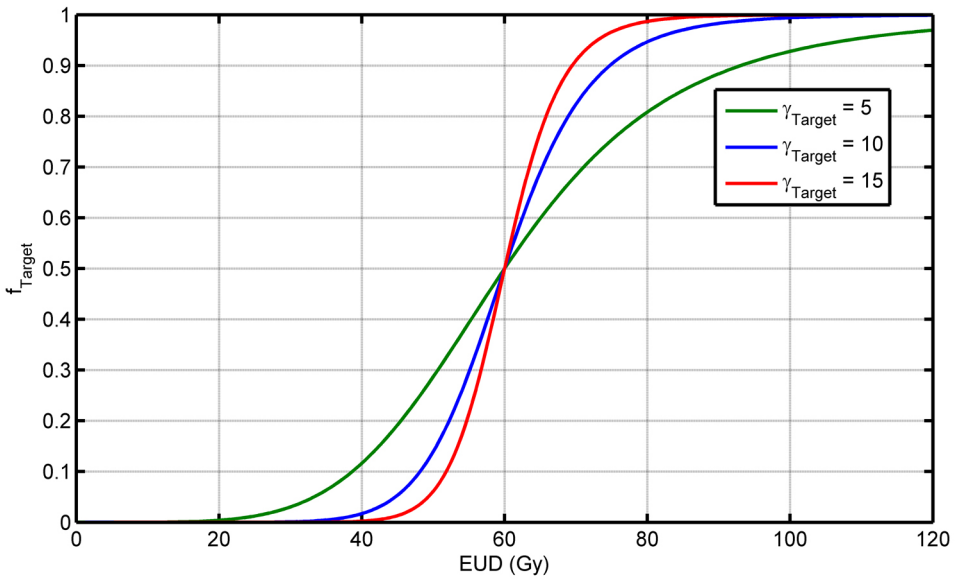

Figure 4.10: Steepness of f_{Target} as a function of γ_{Target}

It was found that the original EUD based objective function for target as proposed by Wu et al.[87]:

$$f_{Target} = \frac{1}{1+\left(\frac{EUD_0}{EUD_{Target}}\right)^{\gamma_{Target}}}$$

does not constrain the dose inhomogeneity in the target volume. A non-uniform dose distribution in PTV is often seen in EUD based treatment planning where dose hotspots can be delivered to the centre of PTV leaving cold spots at the pe-

riphery of the PTV. In the previous study, PTV was treated as both the "target" and the "OAR" to limit their dose inhomogeneity. Here, we introduce a new term to directly account for dose inhomogeneity

$$\frac{1}{1+\left(\frac{\mu_{Target}}{\mu_0}\right)^{\gamma_h}}$$

where μ_0 is the desired dose inhomogeneity in the target volume. μ_{Target} is the actual dose inhomogeneity calculated using $std(D)$ (standard deviation of target dose) and $Mean(D)$ (mean target dose). γ_h sets the priority for optimizing dose homogeneity.

$$\mu_{Target} = \frac{std(D_{Target})}{Mean(D_{Target})}$$

The optimization algorithm will search for different sets of beam parameters to increase EUD_{Target} and minimize μ_{Target} in order to maximize f_{Target}. Meanwhile the objective functions for OAR are formulated as slightly differently with constraint EUD_0 and priority γ_{OAR}, but f_{OAR} will increase with smaller EUD_{OAR} thus minimizing dose delivered to the OAR.

$$f_{OAR} = \frac{1}{1+\left(\frac{EUD_{OAR}}{EUD_0}\right)^{\gamma_{OAR}}}$$

The SWMD based objective function for lung f_{SWMD} is similar to this for OAR except that the constraint EUD_0 and the actual EUD are replaced by the constraint $SWMD_0$ and the actual $SWMD$ calculated in the lung volume, respectively.

$$f_{SWMD} = \frac{1}{1+\left(\frac{SWMD}{SWMD_0}\right)^{\gamma_{SWMD}}}$$

Since the optimization algorithm employed in this study is designed to search for global minimum of the objective function, the overall objective function is formulated as one minus the product of f_{Target}, f_{OAR} and f_{SWMD}.

$$f = 1 - f_{Target} \times f_{OAR} \times f_{SWMD}$$

Either maximizing target EUD and PTV dose homogeneity or minimizing SWMD and EUD for lung and other OAR will generate a smaller value of f. Thus conventional DVH driven or SPECT driven IMRT treatment plans can be generated by minimizing DVH based or SWMD based objective functions using the same optimization algorithm in inverse planning.

4.3.3 Fluence Based Optimization

The last step of IMRT treatment planning is to optimize the fluence of each radiation beam such that the delivered 3D dose distribution in the patient will minimize the objective function. Different types of parameters can be used (optimized) in the inverse planning to modulate beam fluence. Two common optimization techniques are used in IMRT treatment planning: Fluence based optimization and Direct Aperture Optimization (DAO).

In fluence based optimization, each radiation field is segmented into a grid of small beamlets, as done in Figure 4.11. Since the fluence pattern across the entire radiation beam is often inhomogeneous, each beamlet can be assigned an individual fluence or weight x_j, where the fluence or intensities of beamlets from all radiation beams can be written in a vector format $\vec{x} = x_j$, j is the index of each beamlet. Based on x_j, 3D dose distribution can be calculated using pencil beam kernel algorithm or the aforementioned Monte Carlo based beamlets dose calculation algorithm which provides better dose accuracy in heterogeneous region.

In fluence based IMRT optimization, x_j are optimized to minimize the objective function. In most treatment planning systems, this is usually done by the Conjugate Gradient (CG) Method [88]. In this method, $\vec{x}^{k+1}$, the vector x_j in $k+1$th iteration is adjusted by adding another vector $t \cdot \vec{d}^k$ to x_j from the previous iteration with

$$\vec{x}^{k+1} = \vec{x}^k + t \cdot \vec{d}^k$$

where $\vec{d}^k$ gives the change in the direction, i.e. the direction of optimization and t

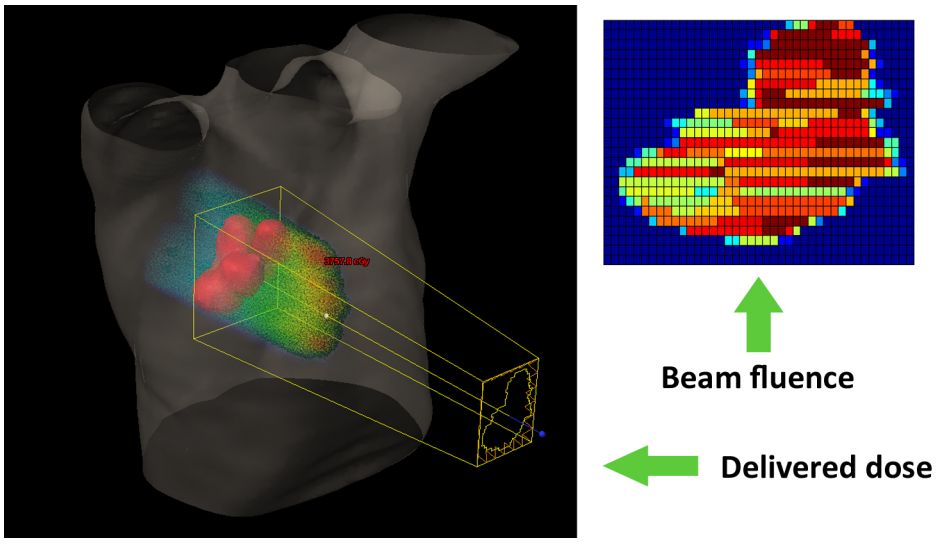

Figure 4.11: Beam fluence and delivered dose from one beam. Fluence and dose are displayed in color scale. Gray and red volumes represent body and PTV respectively.

is the step size of optimization.

The unique feature of the CG method is that the direction of optimization $\vec{d}^k$ is calculated from current gradient of the objective function and the previous direction $\vec{d}^{k-1}$

$$\vec{d}^k = -\nabla f\left(\vec{x}^{k-1}\right) + \vec{\beta}^k \vec{d}^{k-1}$$

where the coefficient $\vec{\beta}^k$ can be estimated by the Polak-Ribiere method

$$\vec{\beta}^k = \frac{\left[\nabla f\left(\vec{x}^k\right) - \nabla f\left(\vec{x}^{k-1}\right)\right] \cdot \nabla f\left(\vec{x}^k\right)}{\nabla f\left(\vec{x}^{k-1}\right) \cdot \nabla f\left(\vec{x}^{k-1}\right)}$$

In each iteration, the fluences x_j can be adjusted based on the new direction of optimization to converge the objective function.

In the classic Newtown's method and Steepest descent algorithm where the direction of optimization is simply the gradient $-\nabla f\left(\vec{x}^{k-1}\right)$, the direction of optimization is always orthogonal to the previous direction [89]. Thus a "zigzag"

path through the solution space is often taken by the algorithm to reach the point of minimum of the objective function. This gives a relative slow convergence rate and long iteration time. Compared to these two methods, the Conjugate Gradient Method combines the current gradient of the objective function and the previous direction of optimization to avoid the "zigzag" path, thus fewer iterations are required to solve the optimization problem (Figure 4.12).

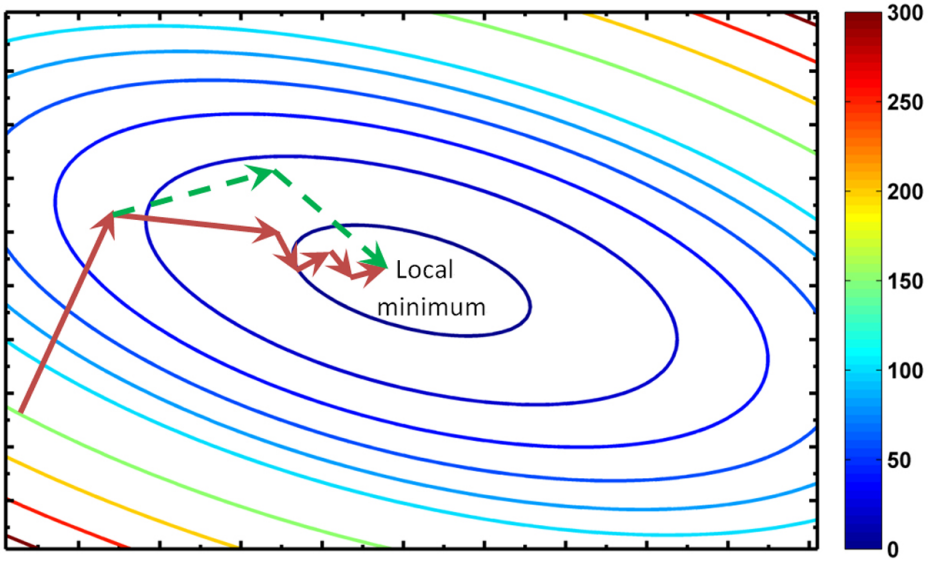

Figure 4.12: The classic Newton and Steepest descent algorithm (brown arrow) optimize along the gradient of the objective function which leads to a "zigzag" path near the local minimum. The conjugate gradient method (dashed green arrow) combines the current gradient and the last direction of optimization and converges faster than previous two methods.

After the beam fluence is optimized, a second step is required to convert the optimal beam intensity to the MLC shapes (apertures) and leaf sequences which could be delivered from the LINAC. In static step-and-shoot IMRT where MLC do not move when a beam is on, this leaf sequencing step is performed by producing a series of MLC apertures with different weights. Radiation beams can be delivered sequentially with these un-equally weighted MLC apertures, thus all MLC apertures superimposed give the optimized beam fluence. In dynamic IMRT where the

MLC move when beam is on, the sliding window method can be used to calculate the position of each MLC leaf at different time interval of dose delivery. Following the speed and position calculated from the sliding window technique, MLC leaves move continuously throughout the delivery thus creating the fluence profile closely matching the optimized profile.

The disadvantage of fluence based optimization for static step and shoot IMRT is that the optimal beam fluence can be quite complex and it could be physically difficult to separate it into a limited number of MLC apertures. Although an increased number of MLC apertures can deliver more a complex beam fluence, this leads to longer beam-on time and more MUs which translates into longer treatment times and increased leakage and scatter radiation from the Linac head. Meanwhile, larger leakage and scatter radiation leads to larger out-of-filed doses and might be associated with higher risks of secondary malignancies. MLC characteristics, such as interleaf leakage and radiation transmitted through the leaves are also not accounted for in the optimization.

4.3.4 Direct Aperture Optimization (DAO)

DAO is a novel treatment planning method for static step and shoot IMRT which bypasses the step of MLC leaf sequencing and addresses some drawbacks of fluence based IMRT treatment planning [90, 91]. In DAO, the position of each MLC leaf and weight of each MLC aperture, rather than the fluence of each beamlet are optimized to achieve optimal beam fluence. In DAO, the leaf sequencing step is not required to translate the optimal intensity maps into a series of deliverable MLC apertures. Compared to fluence based IMRT treatment planning, DAO is capable of delivering a more complex beam fluence with a significant reduction of both the number of MLC apertures and number of MUs [91, 92]. This results in shorter beam on times as well decreased leakage and scatter radiation. MLC leaf leakage between the adjacent leaves and transmission through the leaves can also be incorporated into the treatment planning. In DAO, physical limitations imposed by the MLC are directly included in the optimization as hard constraints, ensuring that the derived optimal plan is always physically deliverable by the MLC. Meanwhile, the number of apertures to be delivered in the optimization is specified by the user

thus providing greater control over the complexity of the treatment plan compared to fluence-based optimization.

In DAO optimization, beam angles and the number of apertures per beam remain constant while the weight of each aperture and positions of each MLC leaves are iteratively adjusted. The initialization of DAO optimization includes specifying:

1. the number of beams;
2. gantry angle and the number of aperture of each beam;
3. the maximum change in the aperture weight;
4. the maximum change of MLC leaf position (step size)

As a starting point of optimization, all the aperture shapes are set to match the BEV of the PTV and the weights of each aperture are equally set so that the mean dose to PTV is equal to the prescribed dose. The dose distribution and the objective function value (cost) are calculated for these initial aperture shapes and weights.

In this study, we implemented the Simulated Annealing (SA) method to optimize the weights and MLC leaf positions for each aperture. Simulated annealing is a generic probabilistic meta-heuristic for the global optimization problem. In the SA method, each point in the solution space can be viewed as a state of the physical system with temperature T and internal energy E. By replacing the internal energy E with the objective function f, the optimization problem of finding the minimum objective function f can be solved in analogy with the physical process of annealing. In each iteration of SA method, the current solution is replaced by another new solution randomly chosen in the nearby solution space. This new solution is accepted with a probability based on the difference between corresponding objective function values and the temperature T. The new solution changes almost stochastically when T is large but becomes more in favor of those yield smaller f (”downhill” solutions) when T goes to zero. Those ”uphill” solutions which give larger f are also randomly accepted with their probabilities gradually decreasing throughout the optimization, thus it provides this method the potential to find a global minimum rather than stuck at the local minima (Figure 4.13)

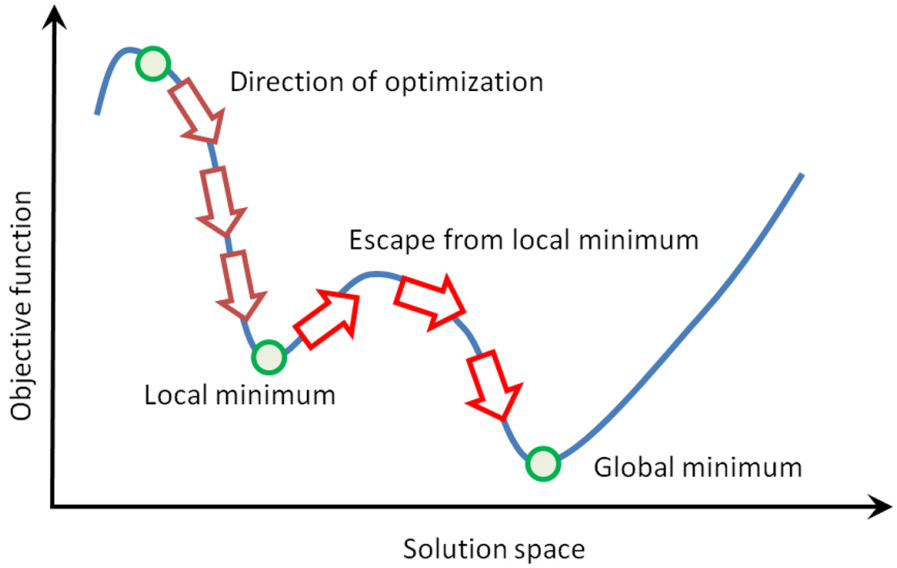

Figure 4.13: In simulate annealing, the capability of accepting "uphill" solutions allows the optimization process to escape from local minima.

In the SA method implemented in this study, the optimization starts with a random selection of an aperture. For this selected aperture, either an open MLC leaf or the aperture weight can be randomly chosen and adjusted, thus there are in total $N_{open}+1$ variables where N_{open} is the total number of open MLC leaves. The probability of choosing a random MLC leaf rather than the aperture weight is set by p_{leaf}, thus leaf position are adjusted most of the time which is more efficient to modulate the beam fluence.

$$p_{leaf} = 1 - \frac{1.5}{N_{open}+1}$$

The change is randomly sampled within the pre-specified range for that variable. The maximum change in either MLC leaf position or aperture weight decreases according to the following schedule:

$$W\left(n_{succ}\right) = \frac{W_0}{\left(1+n_{succ}\right)^{1/R_{step}}}$$

where W_0 is the pre-specified maximum change allowed, i.e. initial maximum MLC leaf step size if the selected variable is a leaf position or initial maximum change in aperture weight if the selected variable is an aperture weight. The parameter R_{step} defines the rate at which the maximum change W decreases as a function of the number of successful changes, n_{succ}.

The new change of the variables is accepted or rejected based on several criteria

Hard constraints

When hard constraints are violated, the new change will be rejected. The hard constraints include:

1. the new MLC leaf position should not retract outside the BEV of PTV;
2. no negative aperture weight;
3. the difference in total weights of each beam does not exceed 50%;

If these hard constraints are not met the new changes are rejected before dose and cost value calculation, otherwise the new change is temporally accepted. Dose distribution and new cost function value are calculated with the new adjusted variable.

Soft constraints

These are the constraints in the objective function such as dose volume constraints, EUD or SWMD constraints. One or several of the soft constraints can be violated with a punishment to the objective function, i.e. increased cost value for some components of the objective function. However, if the selected change gives a lower overall cost value, indicating an improvement towards achieving the planning goals, it will be accepted as a successful change.

If an increased cost value is found with the selected change, instead of automatically rejecting the new change, it is accepted with a probability based on the Metropolis criterion:

$$P = exp\left(-\frac{\Delta f}{T}\right)$$

where Δf is the increase of the cost value and T is the the "temperature" of the system. The probability of retaining a solution with a higher cost value decreases as the temperature decreases. The temperature of the system also "cools down" with a larger number of successful changes of the variables.

$$T\left(n_{succ}\right) = \frac{T_0}{\left(1+n_{succ}\right)^{1/R_T}}$$

where T_0 is the initial system temperature, R_T defines the rate of cooling and n_{succ} is the number of successful changes.

From above two equations, it can be seen that at the early stage of the optimization the system temperature T is high. The changes that increase the cost value are more likely accepted. Meanwhile the search space is relatively large at the beginning of the optimization, with high probability of accepting changes that result in decrease of the cost value. This mechanism allows the optimization to avoid becoming stuck in at local minima. This is the inherent advantage of the simulated annealing method compared to the gradient method, which can lead the optimization converging at a local minimum instead of a global minimum. However the probability of accepting such changes decreases with the progress of optimization as more and more successful changes have been accepted and the system temperature cools down. The size of the search space is also gradually reduced during the optimization allowing the algorithm to converge to a final solution. Ideally this will give the variables at a global minimum of the objective function. The selection of the initial system temperature and the rate of cooling is crucial in simulated annealing, since these parameters determine the algorithm's ability to escape from any local minima, as well as the speed of convergence to the final solution.

After the optimization is completed, the output is a set of deliverable apertures. The final apertures generally have different shapes and weights, as shown in Figure 4.14.

4.4 Materials and Methodology of the Planning Study

The planning study was carried out to investigate the effectiveness of lung functional sparing in SPECT guided IMRT treatment planning and to compare SPECT

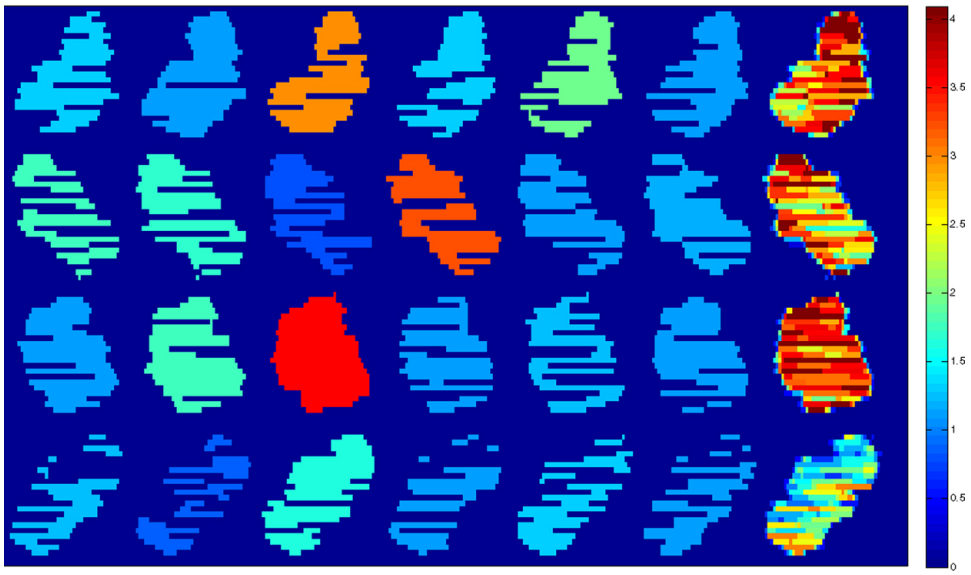

Figure 4.14: Shape of each aperture (left) and accumulated fluence of each aperture (right) from one IMRT plan. Relative weight of each aperture is displayed in color scale.

guided vs. DVH guided IMRT plans. Planning CT and SPECT images from five non-small cell lung cancer (NSCLC) patients were included in this study. Perfusion SPECT scans and CT simulations were performed as described in Chapter 1. Perfusion SPECT images were reconstructed using iterative reconstruction methods with attenuation and scatter correction (OSEM-APD method as introduced in Chapter 2). The SPECT images were subsequently co-registered with planning CT using a rigid registration method. The accuracy of this registration method has been evaluated and reported in Chapter 3. GTV and PTV were contoured by radiation oncologists according to clinical protocol. Lung volume was segmented using CT intensity window in Eclipse treatment planning system. A new "Lung minus PTV" volume which was a surrogate of normal lung for optimization was created as lung volume subtracts PTV. Spinal cord was also contoured out as OAR for dose sparing.

For each patient, two RT plans were generated using DAO with Monte Carlo generated beamlet dose calculation.

1. DVH-guided plan: IMRT plan generated using conventional DVH constraints for targets and OARs without SPECT guidance.

2. SPECT-guided plan: IMRT plan generated using SPECT weighted mean dose (SWMD) as the metric of lung function sparing during treatment planning. EUD-based approach was adopted to optimize PTV dose coverage and OAR sparing.

Both plans used the same field setup with four fields and six apertures per each field. Based on previous studies [93] and testing with different setups, the gantry angles for each field were selected as:

1. For left sided tumors: 30 or 60, 120, 180, 330 degrees.

2. For right sided tumors: 30, 330, 240 and 180 degrees.

In the DVH-guided treatment planning, dose-volume constraints were adopted for optimization. The constraints for PTV dose coverage included the following constraints:

1. More than 99% of PTV is covered by the 57Gy iso-dose line (95% of prescription dose).

2. More than 99.5% of PTV is covered by the 55.8Gy iso-dose line (93% of prescription dose).

3. Less than 5% of PTV receives more than 63Gy.

4. The maximum dose in PTV does not exceed 65Gy.

Dose-volume constraints for V20 and spinal cord were:

1. $V_{5Gy} < 30\%$, less than 30% of the "Lung minus PTV" volume receives 5Gy and above

2. $V_{20Gy} < 10\%$, $V_{30Gy} < 5\%$.

3. The maximum dose in spinal cord is limited to 37Gy$\sim$45Gy.

Table 4.1: Typical SWMD and EUD constraints used in the SPECT guided treatment planning

	EUD_0	γ
PTV ($n = -0.1$)	60Gy	20
Spinal cord ($n = 0.05$)	40Gy	10
	$SWMD_0$	γ
Lung minus PTV volume	5Gy	10

In the SPECT-guided treatment planning, SPECT weighted mean dose (SWMD) and equivalent uniform dose (EUD) were incorporated into the objective function. A representative set of SWMD and EUD constraints used in SPECT-driven plans is listed in Table 4.1.

The weight of each constraint was iteratively adjusted in both SPECT guided and DVH guided treatment planning. DVH and EUD constraints for spinal cord were adjusted in such a way that maximum dose delivered to the spinal cord were appoximately the same in DVH and SPECT driven plans. Thus a strict comparison on the sparing of lung volume/function could be carried out with the same field setup and OAR sparing. Sufficient computing time ($\geq$20 hrs) was allowed for iterative optimization, thus the objective function converged to a global minimum.

4.5 Results

4.5.1 Comparison of PTV Coverage and Spinal Cord Sparing

In general, as is the purpose of planning methodology, target dose coverage met the clinical requirement in DVH and SPECT driven plans. Sparing of spinal cord was similar in the two sets of IMRT plans (Figure 4.15).

For all five patients, both DVH driven and SPECT driven IMRT plans satisfed the clinical requirement of dose coverage on PTV (99% of PTV covered by 95% of prescription dose, 99.5% of PTV covered by 93% of prescription dose, Table 4.2). Spinal cord was well spared in both DVH and SPECT driven plans (Table 4.3). Maximum dose ranged from 38Gy to 46Gy depending on the relative

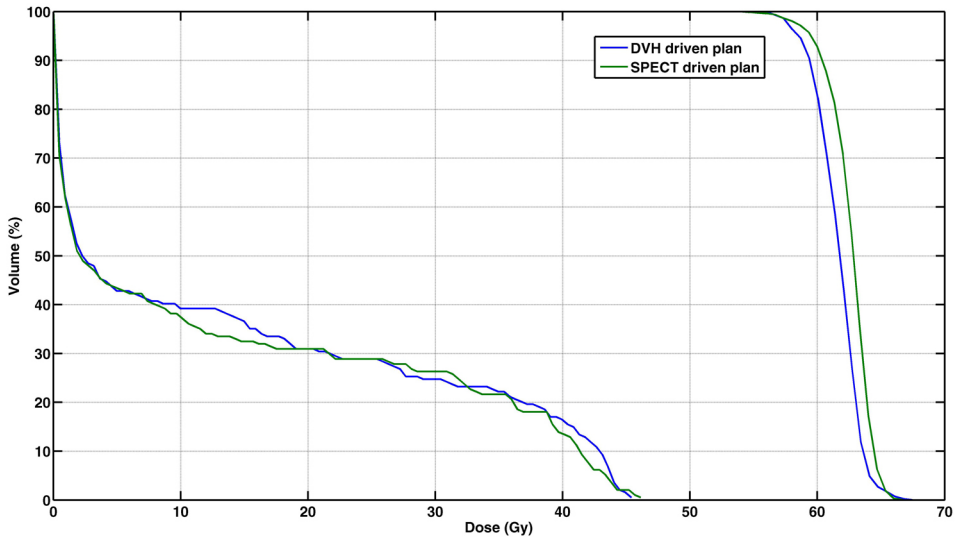

Figure 4.15: DVH of PTV and spinal cord in DVH driven and SPECT driven plans

Table 4.2: PTV dose coverage in DVH and SPECT driven IMRT plans

	DVH driven plans			SPECT driven plans		
	Min	Median	Max	Min	Median	Max
V_{57Gy} (%)	99.0	99.2	99.4	99.1	99.2	99.4
$V_{55.8Gy}$ (%)	99.8	99.8	99.9	99.5	99.6	99.8
EUD (Gy)	61.32	61.58	62.26	62.30	62.57	63.71

position of spinal cord and PTV. No statistically significant difference was found in the cord max dose and EUD between two groups ($p = 0.225$ and 0.5 respectively in Wilcoxon signed-rank test). Although spinal cord is a serial organ and is often partially exposed in the radiation fields in our planning study, the dose delivered to it can be considered as well within tolerance since the maximum tolerable dose suggested for spinal cord in the QUANTEC study is 50Gy which is associated with $< 0.2\%$ probability of myelopathy [94].

Table 4.3: Maximum dose and EUD of the spinal cord

	DVH driven plans			SPECT driven plans		
	Min	Median	Max	Min	Median	Max
Max dose (Gy)	38.2	42.0	45.5	38.1	42.6	46.1
EUD (Gy)	31.0	36.2	41.4	30.7	36.6	41.0

4.5.2 Comparison of Lung Volume Sparing

We found that SPECT guided IMRT plans provide better volume sparing as compared to conventional DVH guided plans. A sample DVH of the "Lung minus PTV" volume in SPECT and DVH driven plans is shown in Figure 4.16.

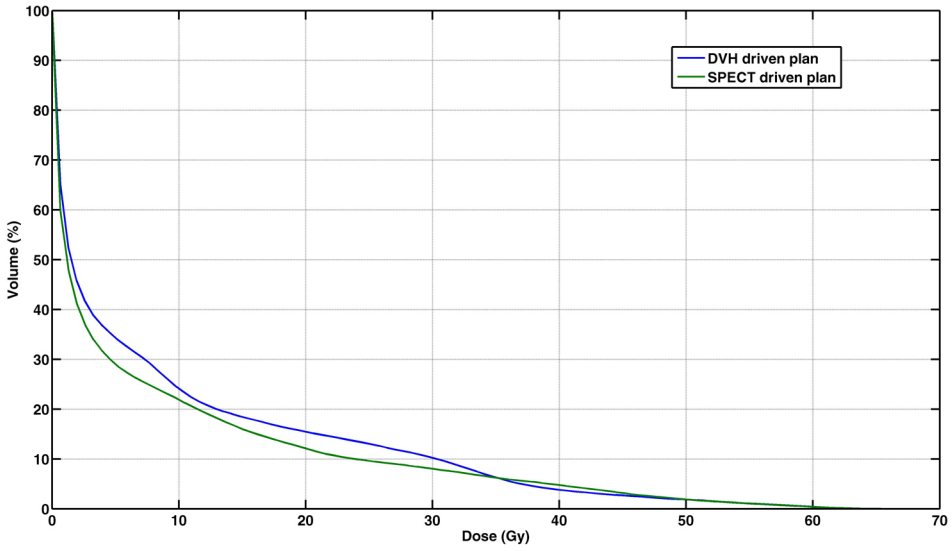

Figure 4.16: DVH of "Lung minus PTV" volume in DVH driven and SPECT driven plans

Dose volume indices and mean lung doses in two sets of plans are listed in Table 4.4. Here we report the analysis of lung volume sparing using three metrics. V_{20Gy} (percentage of the "Lung minus PTV" volume that receives more than

Table 4.4: Sparing of lung volume in DVH and SPECT driven IMRT plans

	DVH driven plans			SPECT driven plans		
	Min	Median	Max	Min	Median	Max
V_{20Gy} (%)	12.5	15.8	21.6	12.1	13.7	21.1
V_{5Gy} (%)	25.5	33.7	40.3	24.1	29.3	38.4
MLD (Gy)	6.4	8.3	11.1	6.2	7.4	11.1

20Gy) is routinely used to predict lung toxicities. Since IMRT plans are typicaly associated with large portion of low dose volume, V_{5Gy} (percentage of the "Lung minus PTV" volume that receives more than 5Gy) is also used to evaluate IMRT plans. Meanwhile mean lung dose (MLD) is suggested as a predictive index in the QUANTEC study [95]. Compared to DVH driven plans, reduction of V_{20Gy} and V_{5Gy} in SPECT driven plans ranged from 0.4% to 3.8% and 1.3% to 5.4%, respectively. V_{5Gy} was found significantly smaller in SPECT guided plans ($p < 0.05$ in Wilcoxon signed-rank test), meanwhile V_{20Gy} and MLD were also found statistically smaller ($p = 0.08$) . Median reduction in V_{20Gy} and V_{5Gy} were 2.1% and 4.4%, respectively. Median MLD was reduced by 0.9Gy (10.8%) using SPECT guided treatment planning suggesting potential benefits for escalating the precription dose delivered to the tumor.

4.5.3 Comparison of Lung Function Sparing

Comparing to DVH driven IMRT plans, improved sparing of lung volume was achieved in SPECT driven plans. Here we report the analysis based on the Dose Function Histogram (DFH) and SWMD (Table 4.5).

DFH was first proposed by Marks et.al [41] as an analog of DVH to evaluate effectiveness of functional sparing in SPECT guided treatment planning. F_{xGy}, the accumulated total function (in this case the sum of SPECT counts), rather than the total volume, which receives more than a threshold dose can be read out from the DFH as shown in Figure 4.17.

Similar to the analysis of lung volume sparing, we choose 20Gy and 5Gy as a

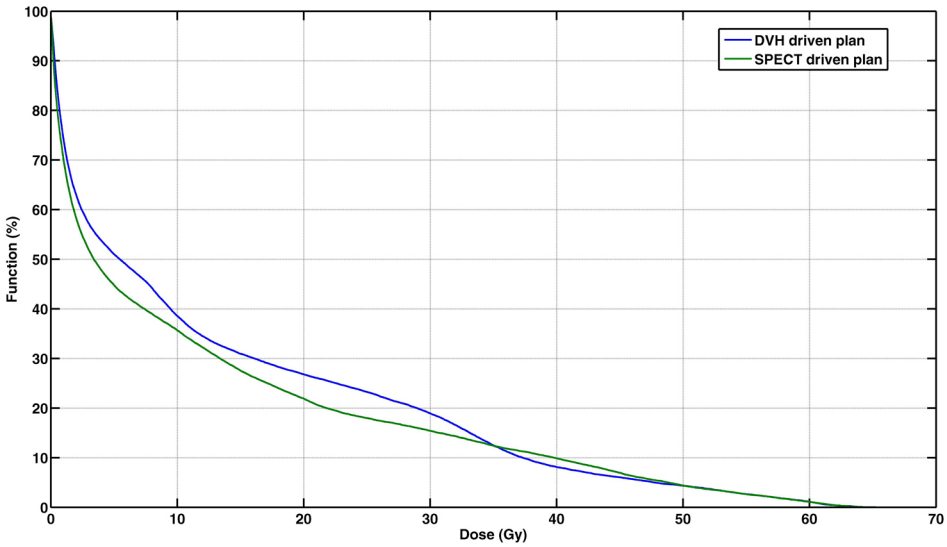

Figure 4.17: DFH of "Lung minus PTV" volume in DVH driven and SPECT driven plans

Table 4.5: Sparing of lung function in DVH and SPECT driven IMRT plans

	DVH driven plans			SPECT driven plans		
	Min	Median	Max	Min	Median	Max
F_{20Gy} (%)	25.0	28.3	40.5	22.1	26.4	39.4
F_{5Gy} (%)	43.9	52.4	59.3	42.2	47.0	57.1
SWMD (Gy)	5.0	9.1	11.4	4.6	7.9	11.2

threshold dose in addition to SWMD for the analysis of DFH indices. Compared to DVH driven plans, reduction of F_{20Gy} and F_{5Gy} in SPECT driven plans ranged from 1.2% to 4.9% and 1.7% to 6.3%, respectively. Median reductions in F_{20Gy} and F_{5Gy} were 1.9% and 5.4%, respectively (p = 0.08 for both metrics). Statistically significant reduction in SWMD was found using SPECT approach ($p < 0.05$). Median SWMD can be reduced by 1.2Gy (13.1%) using SPECT guided treatment planning suggesting superior sparing of lung function.

4.6 Discussion and Conclusion

Escalating the dose to the tumor is one approach of improving tumor control rates but it is often associated with excessive lung toxicities. Thus developing a method to improve the normal tissue sparing and reducing RT-induced lung toxicities would be the key to further escalating dose delivered to the tumor. SPECT guided IMRT treatment planning provides means to directly optimize treatment plans based on lung perfusion rather than lung volume.

In this study, SPECT driven plans are designed such that the doses to PTV and spinal cord are similar to DVH driven plans. Thus in SPECT guided treatment planning the dose delivered to lung volumes with high relative functionality is predominantly re-directed to the volumes with lower functionality. Figure 4.16 and Figure 4.17 show typical DVH and DFH, respectively for all five patients that were enrolled in this study. As shown in these two figures, the sparing of lung function is improved at the cost of slightly higher dose to the low perfusion volume. Since lung is generally regarded as a parallel organ, a small increase of the size of dose hot-spots is usually not a big concern. In fact, the part of lung with relatively low perfusion that receives higher dose may be balanced by the larger volume that receives dose in the 10-40Gy region. This was evidenced by the overall improvement in both DVH and DFH shown in Figure 4.16 and Figure 4.17, respectively.

We found that if the hard constraint on MU differences between beams was not applied in the SPECT based optimization, one beam usually delivered much more MUs than the other beams which might lead to potential danger of rib fracture due to the large entrance dose of this particular beam. This was not found in the DVH based optimization suggesting that SPECT based optimization can be in favor of radiation beams with particular gantry angles. Ideally, gantry angles can also be included as the optimizing parameter in the treatment planning. Due to the nature of MC based beamlet dose calculation, $\sim$15 hrs of MC simulation and beamlets segmentation for each beam is required prior to the treatment planning, thus this approach is unable to iteratively adjust gantry angles of each beam during the optimization. In order to have a strict comparison in this study, we adopted the same field setup of gantry angles in SPECT and DVH driven treatment planning. We believe that adjusting gantry angles in SPECT guided treatment planning can

further improve the sparing of lung functionality.

Previous studies on perfusion reduction after radiotherapy have identified evidence in post-treatment SPECT images that hypoperfused regions adjacent to the tumor have shown reperfusion after radiation treatments [5]. This phenomenon may be attributable to reopening of normal blood vessels in healthy lung tissue after the tumor shrunk. These areas would be falsely identified as poorly functioning tissue and therefore potentially receive higher doses in SPECT driven optimization. Meanwhile, the reperfused region might not be ventilated, thus the actual functionality of reperfused region remains unclear without supplementing data from ventilation studies. Lung ventilation SPECT scans are usually carried out with patients inhaleing ^{133}Xenon gas to visualize the air space in the lung. Complete process of oxygen exchange in the lung requires sufficient air flow into the alveolar (ventilation) and blood flow from the alveolar to carriy away the oxygen (perfusion). Ideally, combining both ventilation and perfusion scans would help to further define the functionality of hypoperfused region. However, there is little can be done to avoid irradiation of tissue adjacent to a tumor in IMRT treatment planning where four radiation beams are used to deliver a high grade dose conforming to the PTV.

IMRT is the predominant radiation delivery technique in functional imaging guided radiation therapy. However the role of IMRT in treating lung cancer patients remains unclear mostly due to the concern that it often delivers potentially damaging low dose to a significant portion of normal tissue including lung. This is due to typically used large number of fields and an increase in the delivered MUs, as well as dose from MLC leakage. Tumor motion with respiration also introduces another level of complexity to IMRT with considerable variation between optimized and delivered dose distributions. In this study, we adopted direct aperture optimization with step and shoot technique for IMRT delivery which required lower MUs and shorter beam-on time compared with sliding window technique. This method has a potential to address some drawbacks of conventional IMRT when treating lung cancer patients.

Theoretically, the improvements of the sparing of lung functionality as suggested by SWMD, F_{20Gy} and F_{5Gy} values listed in Table 4.5 can be translated into reduced lung toxicity rates and escalation of tumor dose. Radiation induced reduction in regional lung perfusion has been shown to be correlated to dose in many

studies. However, a reliable functional imaging based approach to predict global lung perfusion and symptoms of lung toxicities is yet to be established. Thus to what degree the dose can be safely escalated without exceeding current toxicity rates can't yet be accurately predicted. In our planning study, the degree of improvements in sparing of lung functionality was patient specific. Generally, we found that for patients with poor pulmonary function, i.e. very inhomogeneous lung perfusion with large area of defects, SPECT driven optimization resulted in clinically applicable treatment plans, which may have caused less radiation damage to functioning lung, compared to treatment plans that were optimized on the lung volume. For patients with good pulmonary function, i.e. homogeneous lung perfusion with only small defects, not much gain can be achieved through SPECT based optimization. The size of tumors also limits the flexibility of the normal tissue sparing.

In conclusion, we suggest that the use of SPECT guided IMRT treatment planning generally improves the sparing of lung functionality and and may make possible dose escalations in patients with non-small cell lung cancers.

Chapter 5

Future Work

In this study, a complete streamline of perfusion SPECT guided RT treatment planning has been developed and implemented. The investigations of all steps of this process, e.g. image reconstruction, registration, and treatment planning, are described in Chapter 2 to Chapter 4, respectively. The impact of image reconstruction on treatment planning is presented in Chapter 2. A comprehensive evaluation on the accuracy of image registration methods is reported in Chapter 3. In these studies, we recommend to use iterative method with attenuation corrections to reconstruct perfusion SPECT images and co-register it with planning CT images through rigid registration. We also propose the use of SPECT weighted mean dose as a proper metric of functional sparing in treatment planning. The methodology and results of the planning study using perfusion SPECT guided treatment planning is presented in Chapter 4. It suggests that SPECT guided IMRT planning based on EUD and SWMD provides better lung sparing of both anatomical and functional volumes as compared to conventional dose-volume driven IMRT plans.

Several planning studies have demonstrated the gain of functional sparing in perfusion SPECT guided RT. However the possible improvement in lung toxicities has yet to be shown. The future work should be focusing on the assessment of clinical outcome based on perfusion SPECT.

In general, radiation effects on regional lung perfusion (Figure 5.1) can be categorized as:

1. Reduction: Visibly reduced SPECT counts in high dose region due to radia-

tion damage to lung tissues.

2. Reperfusion: Due to tumor shrinkage and regression, previously closed pulmonary vessels reopened after the treatment causing increased perfusion. This effect usually occured in previously un-perfused regions adjacent to the tumor.

3. Compensation: Increased SPECT counts in low dose region after the treatment. The real mechanism causing these effects is still unclear. It may be due to the way the reconstruction is renormalized or reflect the true increase in blood flow to compensate for the reduced perfusion in other high dose volume.

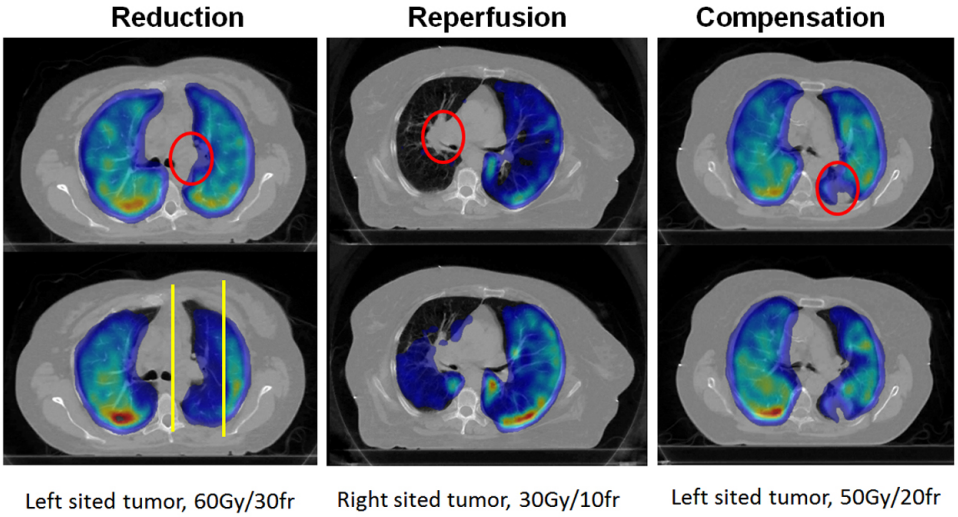

Figure 5.1: Pre-RT (upper row) and post-RT (bottom) SPECT scans demonstrating reduction, reperfusion and compensation of perfusion respectively. Red contours indicate the position of tumor. Yellow contours shows a rough estimate of high dose (>20Gy) region.

In our study, three groups of patients consented to have pre and post RT SPECT scans.

1. Five patients treated with radical intent (60Gy/30 fractions)

2. Three patients treated with palliative intent (30Gy/10 fractions and 40Gy/15 fractions)

3. Three patients treated with SBRT (48Gy to the PTV margin and 60Gy to the iso-center in four fractions).

The effect of radiation on regional lung perfusion in the patients treated with radical 3D-CRT has been well studied by calculating the dose-response curve (DRC) as the percentage change in SPECT counts after the treatment [96–98].

$$DRC(dose) = \left(1 - \frac{post-RT\ \ SPECT\ \ counts}{pre-RT\ \ SPECT\ \ counts}\right) \times 100\%$$

However, to the best of our knowledge, the analysis on the other two patient groups has not been reported yet. Thus it would be interesting to compare the correlation of dose with perfusion reduction in these three groups.

In the palliative patient group, the pattern of perfusion differences after RT was inconsistent. The threshold dose of compensation (increased perfusion in low dose region) could not be found, although increased perfusion in either low dose or high dose volume was common but not consistent. A dose-response curve was not observed in the palliative group (Figure 5.2).

In the radical patient group, a consistent pattern of compensation and reduction of perfusion was observed in four of the five patients (reperfusion was seen in patient 8 in Figure 5.3).

1. Increased SPECT counts were found within volumes receiving less than a certain dose, this threshold ranged from 12 to 35Gy.

2. A strong correlation between dose and change in perfusion distribution, i.e. dose response curve (DRC), was found. D50, dose causing 50% reduction in perfusion ranged from 39 to 54Gy.

In the SBRT patient group, a consistent pattern of decreased perfusion was observed in two out of three patients (reperfusion was seen in patient 9 in Figure 5.4)

1. The amount of increased perfusion in low dose region (compensation) in SBRT group was much smaller as compared to the radical 3D-CRT group.

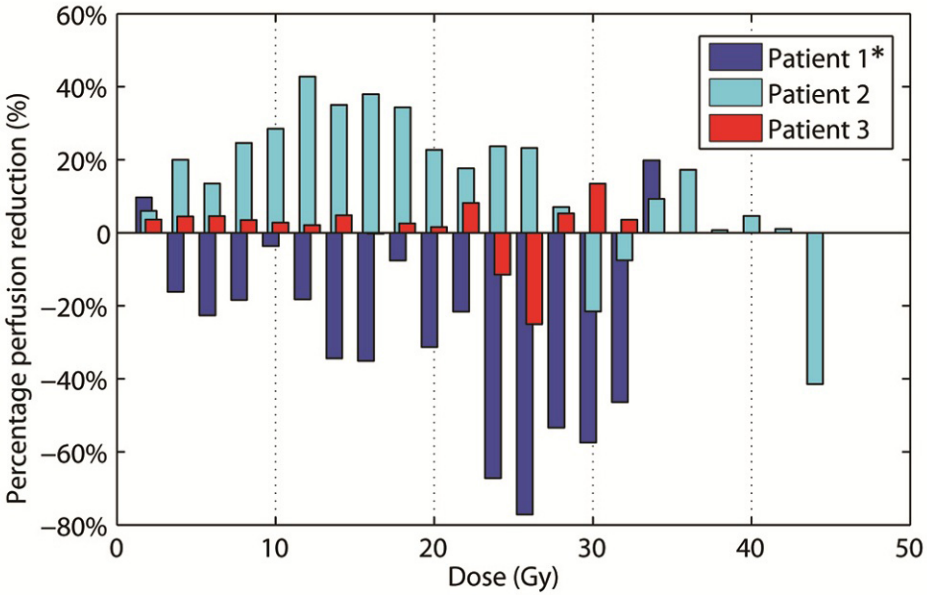

Figure 5.2: Perfusion change in patients treated with palliative 3D-CRT

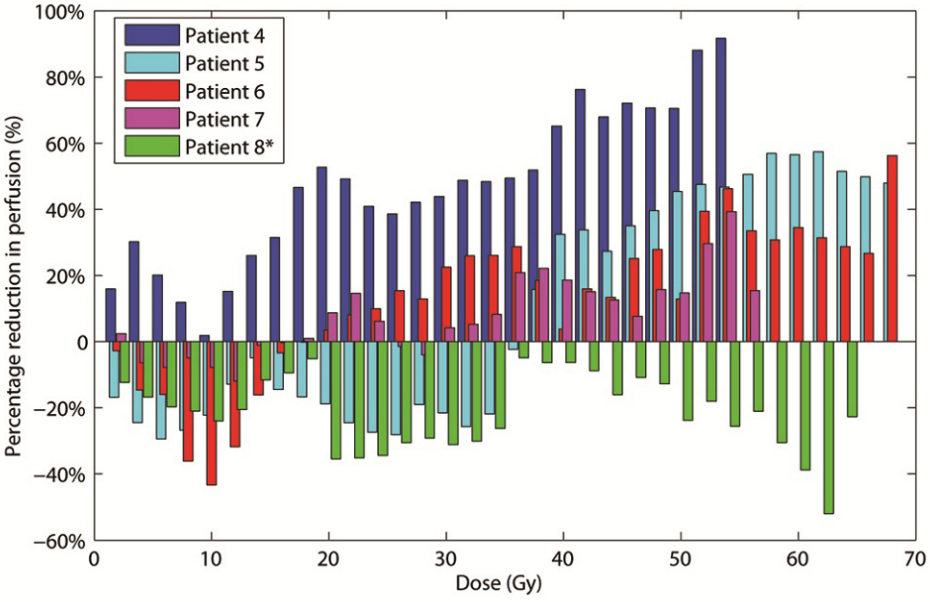

Figure 5.3: Perfusion change in patients treated with radical 3D-CRT (* indicates reperfusion)

2. Compared to the patients treated with radical 3D-CRT (excluding patient with reperfusion), the reduction in perfusion caused by high grade dose (>30Gy) was much smaller in SBRT patients. For example, mean perfusion reduction at 45Gy was 25% in SBRT group and 35% in radical 3D-CRT group, respectively.

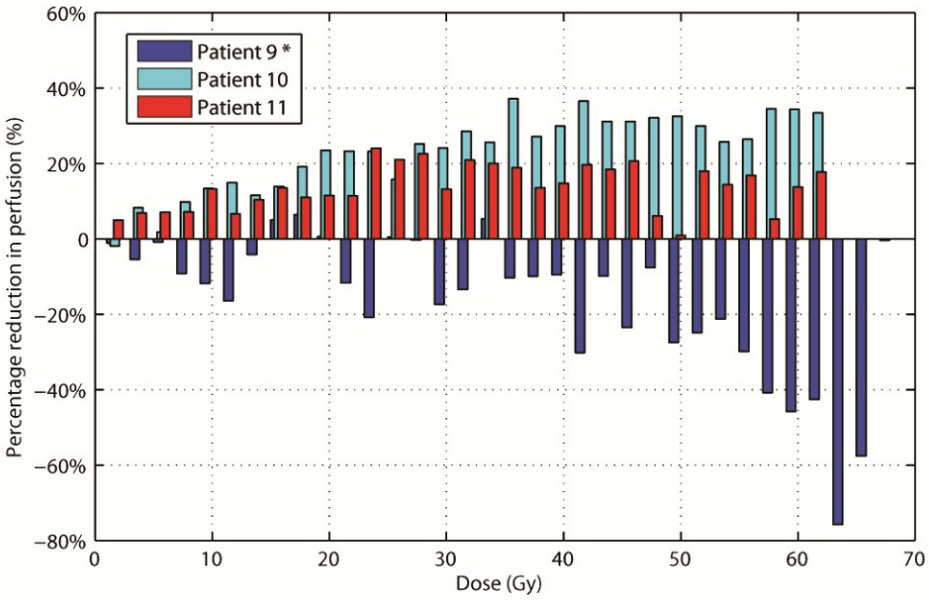

Figure 5.4: Perfusion change in patients treated with SBRT (* indicates reperfusion)

To the best of our knowledge, this is the first perfusion SPECT study in lung cancer patients treated with SBRT. We found that SBRT causes less perfusion damage than 3D-CRT which is quite an interesting finding. On the one hand, it does not agree with the general conception that hypo-fractionation (12Gy/fraction in SBRT vs 2Gy/fraction in 3D-CRT) causes more cell killing and tissue damage, on the other hand, patients treated with SBRT do have moderate rate of lung toxicities as compared to patients treated with conventional dose fractionation [99–102]. Increased damage to lung perfusion due to hypo-fractionation might be cancelled out by the normal tissue repairing during the pro-longed interval between treatments in SBRT. Meanwhile, small size of the tumor as well as non-coplanar fields setup also

contributes to the improvements of lung irradiation. More patient data is required for a detailed analysis of this effect. Perfusion SPECT imaging study in lung cancer patients treated with SBRT is still ongoing and currently the focus of our group in Vancouver Cancer Centre.

In conclusion, actual clinical benefit of perfusion SPECT or other functional imaging modalities guided radiation therapy has yet to be demonstrated. The correlation between functional information and clinical symptoms such as tumor control and normal tissue toxicities is not clear at this moment. It remains the most important issue hindering the practical use of perfusion SPECT as well as other functional imaging modalities in radiation therapy. Meanwhile several factors including tumor/normal tissue segmentation, image reconstruction/registration techniques and parameters must be taken into cautious consideration in functional imaging guided radiation therapy.

Bibliography

[1] "Cancer fact sheets," tech. rep., World Health Organization, 2009. → pages 1

[2] "Cancer facts & figures," tech. rep., American Cancer Society, 2010. → pages 1

[3] J. A. Hayman, M. K. Martel, R. K. T. Haken, D. P. Normolle, R. F. T. 3rd, J. F. Littles, M. A. Sullivan, P. W. Possert, A. T. Turrisi, and A. S. Lichter, "Dose escalation in non-small-cell lung cancer using three-dimensional conformal radiation therapy: update of a phase i trial," *J.Clin.Oncol.*, vol. 19, pp. 127–136, Jan 1 2001. → pages 2, 29

[4] J. S. Belderbos, W. D. Heemsbergen, K. D. Jaeger, P. Baas, and J. V. Lebesque, "Final results of a phase i/ii dose escalation trial in non-small-cell lung cancer using three-dimensional conformal radiotherapy," *Int.J.Radiat.Oncol.Biol.Phys.*, vol. 66, pp. 126–134, Sep 1 2006. → pages 2, 28, 29

[5] L. B. Marks, D. P. Spencer, G. W. Sherouse, G. Bentel, R. Clough, K. Vann, R. Jaszczak, R. E. Coleman, and L. R. Prosnitz, "The role of three dimensional functional lung imaging in radiation treatment planning: the functional dose-volume histogram," *Int.J.Radiat.Oncol.Biol.Phys.*, vol. 33, pp. 65–75, Aug 30 1995. → pages 2, 30, 112

[6] T. T. PUCK and P. I. MARCUS, "Action of x-rays on mammalian cells," *The Journal of experimental medicine*, vol. 103, pp. 653–666, May 1 1956. → pages 7

[7] B. Emami, J. Lyman, A. Brown, L. Coia, M. Goitein, J. E. Munzenrider, B. Shank, L. J. Solin, and M. Wesson, "Tolerance of normal tissue to therapeutic irradiation," *Int.J.Radiat.Oncol.Biol.Phys.*, vol. 21, pp. 109–122, May 15 1991. → pages 8

[8] G. J. Kutcher and C. Burman, "Calculation of complication probability factors for non-uniform normal tissue irradiation: the effective volume method," *Int.J.Radiat.Oncol.Biol.Phys.*, vol. 16, pp. 1623–1630, Jun 1989. → pages 9, 93

[9] C. Burman, G. J. Kutcher, B. Emami, and M. Goitein, "Fitting of normal tissue tolerance data to an analytic function," *Int.J.Radiat.Oncol.Biol.Phys.*, vol. 21, pp. 123–135, May 15 1991. → pages 10

[10] O. Chapet, E. Thomas, M. Kessler, B. Fraass, and R. T. Haken, "Esophagus sparing with imrt in lung tumor irradiation: an eud-based optimization technique," *Int.J.Radiat.Oncol.Biol.Phys.*, vol. 63, pp. 179–187, Sept 2005. → pages 11

[11] T. E. Schultheiss, C. G. Orton, and R. A. Peck, "Models in radiotherapy: volume effects," *Med.Phys.*, vol. 10, pp. 410–415, Jul-Aug 1983. → pages 11

[12] E. A. Eisenhauer, P. Therasse, J. Bogaerts, L. H. Schwartz, D. Sargent, R. Ford, J. Dancey, S. Arbuck, S. Gwyther, M. Mooney, L. Rubinstein, L. Shankar, L. Dodd, R. Kaplan, D. Lacombe, and J. Verweij, "New response evaluation criteria in solid tumours: revised recist guideline (version 1.1)," *European journal of cancer (Oxford, England : 1990)*, vol. 45, pp. 228–247, Jan 2009. → pages 12

[13] "Common terminology criteria for adverse events (ctcae) v3.0," tech. rep., National Cancer Institute. → pages 13

[14] J. D. Cox, J. Stetz, and T. F. Pajak, "Toxicity criteria of the radiation therapy oncology group (rtog) and the european organization for research and treatment of cancer (eortc)," *Int.J.Radiat.Oncol.Biol.Phys.*, vol. 31, pp. 1341–1346, Mar 30 1995. → pages 13

[15] S. Green and G. R. Weiss, "Southwest oncology group standard response criteria, endpoint definitions and toxicity criteria," *Investigational new drugs*, vol. 10, pp. 239–253, Nov 1992. → pages 13

[16] "Lent soma scales for all anatomic sites," *Int.J.Radiat.Oncol.Biol.Phys.*, vol. 31, pp. 1049–1091, Mar 30 1995. → pages 13

[17] M. V. Graham, J. A. Purdy, B. Emami, W. Harms, W. Bosch, M. A. Lockett, and C. A. Perez, "Clinical dose-volume histogram analysis for pneumonitis after 3d treatment for non-small cell lung cancer (nsclc),"

Int.J.Radiat.Oncol.Biol.Phys., vol. 45, pp. 323–329, Sep 1 1999. → pages 13, 27, 29

[18] "Icru report 50 - prescribing, recording and reporting photon beam therapy," tech. rep., International Commission on Radiation Units and Measurements. → pages xi, 15, 16

[19] R. Timmerman, L. Papiez, R. McGarry, L. Likes, C. DesRosiers, S. Frost, and M. Williams, "Extracranial stereotactic radioablation: results of a phase i study in medically inoperable stage i non-small cell lung cancer," *Chest*, vol. 124, pp. 1946–1955, Nov 2003. → pages 20

[20] C. Mountain, "Revisions in the international system for staging lung cancer," *Chest.*, vol. 111, no. 6, pp. 1710–1717, 1997. → pages 21

[21] C. A. Perez, K. Stanley, P. Rubin, S. Kramer, L. Brady, R. Perez-Tamayo, G. S. Brown, J. Concannon, M. Rotman, and H. G. Seydel, "A prospective randomized study of various irradiation doses and fractionation schedules in the treatment of inoperable non-oat-cell carcinoma of the lung. preliminary report by the radiation therapy oncology group," *Cancer*, vol. 45, pp. 2744–2753, Jun 1 1980. → pages ix, 22, 23

[22] R. O. Dillman, J. Herndon, S. L. Seagren, W. L. E. Jr, and M. R. Green, "Improved survival in stage iii non-small-cell lung cancer: seven-year follow-up of cancer and leukemia group b (calgb) 8433 trial," *Journal of the National Cancer Institute*, vol. 88, pp. 1210–1215, Sep 4 1996. → pages 23

[23] K. Furuse, M. Fukuoka, M. Kawahara, H. Nishikawa, Y. Takada, S. Kudoh, N. Katagami, and Y. Ariyoshi, "Phase iii study of concurrent versus sequential thoracic radiotherapy in combination with mitomycin, vindesine, and cisplatin in unresectable stage iii non-small-cell lung cancer," *J.Clin.Oncol.*, vol. 17, pp. 2692–2699, Sep 1999. → pages 23

[24] E. Soresi, M. Clerici, R. Grilli, U. Borghini, R. Zucali, M. Leoni, M. Botturi, C. Vergari, G. Luporini, and S. S. S, "A randomized clinical trial comparing radiation therapy v radiation therapy plus cis-dichlorodiammine platinum (ii) in the treatment of locally advanced non-small cell lung cancer.," *Semin.Oncol.*, vol. 15, no. 6, Suppl 7, pp. 20–25, 1988. → pages 23

[25] C. Blanke, R. Ansari, R. Mantravadi, R. Gonin, R. Tokars, W. Fisher, K. Pennington, T. O'Connor, S. Rynard, and M. Miller, "Phase iii trial of

thoracic irradiation with or without cisplatin for locally advanced unresectable non-small-cell lung cancer: a hoosier oncology group protocol.," *J.Clin.Oncol.*, vol. 13, no. 6, pp. 1425–1429, 1995. → pages 23

[26] M. Guckenberger, J. Wilbert, A. Richter, K. Baier, and M. Flentje, "Potential of adaptive radiotherapy to escalate the radiation dose in combined radiochemotherapy for locally advanced non-small cell lung cancer.," *Int.J.Radiat.Oncol.Biol.Phys.*, vol. 79, no. 3, pp. 901–908, 2011. → pages 24, 25, 26

[27] S. Bral, M. Duchateau, M. D. Ridder, H. Everaert, K. Tournel, D. Schallier, D. Verellen, and G. Storme, "Volumetric response analysis during chemoradiation as predictive tool for optimizing treatment strategy in locally advanced unresectable nsclc.," *Radiother.Oncol.*, vol. 91, pp. 438–442, 2011. → pages 24, 28

[28] M. Feng, F. Kong, M. Gross, S. Fernando, J. Hayman, and R. T. Haken, "Using fluorodeoxyglucose positron emission tomography to assess tumor volume during radiotherapy for non-small-cell lung cancer and its potential impact on adaptive dose escalation and normal tissue sparing.," *Int.J.Radiat.Oncol.Biol.Phys.*, vol. 73, no. 4, pp. 1228–1234, 2009. → pages 24, 25

[29] C. Gillham, D. Zips, F. Ponisch, C. Evers, W. Enghardt, N. Abolmaali, K. Zophel, S. Appold, T. Holscher, J. Steinbacha, J. Kotzerke, T. Herrmann, and M. Baumann, "Additional pet/ct in week 5c6 of radiotherapy for patients with stage iii non-small cell lung cancer as a means of dose escalation planning?," *Radiother.Oncol.*, vol. 88, pp. 335–341, 2008. → pages 25

[30] F. Kong, R. T. Haken, M.Schipper, M.Sullivan., M.Chen, and C. Lopez, "High-dose radiation improved local tumor control and overall survival in patients with inoperable/unresectable non-small-cell lung cancer: Long-term results of a radiation dose escalation study.," *Int.J.Radiat.Oncol.Biol.Phys.*, vol. 63, no. 2, pp. 324–333, 2005. → pages 25, 26

[31] M. Martel, R. K. T. Haken, M. B. Hazuka, M. L. Kessler, M. Strawderman, A. Turrisi, T. S. Lawrence, B. A. Fraass, and A. S. Lichter, "Estimation of tumor control probability model parameters from 3-d dose distributions of non-small cell lung cancer patients.," *Lung Cancer*, vol. 24, pp. 31–37, 1999. → pages 25

[32] S. E. Schild, W. L. McGinnis, D. Graham, S. Hillman, T. R. Fitch, D. Northfelt, Y. I. Garces, H. Shahidi, L. K. Tschetter, P. L. Schaefer, A. Adjei, and J. Jett, "Results of a phase i trial of concurrent chemotherapy and escalating doses of radiation for unresectable non-small-cell lung cancer," *Int.J.Radiat.Oncol.Biol.Phys.*, vol. 65, pp. 1106–1111, Jul 15 2006. → pages 26, 28

[33] J. Bradley, M. Graham, K. Winter, J. Purdy, R. Komaki, W. Roa, J. Ryu, W. Bosch, and B. Emami, "Toxicity and outcome results of rtog 9311: A phase i-ii dose-escalation study using three-dimensional conformal radiotherapy in patients with inoperable non-small-cell lung carcinoma," *Int.J.Radiat.Oncol.Biol.Phys.*, vol. 61, no. 2, pp. 318–328, 2005. → pages

[34] S. Narayan, G. T. Henning, R. T. Haken, M. Sullivan, M. K. Martel, and J. A. Hayman, "Results following treatment to doses of 92.4 or 102.9 gy on a phase i dose escalation study for non-small cell lung cancer.," *Lung Cancer*, vol. 44, pp. 79–88, 2004. → pages 26

[35] F. M. Kong, J. A. Hayman, K. A. Griffith, G. P. Kalemkerian, D. Arenberg, S. Lyons, A. Turrisi, A. Lichter, B. Fraass, A. Eisbruch, T. S. Lawrence, and R. K. T. Haken, "Final toxicity results of a radiation-dose escalation study in patients with non-small-cell lung cancer (nsclc): predictors for radiation pneumonitis and fibrosis," *Int.J.Radiat.Oncol.Biol.Phys.*, vol. 65, pp. 1075–1086, Jul 15 2006. → pages 27

[36] E. D. Yorke, A. Jackson, K. E. Rosenzweig, L. Braban, S. A. Leibel, and C. C. Ling, "Correlation of dosimetric factors and radiation pneumonitis for non-small-cell lung cancer patients in a recently completed dose escalation study," *Int.J.Radiat.Oncol.Biol.Phys.*, vol. 63, pp. 672–682, Nov 1 2005. → pages

[37] S. Wang, Z. Liao, X. Wei, H. H. Liu, S. L. Tucker, C. S. Hu, R. Mohan, J. D. Cox, and R. Komaki, "Analysis of clinical and dosimetric factors associated with treatment-related pneumonitis (trp) in patients with non-small-cell lung cancer (nsclc) treated with concurrent chemotherapy and three-dimensional conformal radiotherapy (3d-crt)," *Int.J.Radiat.Oncol.Biol.Phys.*, vol. 66, pp. 1399–1407, Dec 1 2006. → pages 27

[38] L. Marks, S. Bentzen, J. Deasy, F. Kong, J. Bradley, I. Vogelius, E. Naga, J. Hubbs, J. Lebesque, R. Timmerman, M. Martel, and A. Jackson,

"Radiation dose-volume effects in the lung," *Int.J.Radiat.Oncol.Biol.Phys.*, vol. 76, pp. S70–76, Mar 1 2010. → pages ix, 27, 28

[39] E. D. Yorke, A. Jackson, K. E. Rosenzweig, S. A. Merrick, D. Gabrys, E. S. Venkatraman, C. M. Burman, S. A. Leibel, and C. C. Ling, "Dose-volume factors contributing to the incidence of radiation pneumonitis in non-small-cell lung cancer patients treated with three-dimensional conformal radiation therapy," *Int.J.Radiat.Oncol.Biol.Phys.*, vol. 54, pp. 329–339, Oct 1 2002. → pages 29

[40] Y. Seppenwoolde, K. D. Jaeger, L. J. Boersma, J. S. Belderbos, and J. V. Lebesque, "Regional differences in lung radiosensitivity after radiotherapy for non-small-cell lung cancer," *Int.J.Radiat.Oncol.Biol.Phys.*, vol. 60, pp. 748–758, Nov 1 2004. → pages 29, 30

[41] L. B. Marks, G. W. Sherouse, M. T. Munley, G. C. Bentel, and D. P. Spencer, "Incorporation of functional status into dose-volume analysis," *Med.Phys.*, vol. 26, pp. 196–199, Feb 1999. → pages 30, 42, 109

[42] Y. Seppenwoolde, M. Engelsman, K. D. Jaeger, S. H. Muller, P. Baas, D. L. McShan, B. A. Fraass, M. L. Kessler, J. S. Belderbos, L. J. Boersma, and J. V. Lebesque, "Optimizing radiation treatment plans for lung cancer using lung perfusion information," *Radiother.Oncol.*, vol. 63, pp. 165–177, May 2002. → pages 30, 31, 42, 43, 56

[43] P. A. Lind, L. B. Marks, D. Hollis, M. Fan, S. M. Zhou, M. T. Munley, T. D. Shafman, R. J. Jaszczak, and R. E. Coleman, "Receiver operating characteristic curves to assess predictors of radiation-induced symptomatic lung injury," *Int.J.Radiat.Oncol.Biol.Phys.*, vol. 54, pp. 340–347, Oct 1 2002. → pages 30

[44] Y. Shioyama, S. Y. Jang, H. H. Liu, T. Guerrero, X. Wang, I. W. Gayed, W. D. Erwin, Z. Liao, J. Y. Chang, M. Jeter, B. P. Yaremko, Y. O. Borghero, J. D. Cox, R. Komaki, and R. Mohan, "Preserving functional lung using perfusion imaging and intensity-modulated radiation therapy for advanced-stage non-small cell lung cancer," *Int.J.Radiat.Oncol.Biol.Phys.*, vol. 68, pp. 1349–1358, Aug 1 2007. → pages 31, 42, 56, 69

[45] S. M. McGuire, S. Zhou, L. B. Marks, M. Dewhirst, F. F. Yin, and S. K. Das, "A methodology for using spect to reduce intensity-modulated radiation therapy (imrt) dose to functioning lung," *Int.J.Radiat.Oncol.Biol.Phys.*, vol. 66, pp. 1543–1552, Dec 1 2006. → pages 42, 56

[46] K. Lavrenkov, S. Singh, J. A. Christian, M. Partridge, E. Nioutsikou, G. Cook, J. L. Bedford, and M. Brada, "Effective avoidance of a functional spect-perfused lung using intensity modulated radiotherapy (imrt) for non-small cell lung cancer (nsclc): an update of a planning study," *Radiother.Oncol.*, vol. 91, pp. 349–352, Jun 2009. → pages 42, 43, 56, 62, 63, 66

[47] K. Lavrenkov, J. A. Christian, M. Partridge, E. Niotsikou, G. Cook, M. Parker, J. L. Bedford, and M. Brada, "A potential to reduce pulmonary toxicity: the use of perfusion spect with imrt for functional lung avoidance in radiotherapy of non-small cell lung cancer," *Radiother.Oncol.*, vol. 83, pp. 156–162, May 2007. → pages 31, 42, 43, 51, 56, 62, 63, 66, 69

[48] G. S. Zeng, J. R. Galt, M. N. Wernick, R. A. Mintzer, and J. N. Aarsvold, *Single Photon Emission Computed Tomography*. Emission Tomography - The Fundamentals of PET and SPECT, Elservier Academic Press, 2004. → pages 36, 38

[49] D. S. Lalush and M. N. Wernick, *Iterative Image Reconstruction*. Emission Tomography - The Fundamentals of PET and SPECT, Elservier Academic Press, 2004. → pages 38, 40

[50] J. A. Christian, M. Partridge, E. Nioutsikou, G. Cook, H. A. McNair, B. Cronin, F. Courbon, J. L. Bedford, and M. Brada, "The incorporation of spect functional lung imaging into inverse radiotherapy planning for non-small cell lung cancer," *Radiother.Oncol.*, vol. 77, pp. 271–277, Dec 2005. → pages 42, 56, 62, 63, 69

[51] S. Shcherbinin, A. Celler, A. Thompson, V. Moiseenko, J. Powe, D. Worsley, L. Yin, C. Duzenli, B. Grill, F. Sheehan, and C. Marlowe, "Quantitative reconstructions of activity distribution in lung spect/ct perfusion patient studies," *Eur. J. Nucl. Med. Mol. Imaging*, vol. 35(suppl 2), p. S334, 2008. → pages 43

[52] A. Thompson, A. Celler, J. Powe, D. Worsley, S. Shcherbinin, L. Yin, C. Duzenli, V. Moiseenko, B. Grill, F. Sheehan, and C. Marlowe, "A comparison of different quantitative spect reconstruction techniques: 3d perfusion maps, and calculation of function-weighted dose in lung.," *Radiother.Oncol.*, vol. 88 Supp 2, p. S275, 2008. → pages 43, 53

[53] R. G. Wells and R. Harrop, "Analytical calculation of photon distribution in spect projections," *IEEE Trans.Nuc.Sci*, vol. 45, p. 3202, 1998. → pages 45

[54] E. J. Vandervoort, A. Celler, R. G. Wells, S. Blinder, K. L. Dixon, and Y. Pang, "Implementation of an analytically based scatter correction in spect reconstructions," *IEEE Trans.Nuc.Sci*, vol. 52, pp. 642–653, 2005. → pages 45

[55] D. Mattes, D. R. Haynor, H. Vesselle, T. K. Lewelen, and W. Eubank, *Non-rigid multimodality image registration*, pp. 1609–1620. Medical Imaging 2001: Image Processing, 2001. → pages 64

[56] M. D. Craene, D. B. d'Aische A., B. Macq, and S. K. Warfield, "Incorporating metric flows and sparse jacobian transformations in itk," *The Insight Journal*, 2006. → pages 64

[57] H. Wang, L. Dong, J. O'Daniel, R. Mohan, A. S. Garden, K. K. Ang, D. A. Kuban, M. Bonnen, J. Y. Chang, and R. Cheung, "Validation of an accelerated 'demons' algorithm for deformable image registration in radiation therapy," *Phys.Med.Biol.*, vol. 50, pp. 2887–2905, Jun 21 2005. → pages 64, 65

[58] T. Vercauteren, X. Pennec, A. Perchant, and N. Ayache, "Diffeomorphic demons using itk's finite difference solver hierarchy," *The Insight Journal*, 2007. → pages 64

[59] B. C. Vemuri, J. Ye, Y. Chen, and C. M. Leonard, "A level-set based approach to image registration," in *IEEE Workshop on Mathematical Methods in Biomedical Image Analysis*, pp. 86–93, IEEE Press New York, 2000. → pages 64, 65

[60] J. M. Fitzpatrick, D. L. Hill, Y. Shyr, J. West, C. Studholme, and C. R. M. Jr, "Visual assessment of the accuracy of retrospective registration of mr and ct images of the brain," *IEEE Transactions on Medical Imaging*, vol. 17, pp. 571–585, Aug 1998. → pages 65

[61] M. Urschler, S. Kluckner, and H. Bischof, "A framework for comparison and evaluation of nonlinear intra-subject image registration algorithms," *The Insight Journal*, 2007. → pages 65, 67

[62] V. Noblet, C. Heinrich, F. Heitz, and J.-P. Armspach, "A topology preserving non-rigid registration method using a symmetric similarity function-application to 3d brain images," in *Lecture Notes in Computer Science: Computer Vision - ECCV 2004*, pp. 546–557, 2004. → pages 71

[63] C. McInotosh and G. Hamarneh, "Optimal weights for convex functionals in medical image segmentation," in *International Symposium on Visual Computing: Special Track on Optimization for Vision, Graphics and Medical Imaging: Theory and Applications (ISVC OVGMI)*, 2009. → pages 71

[64] C. McInotosh and G. Hamarneh, "Is a single energy functional sufficient? adaptive energy functionals and automatic initialization," in *Lecture Notes in Computer Science, Medical Image Computing and Computer-Assisted Intervention (MICCAI)*, pp. 503–510, 2007. → pages

[65] J. Rao, G. Hamarneh, and R. Abugharbieh, "Adaptive contextual energy parameterization for automated image segmentation," in *Internation Symposium on Visual Computing: Special Track on Optimization for Vision, Graphics and Medical Imaging (ISVC OVGMI)*, 2009. → pages 71

[66] P. Castadot, J. A. Lee, A. Parraga, X. Geets, B. Macq, and V. Gregoire, "Comparison of 12 deformable registration strategies in adaptive radiation therapy for the treatment of head and neck tumors," *Radiother.Oncol.*, vol. 89, pp. 1–12, Oct 2008. → pages 71

[67] W. Lu, G. H. Olivera, Q. Chen, K. J. Ruchala, J. Haimerl, S. L. Meeks, K. M. Langen, and P. A. Kupelian, "Deformable registration of the planning image (kvct) and the daily images (mvct) for adaptive radiation therapy," *Phys.Med.Biol.*, vol. 51, pp. 4357–4374, Sep 7 2006. → pages 71

[68] D. Yang, S. R. Chaudhari, S. M. Goddu, D. Pratt, D. Khullar, J. O. Deasy, and I. E. Naqa, "Deformable registration of abdominal kilovoltage treatment planning ct and tomotherapy daily megavoltage ct for treatment adaptation," *Med.Phys.*, vol. 36, pp. 329–338, Feb 2009. → pages 71

[69] Y. Watanabe, "Point dose calculations using an analytical pencil beam kernel for imrt plan checking," *Phys.Med.Biol.*, vol. 46, pp. 1031–1038, Apr 2001. → pages 74

[70] A. M. Bergman, K. Otto, and C. Duzenli, "The use of modified single pencil beam dose kernels to improve imrt dose calculation accuracy," *Med.Phys.*, vol. 31, pp. 3279–3287, Dec 2004. → pages 74

[71] T. R. Mackie, J. W. Scrimger, and J. J. Battista, "A convolution method of calculating dose for 15-mv x rays," *Med.Phys.*, vol. 12, pp. 188–196, Mar-Apr 1985. → pages 74

[72] A. Ahnesjo, "Collapsed cone convolution of radiant energy for photon dose calculation in heterogeneous media," *Med.Phys.*, vol. 16, pp. 577–592, Jul-Aug 1989. → pages 74

[73] H. F. BATHO, "Lung corrections in cobalt 60 beam therapy," *Journal of the Canadian Association of Radiologists*, vol. 15, pp. 79–83, Jun 1964. → pages 75

[74] M. R. Sontag and J. R. Cunningham, "Corrections to absorbed dose calculations for tissue inhomogeneities," *Med.Phys.*, vol. 4, pp. 431–436, Sep-Oct 1977. → pages 75

[75] A. M. Bergman, K. Bush, M. P. Milette, I. A. Popescu, K. Otto, and C. Duzenli, "Direct aperture optimization for imrt using monte carlo generated beamlets," *Med.Phys.*, vol. 33, pp. 3666–3679, Oct 2006. → pages 76, 84

[76] I. Kawrakow and D. W. O. Rogers, "The egsnrc code system: Monte carlo simulation of electron and photon transport," Tech. Rep. Technical Report PIRS-701 National Research Council of Canada, Ottawa, Canada, 2000. → pages 79

[77] D. W. Rogers, B. A. Faddegon, G. X. Ding, C. M. Ma, J. We, and T. R. Mackie, "Beam: a monte carlo code to simulate radiotherapy treatment units," *Med.Phys.*, vol. 22, pp. 503–524, May 1995. → pages 80

[78] N. Reynaert, B. D. Smedt, M. Coghe, L. Paelinck, B. V. Duyse, W. D. Gersem, C. D. Wagter, W. D. Neve, and H. Thierens, "Mcde: a new monte carlo dose engine for imrt," *Phys.Med.Biol.*, vol. 49, pp. N235–41, Jul 21 2004. → pages 82

[79] P. R. Almond, P. J. Biggs, B. M. Coursey, W. F. Hanson, M. S. Huq, R. Nath, and D. W. Rogers, "Aapm's tg-51 protocol for clinical reference dosimetry of high-energy photon and electron beams," *Med.Phys.*, vol. 26, pp. 1847–1870, Sep 1999. → pages 82

[80] I. A. Popescu, C. P. Shaw, S. F. Zavgorodni, and W. A. Beckham, "Absolute dose calculations for monte carlo simulations of radiotherapy beams," *Phys.Med.Biol.*, vol. 50, pp. 3375–3392, Jul 21 2005. → pages 82, 83

[81] K. K. Bush, "The generation and application of monte carlo calculated beamlet dose distributions in radiation therapy," *M.Sc Thesis, University of Victoria*, 2003. → pages 84

[82] J. V. Dyk, R. B. Barnett, J. E. Cygler, and P. C. Shragge, "Commissioning and quality assurance of treatment planning computers," *Int.J.Radiat.Oncol.Biol.Phys.*, vol. 26, pp. 261–273, May 20 1993. → pages 86, 87

[83] D. A. Low, W. B. Harms, S. Mutic, and J. A. Purdy, "A technique for the quantitative evaluation of dose distributions," *Med.Phys.*, vol. 25, pp. 656–661, May 1998. → pages 86

[84] M. K. S. Breedveld, P. R. M. Storchi and B. J. M. Heijmen, "Fast, multiple optimizations of quadratic dose objective functions in imrt," *Phys. Med. Biol.*, vol. 51, no. 14, pp. 3569–3579, 2006. → pages 90

[85] A. Niemierko, "Reporting and analyzing dose distributions: a concept of equivalent uniform dose," *Med.Phys.*, vol. 24, pp. 103–110, Jan 1997. → pages 93

[86] Q. Wu, L. Xing, G. Ezzell, and R. Mohan, *Chapter 4 Inverse Treatment Planning*, vol. 2 of *The Modern Technology of Radiation Oncology: A Compendium for Medical Physicists and Radiation Oncologists*. Madison WI: Med.Phys. Publishing, 1 ed., 2005. → pages 93

[87] Q. Wu, R. Mohan, A. Niemierko, and R. Schmidt-Ullrich, "Optimization of intensity-modulated radiotherapy plans based on the equivalent uniform dose," *Int.J.Radiat.Oncol.Biol.Phys.*, vol. 52, pp. 224–235, Jan 1 2002. → pages 93, 94

[88] S. V. Spirou and C. S. Chui, "A gradient inverse planning algorithm with dose-volume constraints," *Med.Phys.*, vol. 25, pp. 321–333, Mar 1998. → pages 96

[89] X. Zhang, H. Liu, X. Wang, L. Dong, Q. Wu, and R. Mohan, "Speed and convergence properties of gradient algorithms for optimization of imrt," *Med.Phys.*, vol. 31, pp. 1141–1152, May 2004. → pages 97

[90] W. D. Gersem, F. Claus, C. D. Wagter, B. V. Duyse, and W. D. Neve, "Leaf position optimization for step-and-shoot imrt," *Int.J.Radiat.Oncol.Biol.Phys.*, vol. 51, pp. 1371–1388, Dec 1 2001. → pages 99

[91] D. M. Shepard, M. A. Earl, X. A. Li, S. Naqvi, and C. Yu, "Direct aperture optimization: a turnkey solution for step-and-shoot imrt," *Med.Phys.*, vol. 29, pp. 1007–1018, Jun 2002. → pages 99

[92] C. Cotrutz and L. Xing, "Segment-based dose optimization using a genetic algorithm," *Phys. Med. Biol.*, vol. 48, no. 18, pp. 2987–2998, 2003. → pages 99

[93] S. M. McGuire, L. B. Marks, F. F. Yin, and S. K. Das, "A methodology for selecting the beam arrangement to reduce the intensity-modulated radiation therapy (imrt) dose to the spect-defined functioning lung," *Phys.Med.Biol.*, vol. 55, pp. 403–416, Jan 21 2010. → pages 105

[94] J. P. Kirkpatrick, A. J. van der Kogel, and T. E. Schultheiss, "Radiation dose-volume effects in the spinal cord," *Int.J.Radiat.Oncol.Biol.Phys.*, vol. 76, pp. S42–9, Mar 1 2010. → pages 107

[95] L. B. Marks, S. M. Bentzen, J. O. Deasy, F. M. Kong, J. D. Bradley, I. S. Vogelius, I. E. Naqa, J. L. Hubbs, J. V. Lebesque, R. D. Timmerman, M. K. Martel, and A. Jackson, "Radiation dose-volume effects in the lung," *Int.J.Radiat.Oncol.Biol.Phys.*, vol. 76, pp. S70–6, Mar 1 2010. → pages 109

[96] L. Marks, M. Munley, D. Spencer, G. Sherouse, G. Bentel, J. Hoppenworth, M. Chew, R. Jaszczak, R. Coleman, and L. Prosnitz, "Quantification of radiation-indeced regional lung injury with perfusion imaging," *Int.J.Radiat.Oncol.Biol.Phys.*, vol. 38, no. 2, pp. 399–409, 1997. → pages 116

[97] Y. Seppenwoolde, S. Muller, J. Theuws, P. Bass, J. Belderbos, L. Boersma, and J. Lebesque, "Radiation dose-effect relations and local recovery in perfusion for patients with non-small-cell lung cancer," *Int.J.Radiat.Oncol.Biol.Phys.*, vol. 47, no. 3, pp. 681–690, 2000. → pages

[98] J. Zhang, J. Ma, S. Zhou, J. Hubbs, T. Wong, R. Folz, E. Evans, R. Jaszczak, R. Clough, and L. Marks, "Radiation-induced reductions in regional lung perfusion: 0.1-12 year data from a prospective clinical study," *Int.J.Radiat.Oncol.Biol.Phys.*, vol. 76, no. 2, pp. 425–432, 2010. → pages 116

[99] M. Taremi, A. Hope, M. Dahele, S. Pearson, S. Fung, T. Purdie, A. Brade, J. Cho, A. Sun, J. Bissonnette, and A. Bezjak, "Stereotactic body radiotherapy for medically inoperable lung cancer: Prospective, single-center study of 108 consecutive patients," *Int.J.Radiat.Oncol.Biol.Phys.*, 2011. article in press;. → pages 118

[100] R. B. Barriger, J. Forquer, J. Brabham, D. Andolino, R. Shapiro, M. Henderson, P. Johnstone, and A. Fakiris, "A dosecvolume analysis of radiation pneumonitis in noncsmall cell lung cancer patients treated with stereotactic body radiation therapy," *Int.J.Radiat.Oncol.Biol.Phys.*, 2011. article in press;. → pages

[101] R. Timmerman, R. Paulus, J. Galvin, J. Michalski, W. Straube, J. Bradley, A. Fakiris, A. Bezjak, G. Videtic, D. Johnstone, J. Fowler, E. Gore, and H. Choy, "Stereotactic body radiation therapy for inoperable early stage lung cancer," *J.A.M.A*, vol. 303, no. 11, pp. 1070–1076, 2010. → pages

[102] P. Baumanna, J. Nymand, M. Hoyere, G. Gagliardia, I. Laxa, B. Wennberga, N. Drugged, L. Ekbergb, S. Frieslanda, K. Johanssond, J. Lundf, E. Morhedc, K. Nilssonc, N. Levinf, M. Paludane, C. Sederholmg, A. Traberge, L. Wittgrenb, and R. Lewensohna, "Stereotactic body radiotherapy for medically inoperable patients with stage i non-small cell lung cancer c a first report of toxicity related to copd/cvd in a non-randomized prospective phase ii study," *Int.J.Radiat.Oncol.Biol.Phys.*, vol. 88, no. 3, pp. 359–367, 2008. → pages 118